2-2010

Hierarchical Multiple Bit Clusters and Patterned Media Enabled by Novel Nanofabrication Techniques - High Resolution Electron Beam Lithography and Block Polymer Self Assembly

Qijun Xiao
University of Massachusetts Amherst, qxiao77@gmail.com

HIERARCHICAL MULTIPLE BIT CLUSTERS AND PATTERNED MEDIA ENABLED BY NOVEL NANOFABRICATION TECHNIQUES – HIGH RESOLUTION ELECTRON BEAM LITHOGRAPHY AND BLOCK POLYMER SELF ASSEMBLY

A Dissertation Presented

by

QIJUN XIAO

Submitted to the Graduate School of the
University of Massachusetts Amherst in partial fulfillment
of the requirements for the degree of

DOCTOR OF PHILOSOPHY

FEBRUARY 2010

Physics Department

HIERARCHICAL MULTIPLE BIT CLUSTERS AND PATTERNED MEDIA ENABLED BY NOVEL NANOFABRICATION TECHNIQUES – HIGH RESOLUTION ELECTRON BEAM LITHOGRAPHY AND BLOCK POLYMER SELF ASSEMBLY

A Dissertation Presented

by

QIJUN XIAO

Approved as to style and content by:

_____
Mark Tuominen, Chair

_____
Narayanan Menon, Member

_____
Boris Svistunov, Member

_____
Thomas Russell, Member

_____
Donald Candela, Department Head
Physics Department

DEDICATION

To my family and friends.

ACKNOWLEDGMENTS

I would acknowledge all of the supports and help I received during my Ph.D. study. Professor Mark T. Tuominen, as my primary Ph.D. advisor, has led me into this wonderful field of nanosciences, and showed me an excellent example of a successful scientist working diligently and smartly along with his charming personality. Professor Thomas P. Russell and his group gave me direct help on the diblock copolymer related experiments, which was critical for this project to successfully proceed. I also want to acknowledge Professor Vincent Rotello and his group for a very in-depth and successful collaboration on the nanoparticle projects, which are not included in this thesis but the experience surely educated me greatly on the organic chemistry and benefited my whole Ph.D. studies. Special thanks are owned to my current and past group members, along with all of other resources, for the training on instruments and inspiration on researches I have received.

ABSTRACT

HIERARCHICAL MULTIPLE BIT CLUSTERS AND PATTERNED MEDIA ENABLED BY NOVEL NANOFABRICATION TECHNIQUES – HIGH RESOLUTION EBL AND BLOCK POLYMER SELF ASSEMBLY

FEBRUARY 2010

QIJUN XIAO, B.S., UNIVERSITY OF SCIENCE AND TECHNOLOGY, CHINA

M.S., UNIVERSITY OF MASSACHUSETTS AMHERST

Ph.D., UNIVERSITY OF MASSACHUSETTS AMHERST

Directed by: Professor Mark T. Tuominen

This thesis discusses the full scope of a project exploring the physics of hierarchical clusters of interacting nanomagnets. These clusters may be relevant for novel applications such as multilevel data storage devices. The work can be grouped into three main activities: micromagnetic simulation, fabrication and characterization of proof-of-concept prototype devices, and efforts to scale down the structures by creating the hierarchical structures with the aid of diblock copolymer self assembly.

Theoretical micromagnetic studies and simulations based on Landau-Lifshitz-Gilbert (LLG) equation were conducted on nanoscale single domain magnetic entities. For the simulated nanomagnet clusters with perpendicular uniaxial anisotropy, the simulation showed the switching field distributions, the stability of the magnetostatic states with distinctive total cluster perpendicular moments, and the stepwise magnetic switching curves. For simulated nanomagnet clusters with in-plane shape anisotropy, the simulation showed the stepwise switching behaviors governed by thermal agitation and cluster configurations.

Proof-of-concept cluster devices with three interacting Co nanomagnets were fabricated by e-beam lithography (EBL) and pulse-reverse electrochemical deposition (PRECD). EBL patterning on a suspended 100 nm SiN membrane showed improved lateral lithography resolution to 30 nm. The Co nanomagnets deposited using the PRECD method showed perpendicular anisotropy. The switching experiments with external applied fields were able to switch the Co nanomagnets through the four magnetostatic states with distinctive total perpendicular cluster magnetization, and proved the feasibility of multilevel data storage devices based on the cluster concept.

Shrinking the structures size was experimented by the aid of diblock copolymer. Thick poly(styrene)-*b*-poly(methyl methacrylate) (PS-*b*-PMMA) diblock copolymer templates aligned with external electrical field were used to fabricate long Ni/Fe magnetic nanowire array, dominant shape anisotropy was observed and compared to the result from previously reported Co nanowire array with strong crystalline anisotropy. Guided diblock copolymer poly(styrene)-*b*-poly(4-vinyl pyridine) (PS-*b*-P4VP) self assembly was performed to generate clustered microdomains. Direct e-beam patterning on PS-*b*-P4VP thin film showed precise and arbitrary patterning on the lateral ordering of the self assembly. Graphoepitaxy of self-assembled PS-*b*-P4VP copolymers on isolated SiN triangular plateaus successfully resulted in the exact clusters of three microdomains. Theoretical consideration and system modeling based on the micellar configuration of the microdomains were done, and the distribution of the cluster's size and number of elements were explained qualitatively.

TABLE OF CONTENTS

Page

LIST OF FIGURES

CHAPTER 1

INTRODUCTION

1.1 Challenges and difficulties

My work has focused on nanofabrication and characterization of ferromagnetic structures. Currently, the nanofabrication technologies are actively investigated for advanced manufacturing and engineering in the research of novel energy, IT, biology and other critical fields. As the example discussed in this thesis, digital data storage technology has generally relied on a binary storage paradigm. The state-of-the-art magnetic storage media employs the concept of perpendicular bit media, which includes an array of nanomagnets with perpendicular anisotropy. Each nanomagnet has two stable states magnetized up or down normal to the substrate representing the binary 0/1 information. One challenge of nanotechnology is to create magnetic data storage systems with a storage density that exceeds 10^{12} bits/inch^2. [7-17] One possible solution is to construct the media from a high-density array of identical nanomagnets with the powerful block copolymer self assembly systems,[1-3, 19] as shown in Figure 1.1. Copolymer self assembly has been adopted for nanofabrication of templates with ordered nanodomains of 3 to 50 nm [20, 21] for various magnetic, electronic and optical applications. [22, 23]

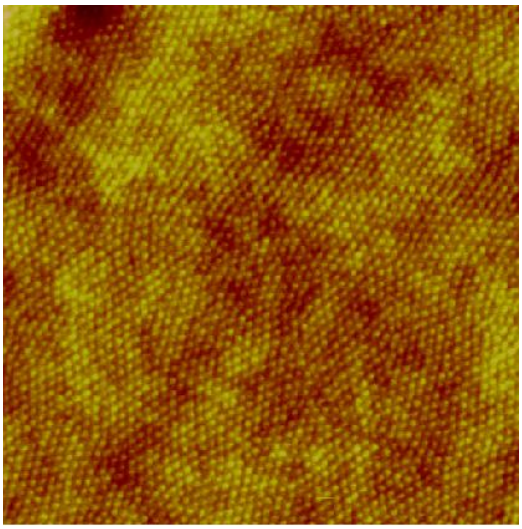

Figure 1.1 Top view of a self-assembly diblock template showing potential for possible ultra-high-density storage devices. The overall dimension of this image is 2 μm.

In hard disk data storage, a bit of binary data is "written" by fully magnetizing a section of granular magnetic film storage media along one specific direction or its opposite. The binary information is "read" by sensing changes in magnetization direction along a track of media.[6] However, addressing ultra-high-density nanomagnet media remains a difficult challenge since present-day read-write technology cannot easily resolve laterally the magnetization of the individual nanomagnets, shown in Figure 1.2. Moreover, densely packed nanomagnets typically have strong magnetostatic interactions with one another, and tend to undergo magnetization reversal collectively.[6] In order to avoid the stray field of the write head pole from switching the nearest neighbors to the target bit, the head needs to be floated less than 2 nm above the media, which is technically challenging in modern hard disks with extremely high spin speed.

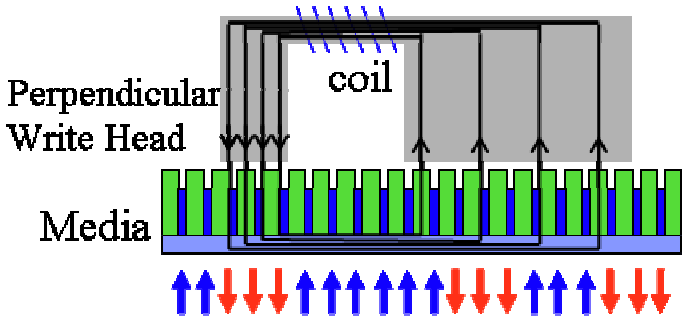

Figure 1.2 Resolution limits due to the size mismatch of the media and the current generation sensor head. (Reference 6)

1.2 Interacting clusters for multilevel storage device

In this work we explore a different data storage paradigm that exploits the stepwise, *multilevel* [5] total magnetization of a small cluster of interacting nanomagnets. This net cluster magnetization can be resolved more easily than that of a single nanomagnet and more compatible with the read/write head, due to the larger lateral size. The whole interacting nanomagnet cluster is treated as the basic unit of the storage device. In such systems, the interaction between the neighbors is favorably used to separate the distinguishable magnetostatic states which represent the different pieces of stored information. This concept [4] is illustrated in Figure 1.3, with comparison to the normal concept of using the full media for the storage device.

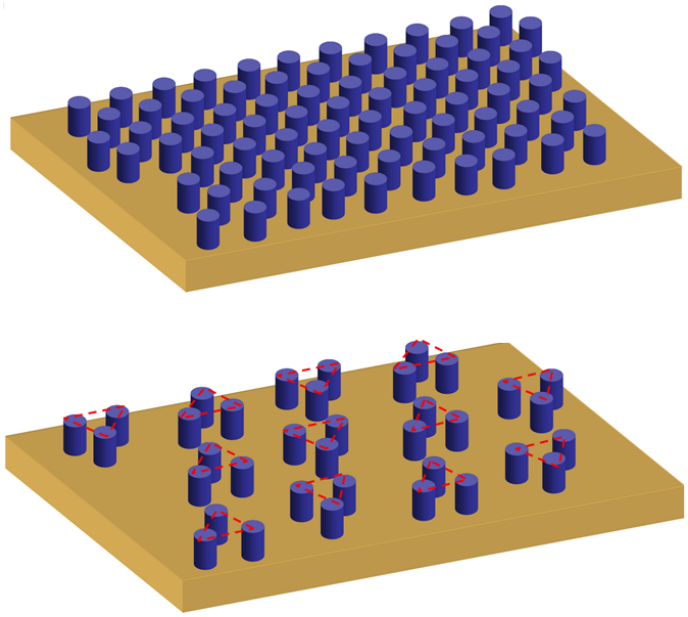

Figure 1.3 Schematic illustration of using the clusters for multiple level storage devices. Top: Common binary bit media with full usage of the media plane. Bottom: Proposed multiple level bit media consisted of array of interacting nanomagnet clusters.

Considering the emergence of recent nanofabrication techniques, it is feasible to make such an ordered cluster containing a specific number of single domain particles. The concept of the multiple level interacting nanomagnet clusters is further explained in Figure 1.4. The applied field is oriented parallel to the easy axis of the single domain nanomagnets, which is along the perpendicular axis. As illustrated schematically in Figure 1.4, the hysteresis loop of such clusters will have multiple magnetization steps that can be used as states representing encoded information. The idea is to "write" the total cluster magnetization M_Z to a specific level by sweeping the field from zero to the requisite value and preserve the remanent state as the stored information after the applied field is turned off. It is important to recognize that for one specific total magnetization there are several distinct configurations having the same

total cluster magnetization. In this thesis, these "degenerate" states are referred as the same state for information storage purposes.

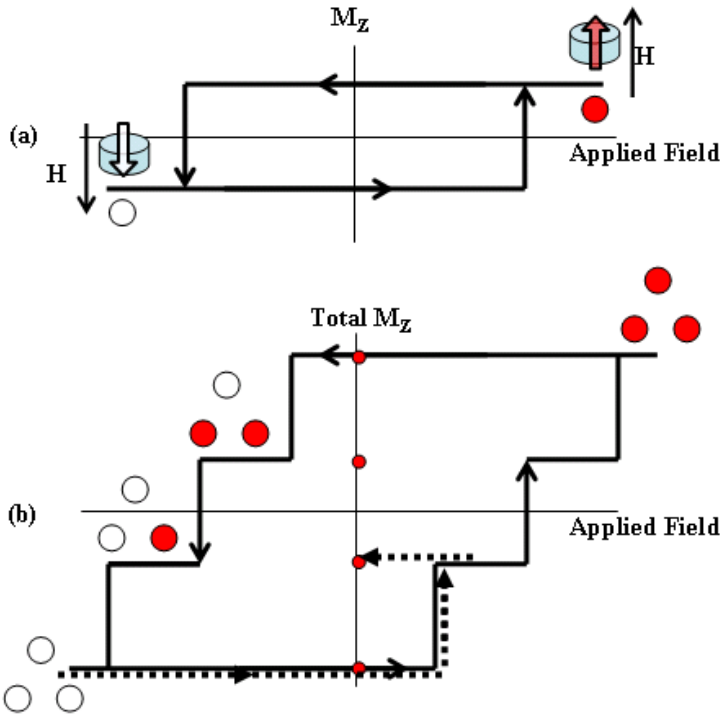

Figure 1.4 (a) A single-domain nanomagnet with a single perpendicular easy axis (uniaxial anisotropy) will have two stable magnetization states under the external field applied along the uniaxial direction**. (**b**)** For illustration purposes, a cluster of three interacting single-domain nanomagnets has 3+1 states with distinguishable total perpendicular magnetization. Upon removal of applied field, each magnetization level can become a stable remanent state. (Reference 4)

1.3 Scope of the thesis

The work described in this thesis includes the experimental efforts to fabricate the ferromagnetic nanostructures with the clustered interacting elements, and theoretical endeavors to guide the fabrication and understand the underlying physics governing the magnetic behavior of the clusters. In Chapter 2 I will show the

micromagnetic simulation work done on the clusters of single domain nanomagnets with perpendicular (to the substrate plane) and in-plane magnetic anisotropies. In Chapter 3 the work to fabricate the perpendicular three-dot nanomagnet clusters as proof-of-concept devices are discussed in great details, which emphasize on e-beam lithography and electrochemical deposition. Static magnetization state measurements done with Magnetic Force Microscopy are included in the characterization section, which show the feasibility of using the multilevel clusters as storage devices. In Chapter 4, an intensive interdisciplinary collaboration effort on using the diblock copolymer self assembly to fabricate nanoscale magnetic structures is shown. Structures with different lateral ordering and dimension are discussed in details. The combination of top-down and bottom-up fabrication approaches is described as the results showed ultra-fine guided diblock copolymer self assembly. This project is essentially interdisciplinary research that creates nanoscale structures with the dimensions inherited from the molecule level and studies the resulted nanomagnetism and switching physics.

1.4 References

1. T. Thurn-Albrecht, J. Schotter, G.A. Kästle, N. Emley, T. Shibauchi, L. Krusin-Elbaum, K. Guarini, C. T. Black, M. T. Tuominen and T. P. Russell, *Science* **290**, 2126 (2000)

2. J. Cheng, C. A. Ross and A. Mayes, *Nature Materials* **3**, 823-8 (2004)

3. K. Naito, H. Hieda, M. Sakurai, Y. Kamata and K. Asakawa, *IEEE Trans. Mag.* **38**, 1949 (2002)

4. Q. Xiao, R. V. Krotkov, and M. T. Tuominen, *J. of Appl. Phys.*, **99**, 08G305 (2006)

5. M. Albrecht, G. Hu, A. Moser, O. Hellwig and B. D. Terris, *J. Appl. Phys*., **97**, 103910 (2005)

6. M. L. Plumer, J. van EK and D. Weller, *The Physics of Ultra-High-Density Magnetic Recording* (Springer, 2001)

7. J. Wong, A. Scherer, M. Todorovic and S. Schultz, *J. Appl. Phys*. **85**, 5489 (1999)

8. S.-Y. Chou, *Proc. IEEE* **85**, 652 (1997)

9. M. Park, C. Harrrison, P. M. Chaikin, R. A. Register and D. H. Adamson, *Science* **276**, 1401 (1997).

10. S. Wirth, S. V. Molnar, M. Field and D. D. Awscholom, *J. Appl. Phys.* **85**, 5249 (1999)

11. G. J. Strikjers, J. H. J. Dalderop, M. A. A. Broeksteeg, J. J. M. Swagten and W. J. M. de Jonge, *J. Appl. Phys*. **86**, 5141 (1999)

12. J. M. Garcia *et al.*, *J. Appl. Phys*. **85**, 5480 (1999)

13. T. L. Hylton *et al.*, *Appl. Phys. Lett.* **67**, 1154 (1995)

14. S. Fan *et al.*, *Science* **283**, 512 (1999)

15. J. Heremans and C. M. Thrush, *Phys. Rev. B* **59**, 12579 (1999)

16. G. Fasol *et al.*, *Science* **275**, 941 (1999)

17. J. Chen, M. A. Reed, A. M. Rawlett and J. M. Tour, *Science* **286**, 1550 (1999)

18. H. Yokoyama, T. E. Mates, and E. J. Kramer, *Macromolecules* **33**, 1888 (2000)

19. J. Y. Cheng, C. A. Ross, V. Z.-H. Chan, E. L. Thomas, R. G. H. Lammertink, and G. J. Vancso, *Adv. Mater*. **13**, 1174 (2001)

20. F. S. Bates, G. H. Fredrickson, *Annu. Rev. Phys. Chem.* **41**, 525 (1990)

21. M. J. Park et al., *Nano Lett.* **7**, 3547 (2007)

22. C. A. Ross, *Annu. Rev. Mater. Res*. **31**, 203 (2001)

23. S. A. Maier *et al. Adv. Mater*. **13**, 1501 (2001)

CHAPTER 2

SIMULATION AND THEORETICAL ANALYSIS OF AN INTERACTING NANOMAGNET CLUSTER

As the first work [1] I had done in this project, micromagnetic dynamics simulations based on the Landau-Lifshitz-Gilbert (LLG) equation [6, 7] reveal that the competing magnetostatic interactions between magnets in a cluster result in a rich multi-level magnetic response, each level providing a stable remanent magnetization. This demonstrates the feasibility of utilizing the multiple level magnetostatic states of the interacting nanomagnet clusters for data storage devices. We study, in particular, the magnetization response of clusters made of low aspect-ratio nanomagnets having significant magneto-crystalline perpendicular anisotropy using parameters typical of Co_3Pt for their potential use as perpendicular bit media elements. Further, we investigate the degree to which the magnetic switching behavior can be tuned by manipulating the symmetry of the cluster. These results further the understanding of multilevel data storage, a topic discussed recently in other related work.[2] Our simulations are used to investigate a multilevel data storage unit based on a hexagonal cluster of interacting uniaxial single domain nanomagnets. These results provide guidance for increasing effective data storage density through the introduction of multilevel data units in storage media.

2.1 Basic setup of the micromagnetic simulation

An important property of the nanomagnet cluster for the purpose of multilevel information storage is to have distinct, well-separated steps on the total magnetization curves. For this purpose it is important to understand the physics underlying the magnetization reversal fields corresponding switching between states. The shape of hysteresis curve depends on the "intrinsic" nanomagnet properties, e.g. saturation magnetization, shape of the particles, and magnetization anisotropy.[3] It also depends on extrinsic parameters, e.g. temperature, applied field sweep rate, and the overall geometry of the cluster.[3]

The hexagonal configuration is inspired by a hierarchical nanofabrication scheme using diblock copolymer templates, which is shown in the reference [5] as an excellent example. For perpendicular media, magnetic parameters representative of Co_3Pt -- a material with relatively strong uniaxial crystalline anisotropy [4] – are chosen in the simulation. For the in-plane media we used the parameters of permalloy ($Ni_{80}Fe_{20}$) because it has negligible crystalline anisotropy.[4] The dimension of the nanomagnets used is 15 nm in diameter and 10 nm in height. The center-to-center distance of elements in the hexagonal array is 30 nm. Comparing the size and separation of the nanomagnets, it is reasonable to use a point dipolar interaction model to represent interactions between elements.

The magnetic state of each single domain nanomagnet can be characterized by a single three-dimensional magnetization unit vector $\vec{m}$. The simulation uses the Laudau-Liftshitz-Gilbert equation [6, 7] to calculate the dynamics of each 3-D nanomagnet's magnetization,

$$\frac{d\vec{m}}{dt} = \frac{\gamma_0}{1+\alpha^2}\vec{m}\times(\vec{H}_{Total} - \alpha\vec{m}\times\vec{H}_{Total})$$

In this formula, γ_0 is the gyromagnetic ratio, α is the damping factor for the magnetic precession, and $\vec{H}_{Total}$ is the effective total magnetic field applied locally to the single nanomaget. This total local field $\vec{H}_{Total}$ is the summation [8] of applied field $\vec{H}_a$, the dipolar interacting field from neighbors $\vec{H}_n$, self-demagnetization field $\vec{H}_d$, the crystalline anisotropy field $\vec{H}_u$ and thermal agitation field $\vec{H}_{th}$

$$\vec{H}_{Total} = \vec{H}_a + \vec{H}_n + \vec{H}_d + \vec{H}_u + \vec{H}_{th}$$

Because the nanomagnets we study here are typically smaller or close to the single domain critical length (depending on the magnetic materials), it is convenient to assume that the nanomagnets are single domain entities. Consequently, we can ignore the intrinsic exchange field for the calculation of $\vec{H}_{Total}$.

In order to calculate $\vec{H}_{Total}$, one needs to specify the terms in the formula separately. $\vec{H}_a$ is determined by the external applied field, which is controllable and arbitrary. $\vec{H}_n$ is a summation of the dipolar interacting fields from all neighbors acting on the magnet of interest. The total dipole-dipole interacting field from neighbors to the targeted nanomagnet $\vec{m}_i$ is

$$\vec{H}_n = M_S V \sum_{j\neq i} \frac{3(\hat{r}_{ij}\cdot\vec{m}_j)\hat{r}_{ij} - \vec{m}_j}{\left|\vec{r}_{ij}\right|^3}$$

M_S is the unit magnetization by volume, V is the volume of the nanomagnet, and $\hat{r}_{ij}, \vec{r}_{ij}$ are the unit spacing vector and spacing vector from the neighbor $\vec{m}_i$ to $\vec{m}_i$ respectively.

The self-demagnetization field $\vec{H}_d$, the demagnetization field from the shape anisotropy, can be calculated as demonstrated below. In a uniform magnetic object with the shape of ellipsoids, the demagnetization field is constant inside the magnetic body. We make the assumption here that the demagnetization inside the nanomagnets of the shape of cylinders can be approximated to be uniform inside the cylinders and can be presented by the demagnetization field at the center of the body. In a cylinder as shown in Figure 2.1 below, the demagnetization at the center can be calculated with the aid of the fictitious magnetic surface charges. The surface magnetic charge density is [15]

$$\sigma_m = \hat{n} \cdot \vec{m} M_S$$

$\hat{n}$ is the unit vector perpendicular to the nanomagnet surface, pointing from inside to the outside of the cylinder.

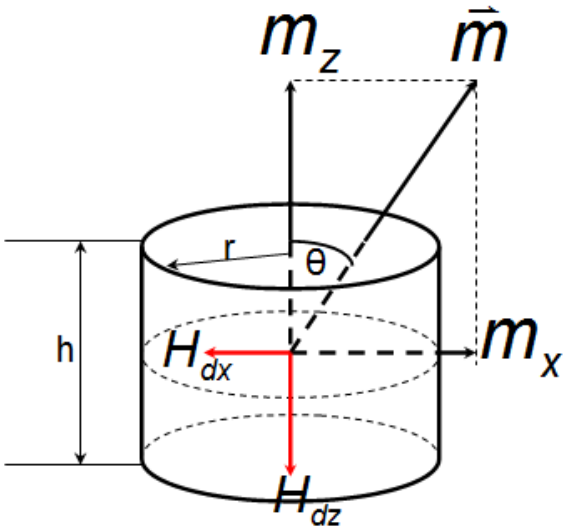

Figure 2.1 Demagnetization field from the uniform magnetization inside the cylindrical single domain nanomagnet.

The demagnetization field is, calculated after integration,[15]

$$H_{dz} = -2\pi M_S m_z h\left(\frac{1}{\frac{h}{2}} - \frac{1}{\sqrt{r^2 + \frac{h^2}{4}}}\right) = -M_S m_z \cdot N_z$$

$$H_{dx} = -\pi M_S m_x \frac{h}{\sqrt{r^2 + \frac{h^2}{4}}} = -M_S m_x \cdot N_x$$

As shown in Figure 2.1, r and h are the radius and height of the nanomagnet cylinder, respectively; and N_z, N_x are the demagnetization factors of the nanomagnet. It is worth of noticing that $N_z + 2N_x = 4\pi$, which agrees with the ideal ellipsoid single domain Stoner-Wohlfarth particles.[9]

The crystalline anisotropy field $\vec{H}_u^{\omega}$ is derived from the crystalline anisotropy energy [8]

$$E_u = -K_u \cdot \cos^2\theta = -K_u(\vec{m}\cdot\hat{z})^2 = -\frac{K_u}{M_S^2}(\vec{M}\cdot\hat{z})^2$$

thus

$$\vec{H}_u = -\frac{\partial E_u}{\partial \vec{M}} = \frac{2K_u}{M_S^2}\hat{z}(\vec{M}\cdot\hat{z})$$

where K_u is the first order crystalline anisotropy factor, and $\hat{z}$ is the unit vector along the uniaxial easy axis of the nanomagnet.

Each component of the stochastic thermal field is determined by [6, 7]

$$H_{th} = N(0,1)\sqrt{\frac{2\alpha k_B T}{M_S^2 V \cdot \Delta t}}$$

where $N(0,1)$ is the unit Gaussian random function (recalculated each Δt) and V is the volume of the nanomagnet.

2.2 Perpendicular media simulation

The system studied is a small ordered two-dimensional cluster of interacting three-dimensional single domain magnetic nanoparticles, each having uniaxial anisotropy with easy axis perpendicular to the cluster plane for the perpendicular media. In all cases studied here the applied field is oriented parallel to the easy axis. The physics of magnetization reversal for a nanoscopic single domain magnetic particle having uniaxial anisotropy is well described by the Stoner-Wohlfarth (S-W) model.[9] Whereas the hysteresis loop of a single nanoparticle is square [Figure 1.4 (a)], the hysteresis loop of a cluster will have multiple magnetization steps [Figure 1.4 (b)].

An important property of the nanomagnet cluster for the purpose of multilevel information storage is to have distinct, well-separated steps on the total magnetization

curves. For this purpose it is important to understand the physics underlying the magnetization reversal fields corresponding switching between states. The shape of hysteresis curve depends on the "intrinsic" nanomagnet properties, e.g. saturation magnetization, shape of the particles, and magnetization anisotropy. It also depends on extrinsic parameters, e.g. temperature, applied field sweep rate, and the overall geometry of the cluster. [4, 8, 10]

To evaluate the statistical probability distribution of switching field values analytically, the free energy barrier for switching must be determined. Let us first examine the case where only one single nanomagnet is present. In order to switch the nanomagnet from one stable state to the other, one needs to apply an external field in the other direction. In another terms, the initial state of the nanomagnet has the magnetization aligned along the $\hat{z}$ direction. The external field H_z is applied on the opposite orientation. For this initial state, the crystalline anisotropy energy is the lowest while the Zeeman energy is the highest, and the total free energy density is

$$E_i = (E_d + E_u + E_Z)\Big|_{initial}$$

θ is 0 for the initial state, so the initial demagnetization energy density is [1, 8]

$$E_d\Big|_{initial} = -\frac{1}{2}\vec{H}_d \cdot \vec{M} = -\frac{1}{2}(-N_z\vec{M}) \cdot \vec{M} = \frac{1}{2}N_z M_S^2$$

The initial crystalline anisotropy energy density is [4, 8]

$$E_u\Big|_{initial} = -K_u \cos^2\theta = -K_u$$

The initial Zeeman energy density is $E_z\Big|_{initial} = -\vec{H}_a \cdot \vec{M} = H_a M_S$. Therefore the total free energy density is

$$E_i = (E_d + E_u + E_Z)\big|_{initial} = \frac{1}{2}N_z M_S^2 - K_u + H_a M_S$$

The competition between these energies terms will cause the magnetization vector to rotate. The global free energy minimum state for the system is to have the magnetization to be aligned along the $-\hat{z}$ direction (along the applied field). The most important issue during the switching is to determine the free energy barrier through the precession from the initial state to the final state.

The general expression for the free energy of the nanomagnet in the applied field (along the $-\hat{z}$ axis), depending on the angle θ between the $\hat{z}$ axis and the magnetization vector, can be written as $E_\theta = (E_d + E_u + E_Z)$, and the terms in this formula are

$$E_d(\theta) = -\frac{1}{2}\vec{H}_d \cdot \vec{M} = -\frac{1}{2}(-N_z M_z \hat{z} - N_x M_x \hat{x}) \cdot \vec{M} = \frac{1}{2}(N_z M_S^2 \cos^2\theta + N_x M_S^2 \sin^2\theta)$$

$$E_u(\theta) = -K_u \cos^2\theta$$

$$E_Z(\theta) = -\vec{H}_a \cdot \vec{M} = H_a M_S \cos\theta$$

We can calculate the angle θ_0 at which the E_θ reaches maximum by solving the equation

$$\frac{\partial E_\theta}{\partial \theta}\Big|_{\theta_0} = 0$$

which refers to [1]

$$\cos\theta_0 = -\frac{H_a \cdot M_S}{2K_1 - M_S^2(N_{//} - N_\perp)}$$

The free energy density barrier for the switching of the nanomagnet at the given applied field (along the $-\hat{z}$ axis) can be derived as [1]

$$\frac{E_B}{V} = E_{\theta_0} - E_i = (1-\cos^2\theta_0)[K_1 - \frac{1}{2}M_S^2(N_{//} - N_{\perp})] + H_a \cdot M_S(1-\cos\theta_0)$$

At zero temperature, a single isolated nanomagnet switches at the critical field at which the free energy barrier (determined by the magnetocrystalline and shape anisotropies) for magnetization reversal vanishes. At finite temperatures, the hysteresis loop is no longer perfectly symmetric. The switching field values are not exactly reproducible -- they acquire a statistical distribution due to the stochastic thermal agitation. To study the switching process of the single Stoner-Wahlfarth nanomagnet by simulation, the applied field is swept at a constant rate. This means the energy barrier of the switching during the process is constantly changing as well. The energy barrier scaling with volume can be compared to the k_BT to estimate the thermal stability. For an isolated Stoner-Wohlfarth particle with the external field H applied along the easy axis, the switching energy barrier can be written as [8]

$$E_B(H) = K_u V(1 - \frac{H}{2K_u / M_S})^2$$

where K_u is the effective uniaxial anisotropy. It shows that free energy barriers decrease with the particle size. When K_uV is comparable to k_BT the magnetization fluctuates very rapidly, which is known as superparamagnetism. In more detail, the stability condition is defined by

$$\frac{K_u V}{k_B T} \geq 25$$

which indicates the average life time for a certain bi-stable state under the given temperature is 100 seconds. For a grain to be stable for 10 years (3×10^8 s),

$\frac{K_u V}{k_B T} \geq 40$. On the other hand, the magnetization of a grain of volume V = (5 nm)^3 and anisotropy $K_u = 4\times10^6$ erg/cm^3 is thermally unstable at room temperature, because $\frac{K_u V}{k_B T} = 12$.

Consider the following experiment: at the initial time $t = 0$, the nanomagnet is not switched, and stays at the initial state with the magnetization vector pointing to the $\hat{z}$ axis. One starts to apply an external field $H(t)$ swept at a constant rate. At a later moment t, the probability for the nanomagnet to *stay* un-switched is $P(t)$, which can be expressed as [10, 11]

$$\frac{dP}{dt} = -\frac{P}{\tau}$$

This leads to

$$\ln P\Big|_0^t = -\int_0^t \frac{dt}{\tau}, \qquad P(t) = \exp(-\int_0^t \frac{dt}{\tau})$$

Note here [12, 13, 14]

$$\tau^{-1} = f_0 \cdot \exp(-\frac{E_B}{k_B T})$$

$dt \cdot \frac{P}{\tau}$ is the probability for the nanomagnet to switch during the time interval $(t, t+dt)$, and similarly

$$dH \cdot \frac{P}{\tau} \cdot \frac{dt}{dH}$$

is the probability for the nanomagnet to switch during the applied field interval $(H, H+dH)$.

As a performance check, we compared the switching simulation results of a single nanomagnet to the predictions of analytical theory, using the theoretical derivation above. The simulation using LLG equation was repeated 1000 times in order to build large enough sample space, for the purpose to be compared with the stochastic thermal dynamic analytic calculation. Material parameters [4] of Co_3Pt are chosen for the simulation: Saturation moment density $M_S = 1100$ emu/cm^3, first order uniaxial crystalline anisotropy constant $K_u = 2.0 \times 10^7$ erg/cm^3. The applied field sweep rate is 5×10^8 Oe/s, which is applied to lower the computation time cost of the simulation. In the LLG equation $\frac{d\vec{m}}{dt} = \frac{\gamma_0}{1+\alpha^2}\vec{m} \times (\vec{H}_{Total} - \alpha\vec{m} \times \vec{H}_{Total})$, we set the damping term to be $\alpha = 0.8$. The switching is simulated at temperature of 300 K. A discrete time interval Δt is set to be 5×10^{-14} second,[6, 7] such that it is small enough for the fluctuating thermal field $H_{th} = N(0,1)\sqrt{\frac{2\alpha k_B T}{M_S^2 V \cdot \Delta t}}$ to be approximately considered constant during $(t, t + \Delta t)$.[6, 7] During each time interval $(t, t + \Delta t)$, the $\vec{H}_{Total}$ is re-calculated by the summation $\vec{H}_{Total} = \vec{H}_a + \vec{H}_n + \vec{H}_d + \vec{H}_u + \vec{H}_{th}$, then update the magnetization vector $\vec{m}$ by the LLG equation, and rinse and repeat afterwards.[1, 6, 7] The result is shown in Figure 2.2 as the gray colored histogram.

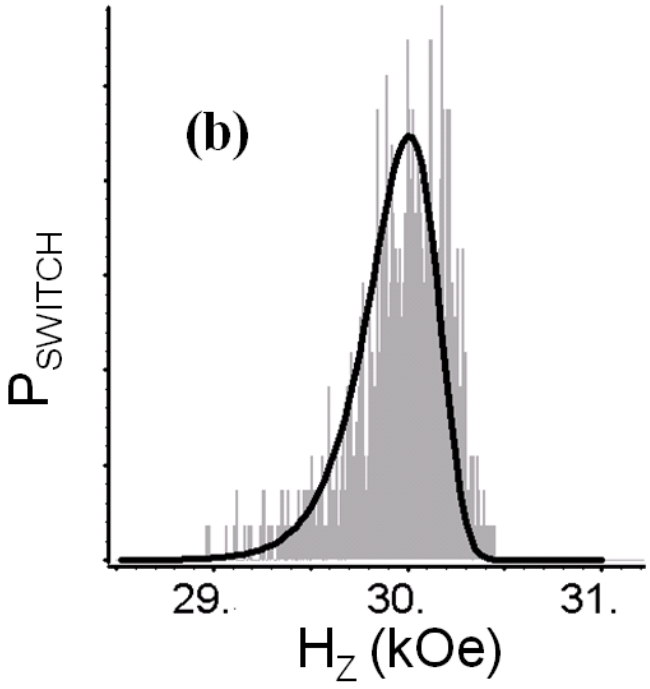

Figure 2.2 LLG simulated switching probability histogram (gray histogram) for a single isolated nanomagnet and the analytical prediction (solid line) (Reference 1)

According to the energy barrier formula derived previously, the analytical prediction of the switching field distribution is calculated and plotted in Figure 2.2 as the solid line. Figure 6 shows the analytical curve fits with the 1000 LLG simulated runs of a single nanomagnet switching, using $f_0 = 2.18 \times 10^{11}$ Hz [1] as a fitting parameter.

The next simulation work we did is on a cluster of seven nanomagnets arranged in a *symmetric* hexagonal pattern. This pattern of the clusters was demonstrated by experimental work done [5] by Prof. Thomas Russell's group at UMass Amherst, as shown as an inset in Figure 2.3. One randomly selected LLG simulated switching curve for such a cluster of seven nanomagnets is plotted in Figure 2.3.

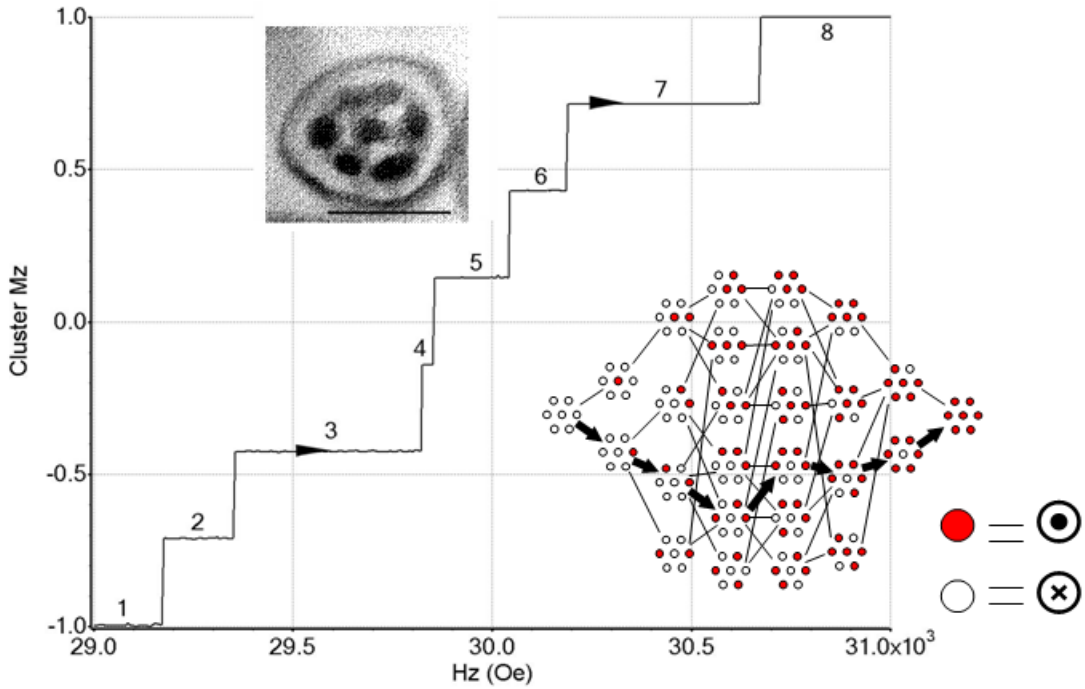

Figure 2.3 A randomly chosen switching curve for the symmetric 7-dot cluster at 300K using a LLG simulation. The SEM inlet picture shows the experimental prototype structures formed by diblock copolymer self assembly. The bold arrows on the switching path map correspond to the 8 steps on the hysteresis. The TEM image shows the direct experiment support to this concept from Prof. Thomas J. McCarthy's and Prof. Thomas P. Russell's research groups in the reference work. (Reference 5)

For the simulation, temperature is set to 300 K and the field sweep rate is set to 5×10^{8} Oe/second. The distance between the nearest neighboring nanomagnets in the cluster is set to 30 nm. The first result we should notice is the stepwise hysteresis loop. The curve has 8 distinctive steps with 8 different total perpendicular magnetization values, which matches our prediction and expectation for the multiple state storage devices. Secondly, the arrowed path highlighted in the switching pathway map (inlet of Figure 2.3) corresponds to the specific switching process plotted in the hysteresis curve. At finite temperatures, thermal agitation activates multiple possible pathways for switching: the cluster is not restricted to follow only the path involving the lowest

energy barriers of switching, but also other alternate switching paths with energy barriers comparable to $k_B T$. The map of switching pathways shows all the possible switching transitions for a symmetric hexagonal 7-dot cluster. For repeated simulations at non-zero temperatures, the cluster will not necessarily follow the same switching path, but rather take a variety of random paths producing a statistical distribution of switching field values. The physics related to the switching field distribution is complicated and the stochastic behavior of the cluster is not appreciated by the purpose of using the clusters for data storage devices, due to the uncertainty of switching processes. Thirdly, there is a huge storage density loss with the 7-dot design in comparison with other designs. With 7 bits in the cluster, one can store different information by up to 7+1=8 states. In the traditional binary bit media, if possible, one can have 2^7 different sets of states. The stability of the remanent states is studied for the purpose of holding the information saved after turning off the applied field in the simulation. The calculation shows that the energy barrier of changing the remanent states at zero applied field is about the magnitude of 10^{-11} erg. Compared to the thermal agitation strength $k_B T = 4.14 \times 10^{-14}$ erg at 300 K, the energy barrier is so large that the probability of switching to another remanent configuration is practically negligible. The simulation verifies the observation of remanence for long times after turning off applied field.

In a cluster with N 3D uniaxial nanomagnets there are 2N angular degrees of freedom needed to fully describe the dynamics of the N magnetization vectors; thus principally the free energy barrier for switching one specific nanomagnet is a function of 2N variables. This full treatment is difficult to calculate. The LLG simulation shows

that while one nanomagnet switches the other nanomagnets in the cluster experience only small perturbations around their easy axes. This inspires a simplification that all the other nanomagnets keep their magnetizations constant along their easy axes while one nanomagnet switches, such that the free energy barrier depends on only two variables. This means cluster switching processes are approximated as the switching process of a single nanomagnet under the applied field and a constant (dipolar) interaction field from the neighbors. Thus for a specific nanomagnet, the switching field is the switching field for a single isolated nanomagnet modified by the interaction field. By assuming that the interaction between nanomangets is a point dipole-dipole interaction and that the nanomagnets switch one by one, the placement of the steps on the hysteresis loop can be calculated and understood simply. Essentially, the physics is reduced to the switching of an isolated nanomagnet, but with a field shift calculated from the specific initial cluster state. This enables straightforward analytical calculations of the cluster switching behavior and stability of remanent states at non-zero temperatures.

Changing the geometry of the cluster in some way will change the most probable switching paths and the applied field values around which the switching events occur. This can be used as a tool to make states of the cluster with different total perpendicular magnetization more distinguishable from each other in the hysteresis curve. An example is illustrated in Figure 2.4 below.

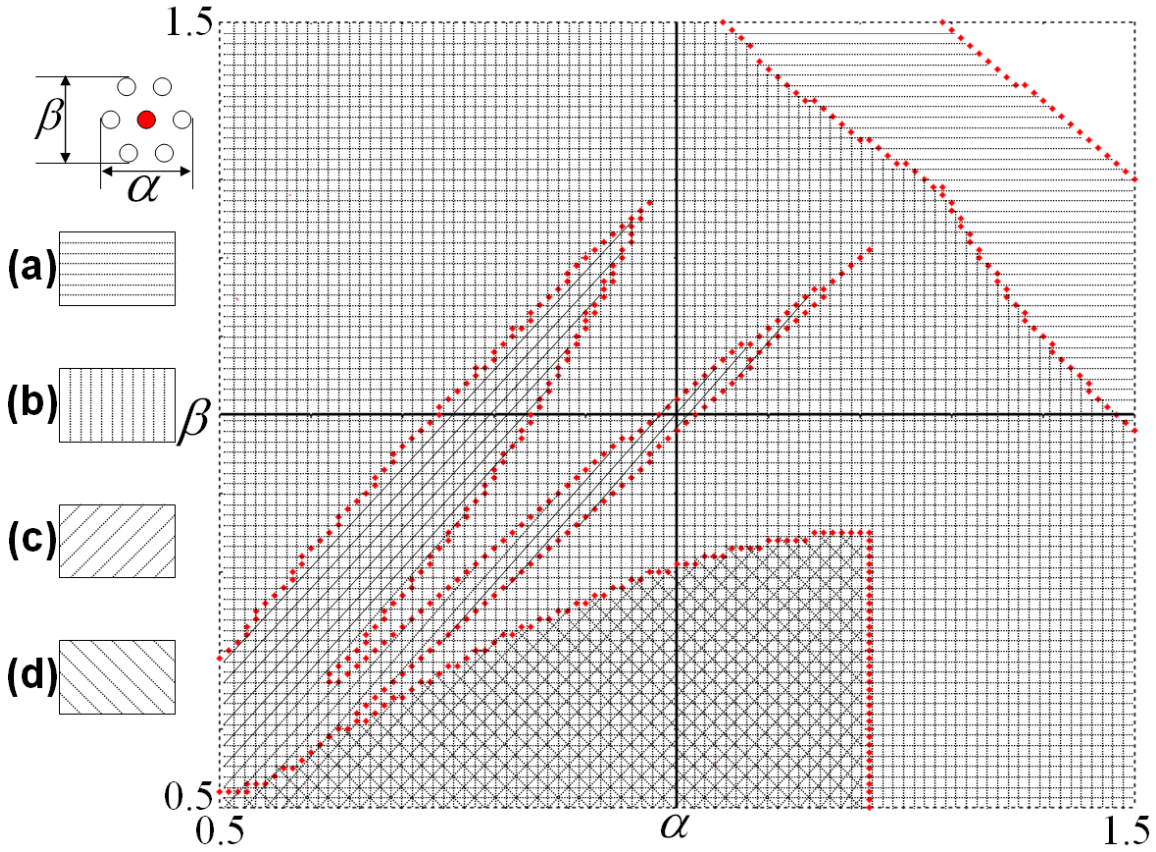

Figure 2.4 A map showing the effects of introducing asymmetry to the nanomagnet cluster. The demarcated regions indicate where the switching field for a particular transition is well separated from the previous switching transition. (Reference 1)

At 5 K, a field sweep rate of 10^8 Oe/s, and with the fitting parameters acquired from simulation, the analytical calculation shows that if the different constant interaction field shifts of two competing switching events are more than 65 Oe apart, the probability for the less probable event to happen is lower than 5%. The most probable switching paths for an interacting nanomagnet cluster with a particular geometry can be evaluated using this 65 Oe criterion. Figure 2.4 shows how changing the physical geometry of the 7-dot cluster can modify the switching curves under the given conditions. In the figure, α and β are the distortion factors along the horizontal and vertical cluster symmetry axes, ranging from 0.5-1.5 corresponding to from

compressed to 50% to elongated to 150% of the original (symmetric) hexagonal cluster scale. In the general (asymmetric) case, the *first* switching event will involve a transition from the initial state to a state in which one nanomagnet has switched (M_Z = -7 to M_Z = -5). Region (a) in Figure 2.4 shows the range of distortion that ensures that the most probable first switching event to happen will be the one in which the center nanomagnet has switched. Region (b) will ensure that the most probable *second* switching events (M_Z = -5 to M_Z = -3) happen at applied field values that differ from the first switching fields by a minimum criterion value. In other words, this criterion ensures that the switching field distributions of the first and second switching events do not overlap substantially. The second and third switching events are less distinguishable. The criterion used to draw region (c) is that the most possible switching fields of the third switching events are at least 10 Oe higher than the second switching event. Stricter criteria will shrink the qualifying region extremely. Region (d) defines the distortion that separates the third and fourth switching events by a 150 Oe criterion. After the fourth switching event, the overlapping of different switching transitions is unavoidable at all values of cluster distortion. Note that the discussion above is not appropriate for the distortion near the most compressed edge (α and β both close to 0.5) because of the dipolar interaction approximation, although it is drawn in the figure.

As we pointed out previously, the 7-dot cluster design has several drawbacks preventing easy implement for applications, due to the complicated switching state network and the stochastic nature of the switching process. Instead, we turned our

focus to the design of interacting cluster of *three* nanomagnets with equilateral triangular symmetry. With three bits in the binary media, one can have up to 8 different states; with a three-dot interacting cluster counted as one basic unit in the media, one can have up to 3+1 = 4 different states. We only lose half of the storage density, which is a significant improvement compared to the 7-dot cluster design. Furthermore, the switching physics is much more simplified. Let us recognize the dots

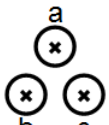

in the cluster with the codes as . There are three possible ways to switch only one in the cluster: we can switch either of the dots a, b, c. Consider dot <a> is going to be switched during this step of experiment. Using dipolar approximation, the actual magnetic field on dot <a> during the switching, is the combination of the applied field and the interaction field from its two neighbors – dot <b> and <c>. So, the switching distribution of this particular event can be evaluated as the distribution of a single nanomagnet switching with a shift of constant applied field value, as shown next:

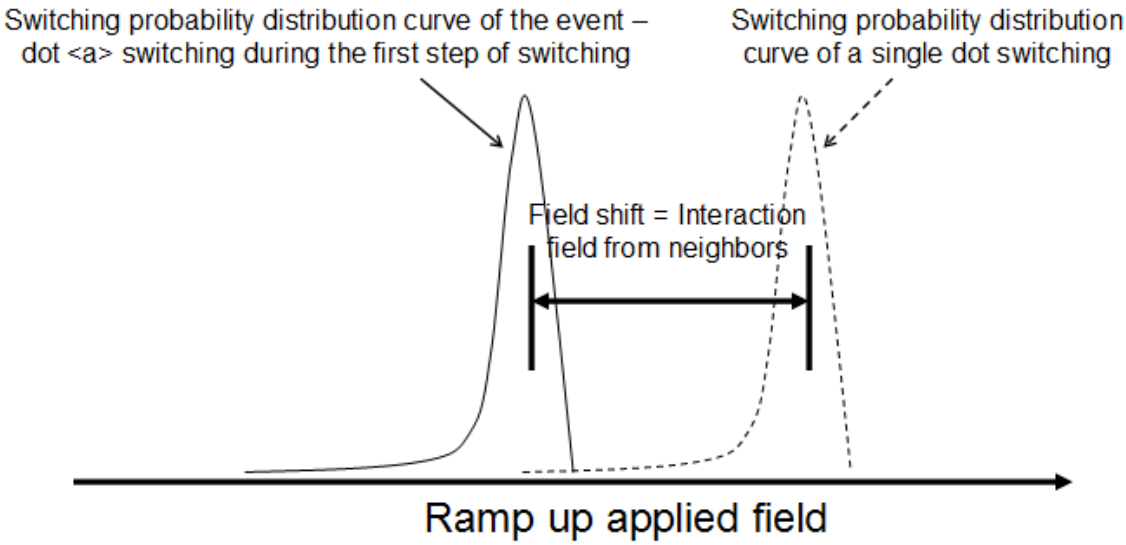

Figure 2.5 Switching probability distribution curve of the first switching event in the 3-dot cluster compared to that of the single isolated nanomagnet.

Now consider dot <b> or <c> is going to be switched during this step of experiment. Following the same derivation in the previous section, the switching probability curves for these two events are exactly same as the switching probability distribution curve of the event switching dot <a>. This is because, due to the perfect symmetry, the interaction fields from neighbors are exactly the same in all of the three cases.

Consider the switching processes of the second nanomagnet in the cluster. There are six different possible events counting the three initial configurations and three final configurations, as shown in Figure 2.6.

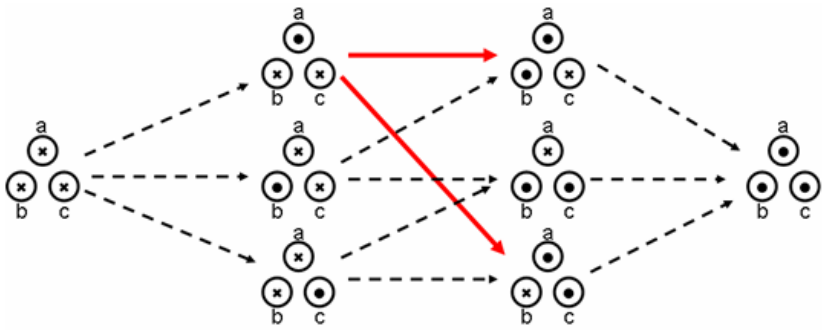

Figure 2.6 Complete switching event network of the equilateral triangular 3-dot cluster

Due to the symmetry of the cluster, all of the initial configurations have the same magnetostatic energy; all of the final configurations have the same magnetostatic energy; and all of six switching events have the same energy barrier. This leads to the conclusion that we can simplify the complete switching event network, shown in Figure 2.6, to the one shown in Figure 2.7. Therefore, the switching field distribution can be well separated and studied with great ease. And because of this reason, we put the majority of our fabrication efforts on the projects using the equilateral triangular three-dot cluster design.

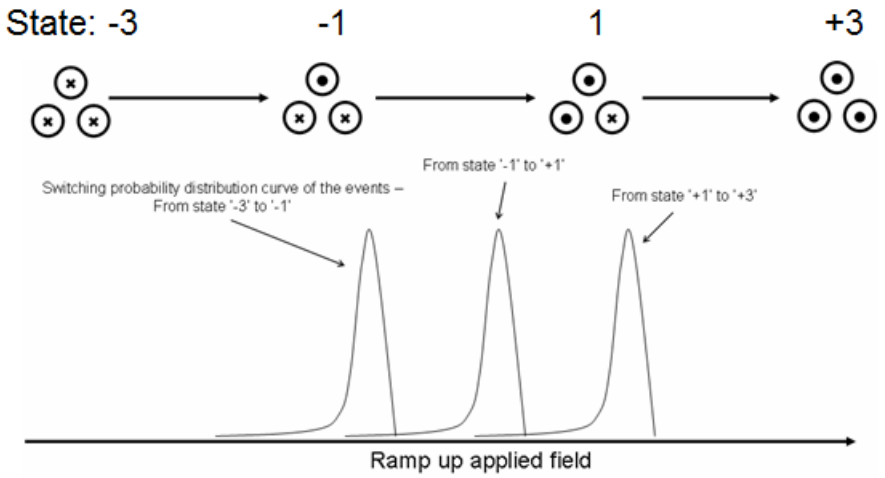

Figure 2.7 Simplified switching pathway of the equilateral triangular 3-dot cluster, and the corresponding switching field distribution curves

2.3 Simulations of the in-plane clusters

Simulation work of nanomagnet clusters for in-plane media has also been done. The work is based on the material's parameters of permalloy ($Ni_{80}Fe_{20}$). Permalloy is a magnetically soft magnetic material that has negligible crystalline anisotropy. [4] The flat disk shape of the nanomagnets is the same as the one described in the perpendicular media section. Defined by the shape of the nanomagnets, the most energetically favorable magnetization configuration is to have all the nanodots magnetized in the cluster plane.[8] For all the simulation work in this section the applied field is also in the cluster plane.

The magnetic behavior of the in-plane nanomagnet clusters depends on the shape and the overlay of the nanomagnets. For example, novel distinctive simulated hysterisis loops were observed for different external field orientations during ideal

micromagnetic simulation without considering the thermal agitation, which are shown in Figure 2.8 below. The results indicate effective easy and hard axis. When the applied field is along the effective easy axis, which is any of the six-fold symmetry axes, the cluster forms “vortex” states during the switching processes. In the “vortex” states, the magnetization of the six outmost nanomagnets are lined up and looped in a closed vortex, with small contribution to the net in-plane cluster magnetization. And the major contribution of the net in-plane cluster magnetization comes from the central nanomagnet. When the applied field is along the effective hard axis, which is one of the two-fold mirror reflection symmetry axes, the cluster does not form the vortex states during switching; instead, zigzag patterns were observed. In Figure 2.8, the effective easy and hard axes are labeled as the x and y axes, respectively. And the inlets of the images of cluster in-plane magnetization (vortex state and zigzag state) are real time observation taken during the micromagnetic simulation.

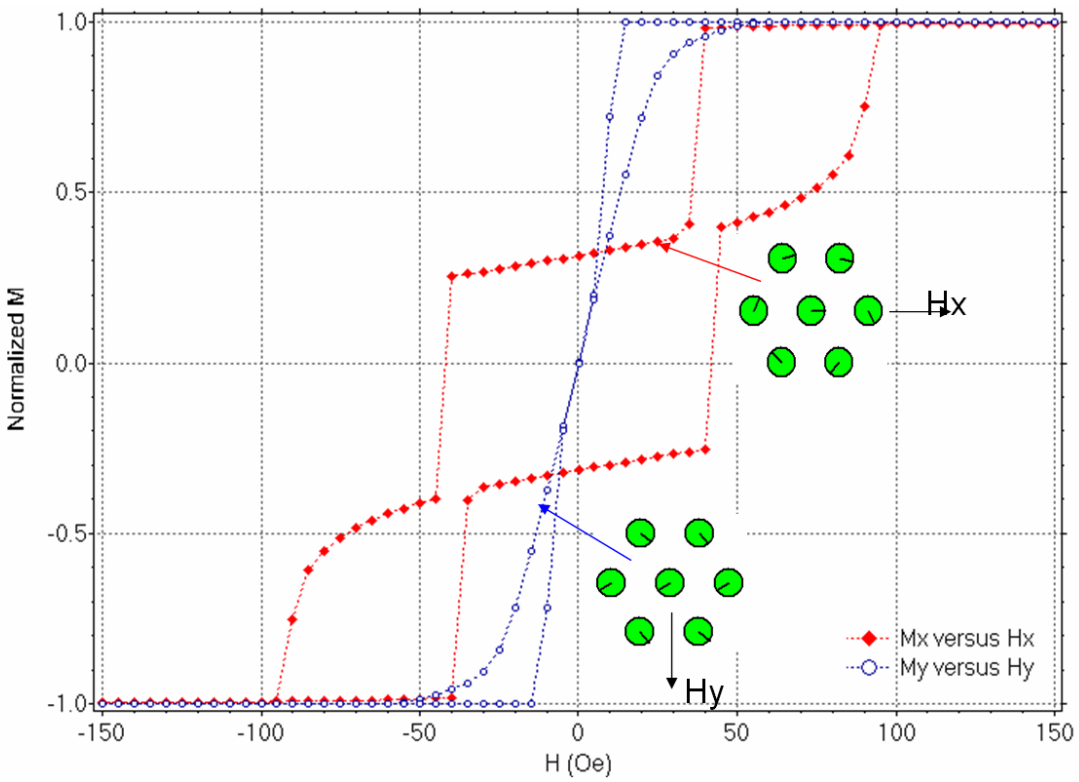

Figure 2.8 Simulated hysterisis loops of the in-plane Permalloy nanomagnet cluster without considering the thermal agitation. *Red curve*: Field applied along the effective easy axis of the cluster. *Blue curve*: Field applied along the effective hard axis of the cluster. *Images of the in-plane magnetization of the cluster*: Snap shots of the cluster's magnetization states during the simulation, and the directions of the short lines started from the centers of the nanomagnets indicate the orientations of the in-plane magnetization of the nanomangets.

Because of the nanoscale of the individual magnet, at sufficient high temperatures the system is turned into the super-paramagnetic states. The magnetization of the nanomagnets are stirred by the thermal fluctuation, the net magnetization at zero applied field is zero along any directions. In the simulation, we observed the super-paramagnetic behavior at temperatures as low as 5 K. This means the cluster magnetization is very sensitive to the temperatures. Figure 2.9 shows an example how the switching curves of the cluster are tuned by temperatures. The

dramatic fluctuations indicates certain switching patterns were activated by thermal agitation under 2 K. These switching patterns were not accessible under the ideal simulation case without considering the thermal agitation.

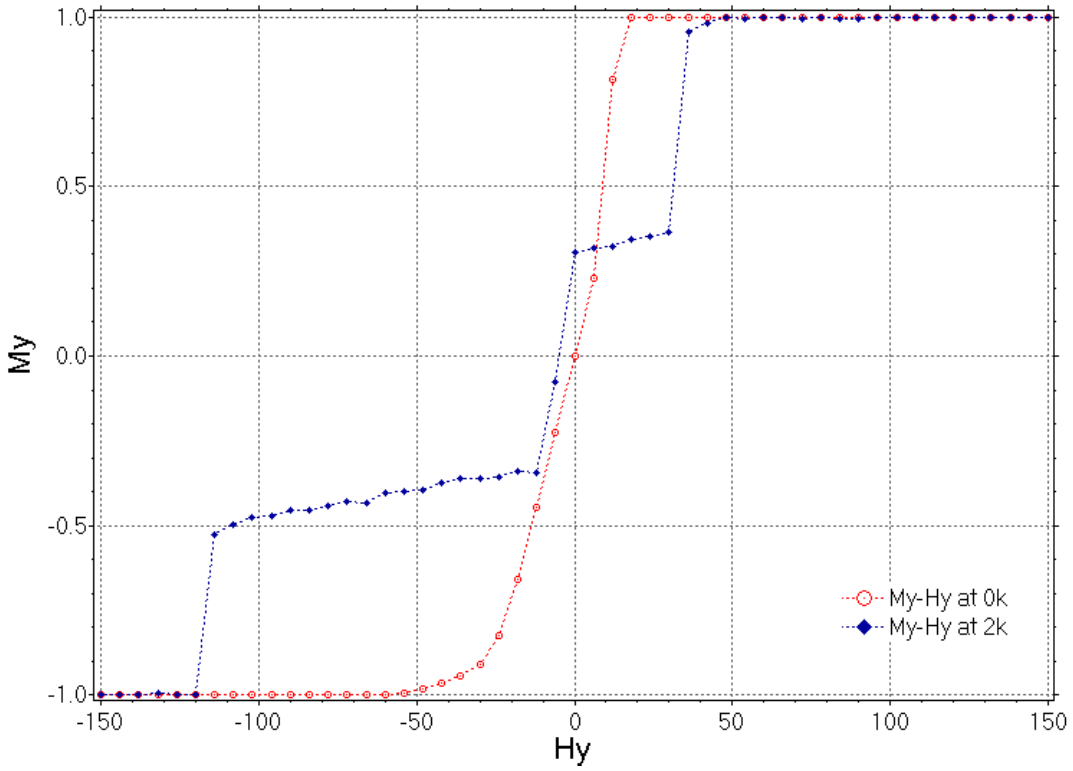

Figure 2.9 Half of the hysteresis loops for symmetric in-plane 7-dot cluster, tuned by temperatures.

Also, the switching of the cluster can be tuned by distortion of the cluster's geometry. Figure 2.10 shows an example how the switching curves are tuned by distortion alone the Y axis without considering the thermal agitation.

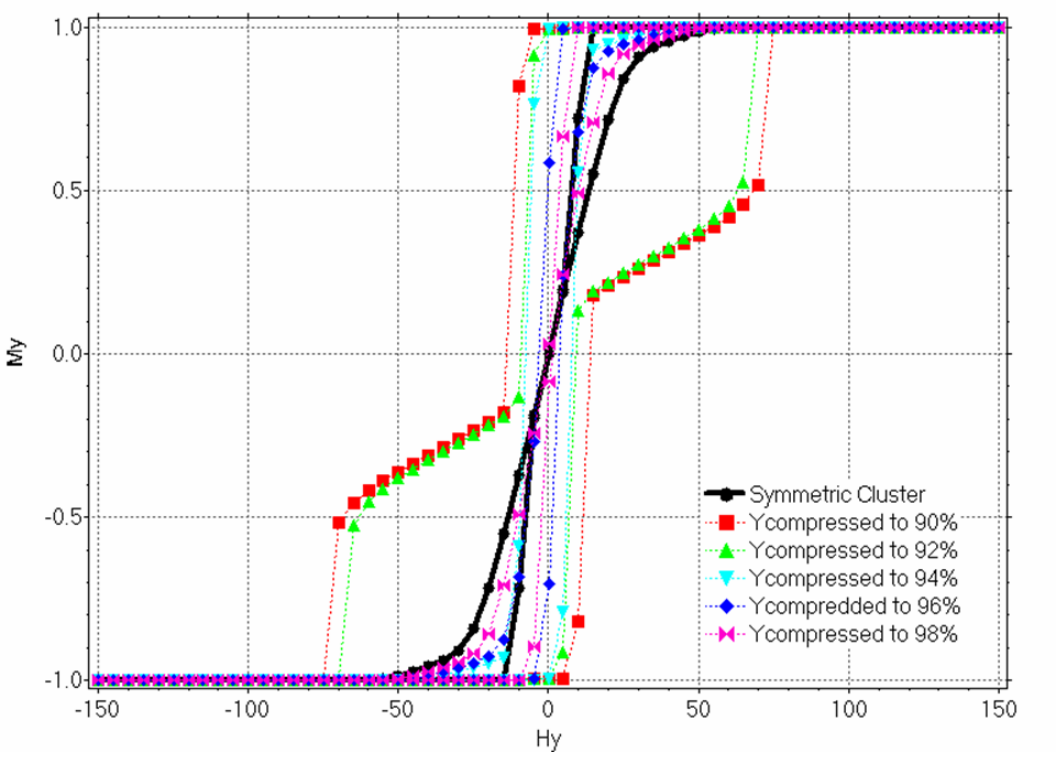

Figure 2.10 Half of the hysteresis loops for symmetric in-plane 7-dot cluster, tuned by distortions.

The noticeable change of the hysteresis loops in Figure 2.9 and Figure 2.10 is due to the re-selection of the most energetically favorable switching pathways. The thermal agitation gives the cluster enough probability to overcome the energy barrier for changing the switching pathways. Distortion can change the overall energy mapping so at certain distortion points the most favorable switching pathway is changed.

2.4 References

1. Q. Xiao, R. V. Krotkov, and M. T. Tuominen, *J. of Appl. Phys*., **99**, 08G305 (2006)

2. M. Albrecht, G. Hu, A. Moser, O. Hellwig and B. D. Terris, *J. Appl. Phys.*, **97**, 103910 (2005).

3. G. Bertotti, *Hysteresis in Magnetism* (Academic Press, 1998).

4. D. Jiles, *Introduction to Magnetism and Magnetic Materials*, (Chapman & Hall, 1998)

5. H. Xiang, K. Shin, T. Kim, S. I. Moon, T. J. McCarthy and T. P. Russell, *Macromolecules* **37**, 5660 (2004)

6. G. Brown, M.A. Novotny, and P.A. Rikvold, *Phys. Rev. B.* **64**, 134422 (2001)

7. G. Brown, M.A. Novotny, and P.A. Rikvold, *J. Appl. Phys.* **87**, 4792 (2000)

8. D. J. Sellmyer, M. Zheng and R. Skomski, *J. Phys. Condens. Matter* **13**, R433 (2001)

9. E.C. Stoner and E.P. Wolfarth, *Phil. Trans. R. Soc. Lond., A,* **240**, 599–642 (1948)

10. R. Skomski and J. M. Coey, *Permanent Magnetism* (Bristol: Institute of Physics, 1999)

11. P. Gaunt, *J. Appl. Phys.* **59**, 4129 (1986)

12. L. N´eel *Ann. Geophys*. **5** 99 (1949)

13. R. Street and J. C. Wooley, *Proc. Phys. Soc. A* **62** 562 (1949)

14. H. A. Kramers, *Physica* (Utrecht) **7**, 284 (1940)

15. H. Saito *et al., J. of Magnetism and Magnetic Mat.* **310**, 939 (2007)

CHAPTER 3

EXPERIMENTS ON NANOMAGNET CLUSTERS

In this work, we focused on the actual fabrication interacting cluster prototypes based on the schemes for multilevel information storage presented in previous section.[4] The eventual goal is the combination of advanced self-assembling block copolymer materials and lithographic patterning technology, to produce a well defined number of copolymer domains defined by local confinement to form hierarchically clustered nanomagnets for storage applications. The current project was designed to explore the feasibility of using such prototype structures as data storage devices.

3.1 Nanofabrication of proof-of-concept clusters

The key nanofabrication techniques for our samples include Electron Beam Lithography (EBL) on a suspended 100 nm silicon nitride membrane [4, 7] and metal deposition by thermal evaporation or alternatively pulse-reverse electrochemical deposition (PRECD).[8]

3.1.1 Ultra-high resolution EBL defining the cluster geometry

A goal in these proof-of-concept experiments was to study the properties of structures with dimensions comparable to the latest perpendicular nanomagnets fabricated with other viable advanced nanomanufacturing technologies. For example, using self-assembled diblock copolymers one can fabricate ordered arrays of sub-30

nm diameter nanomagnets.[1-3] It is a challenge to apply conventional EBL in order to fabricate the nanostructures with such small dimensions. [5] The resolution of EBL on normal substrates suffers from the backscattered electrons from the e-beam/substrate interaction, or in another term proximity effect. This is illustrated in Figure 3.1.[5] Typically with the instrument setups commonly used nowadays in the modern electron beam writers and scanning electron microscopes (acceleration voltage less than 50 keV), a fine beam of focused and collimated incident electrons can have a cross section diameter less than 10 nm,[4] but the effective exposure area on the e-beam resist layer can be much larger. This is one of the most important limiting problems of EBL.

One costly solution is to accelerate the e-beam to extremely high energies, such as 100 keV.[4] With such high energies the electrons will penetrate much deeper into the substrate, and the top resist layer will have less impact from the back scattered secondary electrons. This requires a specialized instrument which is not commonly accessible. In our instrument (JEOL JSM 6400 SEM equipped with a customized EBL module) we typically use acceleration voltage of 20 keV, which results in a significant proximity effect.

Alternatively, in our case, high resolution EBL was achieved with a much lower beam energy by using a PMMA e-beam resist layer spin-coated onto a 100 nm suspended SiN membrane.[6,7] The SiN membrane substrate was fabricated out of a double-coated SiN/Si/SiN wafer.[5] Low surface stress SiN membranes of 100 nm thickness were fabricated by low pressure chemical vapor deposition onto a silicon (1 0 0) wafer of 250 μm thickness, in order to control the mechanical properties variance between the SiN layer and the Si substrate and further protect the fragile SiN layer.

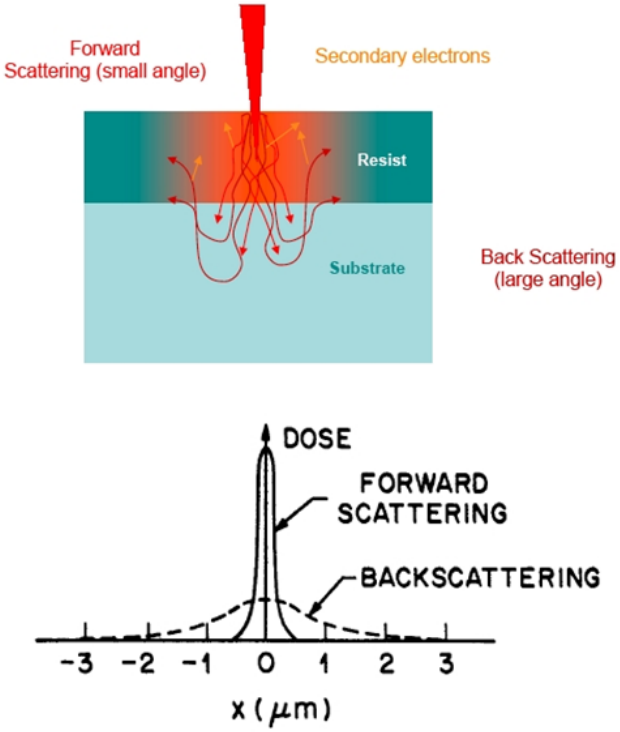

Figure 3.1 *Top*: Schematic illustration of the proximity effect during EBL. The incident electrons (red), backscattered electrons (red) and the production of the secondary electrons (orange) are shown in the picture. *Bottom*: Dose distribution of the forward scattering and backscattering at the resist-substrate interface. (Figure from reference 5)

First, the membrane window on the back side of the wafer is defined by chemical or mechanical etching. This process can be roughly done by roughing the designed widow with a diamond scriber as shown in Figure 3.2 (a), or precisely removing the designed region of SiN by focus ion milling. The bulk of silicon wafer exposed from the back side SiN opening is etched in 25% KOH (weight concentration) solution at 85 ^{o}C. The etching will most likely to go along the (111) silicon crystal planes because of the closest packing factor along this set of planes. The etching will

be stopped till the reaction reaches the SiN membrane on the other side and thus fabricate the suspended SiN membrane. This process is descried in Figure 3.2.

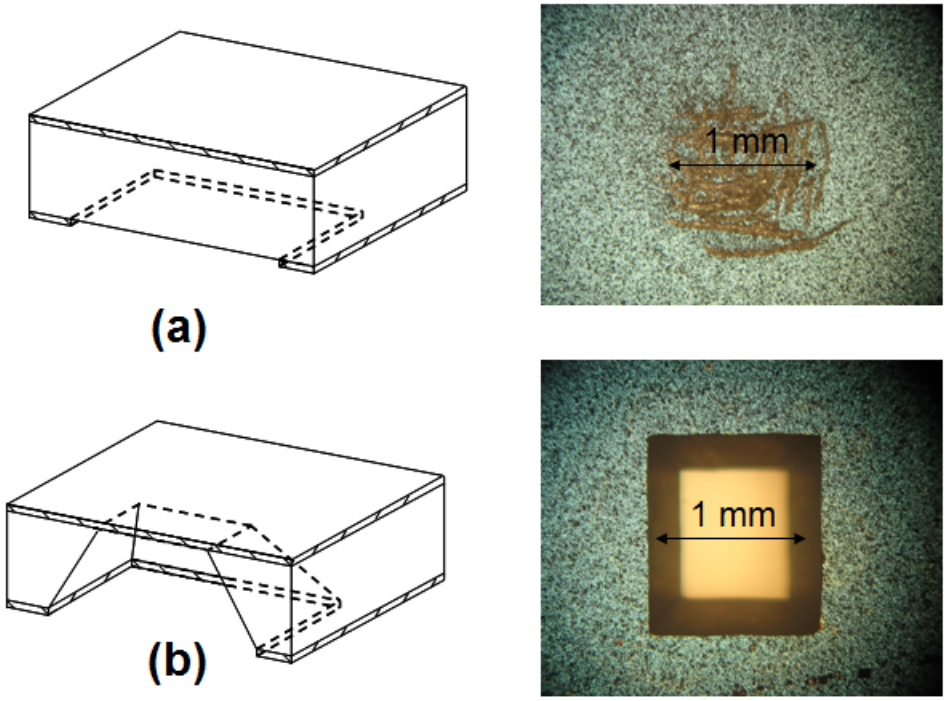

Figure 3.2 Fabrication of the suspended SiN membrane on silicon substrate. (a) Definition of the window opening on the back SiN side. The right side picture shows the random pattern generated by roughing the surface with a diamond scriber. (b) The suspended SiN window after the etching is stopped by the top layer of SiN membrane.

As shown in Figure 3.3, the EBL is now cast on a layer of 100 nm thick SiN suspended film. After the incident electrons penetrate through the electron beam resist layer (in our case it is a layer of 70 nm thick PMMA), they are further scattered by the SiN substrate. With the significantly reduced thickness of the substrate and therefore the interaction between the electron beam and the substrate, the backscattered electrons are significantly reduced. This results in reducing the proximity effect greatly effective and increasing the e-beam lithography resolution. [6, 7]

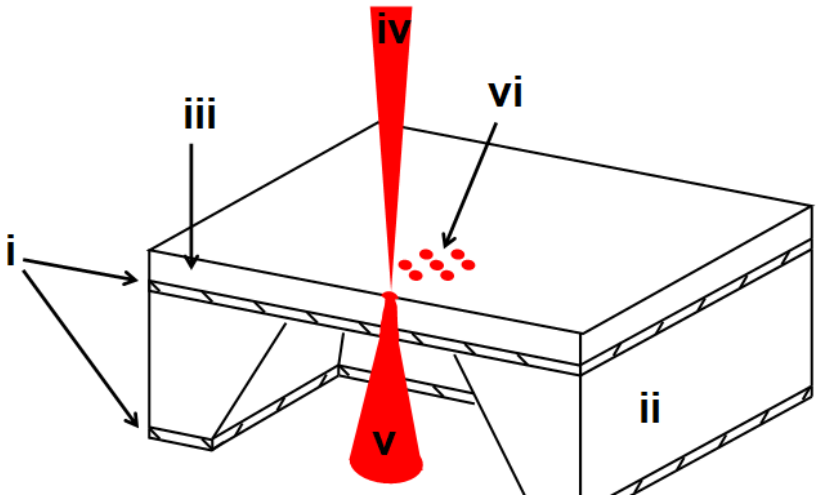

Figure 3.3 EBL on suspended SiN membrane, in which (i) 100 nm silicon nitride coating. (ii) Silicon wafer with (1 0 0) surface orientation. (iii) EBL working layer, e-beam resist only, or resist with metallic underlayer. (iv) Incident focused e-beam. (v) Transmitted e-beam. (vi) Array of patterns created by e-beam point exposure. (Reference 7)

The EBL was performed in point exposure mode in order to achieve the best possible lithography resolution. In this mode, the electron beam was allowed to expose only one single point on the resist film, blanked and then moved to another adjacent point for the next exposure, without overlapping of the effective exposed area of the neighboring points. A 20 kV e-beam acceleration voltage was used. For a 70 nm thick PMMA film, the exposure dosage for the best experimentally achieved resolution in our case [7] is 5.5 pA x 300 µs for one single exposure point, whereas for a 200 nm thick PMMA film, the optimal exposure was 5.5 pA x 700 µs. After exposure, the samples were developed in solution of IPA:water (3:1) at 5 ^{o}C for 30 seconds.[4]

3.1.2 Transferring the EBL pattern to nanomagnet clusters by metallization

After the nanoporous templates were fabricated by EBL, we used the patterns to create ordered metal nanodot arrays via evaporation or alternatively, electrodeposition. The first method we tried is thermal evaporation. Thermal evaporation is a typical top-down process for pattern transferring by heating a source material above its boiling temperature. One of the advantages of this method is the precise control of the evaporated thickness of the target material, up to the precision of $\overset{o}{A}$, with the aid of in situ deposition mass monitoring by QCM. It is suitable to perform evaporation for a single element source, but not necessarily for complex compound source materials, due to the difference between the boiling temperatures of the constituent elements. It is also limited by the boiling temperatures of the source materials, and not capable of evaporating metal elements with extremely high boiling temperatures. For many commonly used magnetic compounds, e.g. Co_3Pt, CoCrPt, Co/Pd, the best thin-film deposition method is by sputtering.[18]

The smallest structures made were arrays of nanodots of 30 nm diameter, which are comparable to the size of nanomagnets made by diblock copolymer template systems.[1-3] A unique advantage of this method is it can be adapted to fabricate clusters of nanomagnets of arbitrary geometries for prototyping experiments. In Figure 3.4 we show some proof-of-concept examples of complex cluster patterns fabricated by evaporation of Ag into the nanotemplate. The best resolution achieved so far is 30 nm diameter and 20 nm height nanodots, separated by 60 nm from center to center.

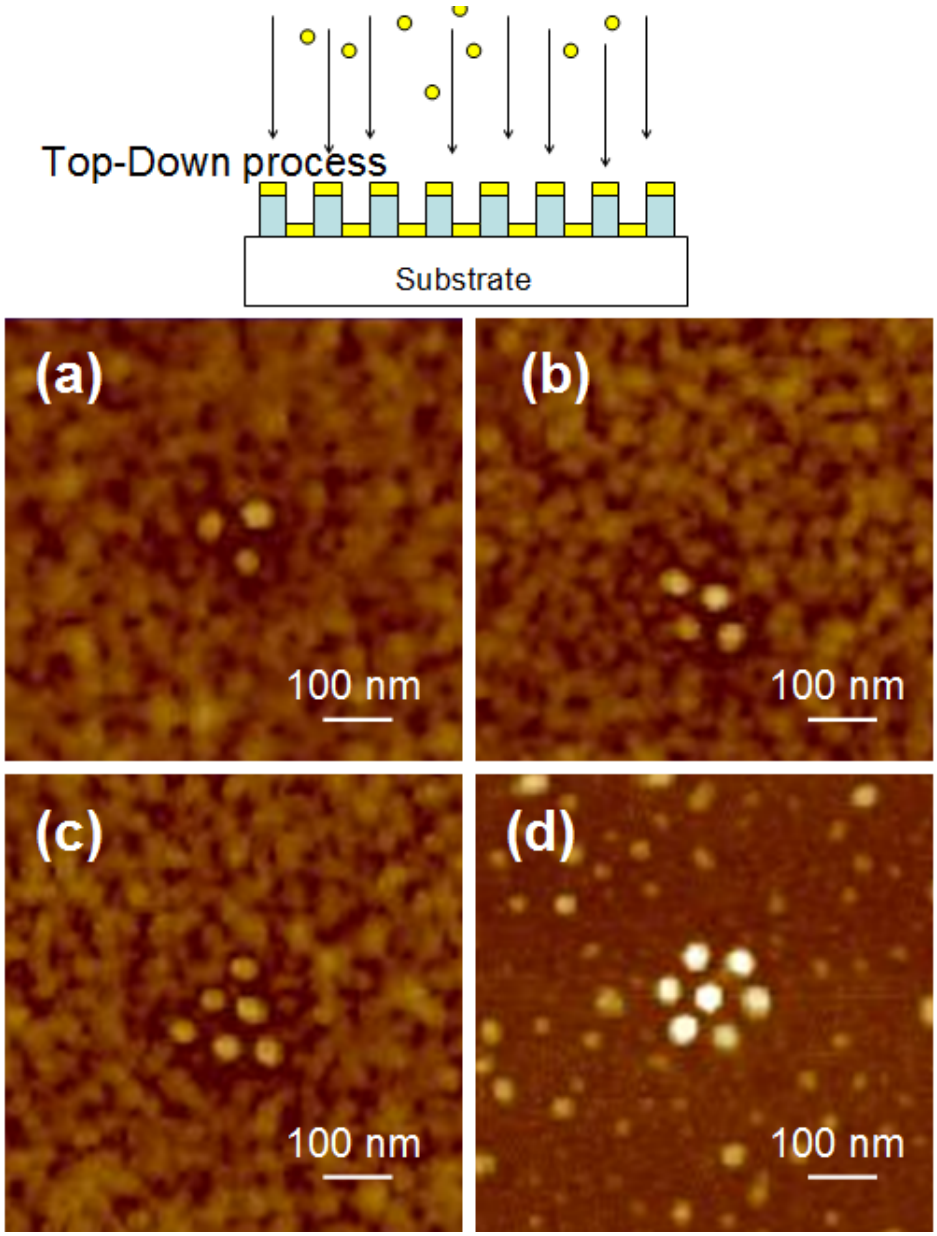

Figure 3.4 AFM height images of cluster structures fabricated by ultra high resolution EBL and evaporation. All nanodots are evaporated to 20 nm height, and 60 nm separated to the nearest neighbor(s). (a) Three Ag nanodots in a triangle cluster. (b) Four Ag nanodots in a quadrilateral cluster. (c) Six Ag nanodots in a triangle cluster. (d) Seven Ag nanodots in a hexagonal cluster. (Reference 7)

Unfortunately, it is not feasible to transfer the nanotemplates to the perpendicular interacting nanomagnet clusters simply by thermal evaporation. The high temperatures during this process will disturb the alignment of the deposited atoms along the desired easy crystalline axis. The deposited materials are most likely multiple grained and amorphous, without forming the required uniaxial magnetic anisotropy. A post-annealing process was reported [17] to be able to help rearrange the magnetic lattice structures and turn the deposited results to stronger ferromagnetic materials (e.g. FePt), but it is still difficult to control the orientation of the uniaxial easy axis of the compounds after the annealing.

Based on the previous work done by one of my colleagues Dr. Andrei Ursache, clusters of Co nanomagnets with perpendicular crystalline anisotropy were fabricated by the method of pulse reverse electrochemical deposition (PRECD).[8, 9] Electrochemical deposition (ECD) is one of the typical bottom-up nanofabrication methods.[10, 11] It has unique advantages such as cheap and fast process flows, capability of massive parallel production.[12, 13] Although, in our experience it is not easy to precisely control the amount of deposited materials by ECD. In order to gain accurate control of the deposition, the working (deposition) area on the sample must be somehow measured, and one has to be careful with all of the other experiment conditions. In the reference,[8] Dr. Andrew Ursache described how to achieve this by using a build-in QCM for in situ monitoring of the deposition mass. The PRECD is a carefully engineered AC electrochemical deposition method with two rotating phases.[8, 12, 13] Figure 3.5 shows the tuning of the perpendicular magnetic anisotropy of the deposited Co crystal structure.

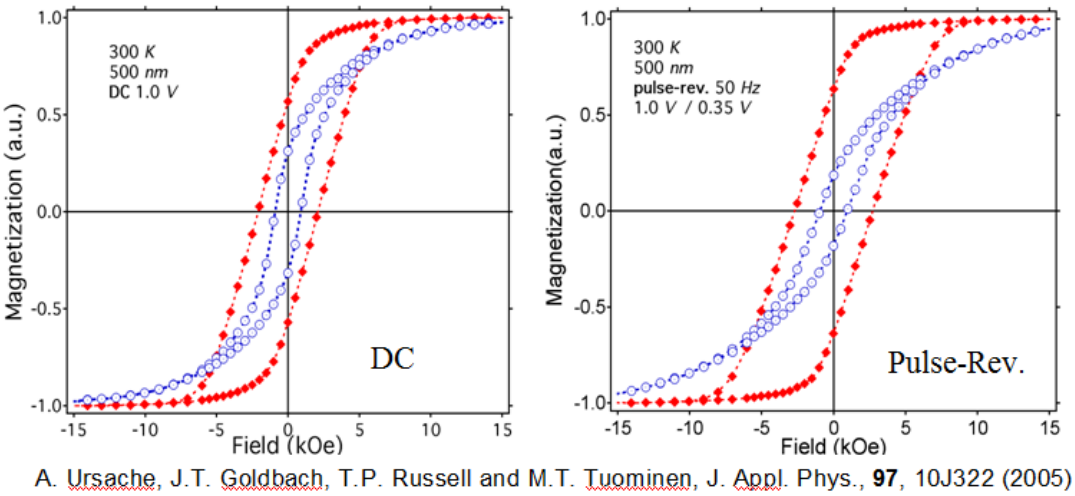

Figure 3.5 Tuning the perpendicular anisotropy of the deposited Co nanomagets. *Red curves*: hysteresis loop with the external field applied along the preferred nanomagnet easy axis. *Blue curves*: hysteresis loop with the external field applied perpendicular to the preferred nanomagnet easy axis. (Figure from reference 8)

In this case, a layer of 10 nm Ag was pre-evaporated onto the SiN surface prior to the preparation of the PMMA layer as the conductive electrode for subsequent electrochemical deposition. During the first pulse deposition phase, a high voltage (1 V from reference to working electrode in the cell) is applied so that the Co atoms are attracted and deposited into the nanotemplates. Followed by the reverse pulse phase, a low voltage (0.35 V from reference to working electrode in the cell) is applied so that the loosely bounded Co atoms at the defected crystal locations are etched and removed back into the electrolyte. Also the concentration and the pH value of the electrolyte can relax during this phase, to help maintain a constant yielding through the whole deposition process. The electrochemical deposition was done in pH = 6 $CoSO_4$ electrolyte (pH adjusted by adding sodium tetraborate), and the time periods for the

pulse and reverse are 10 ms each. The PRECD process is illustrated in the Figure 3.6. This recipe was developed by Dr. Andrew Ursache and published in the reference.[8] For the 10 seconds of PRECD, it yields 50 nm height Co nanomagnets confined in the EBL patterned nanotemplates. After PRECD, the e-beam resist (PMMA) layer is kept to support the high aspect ratio Co nanomagnets.

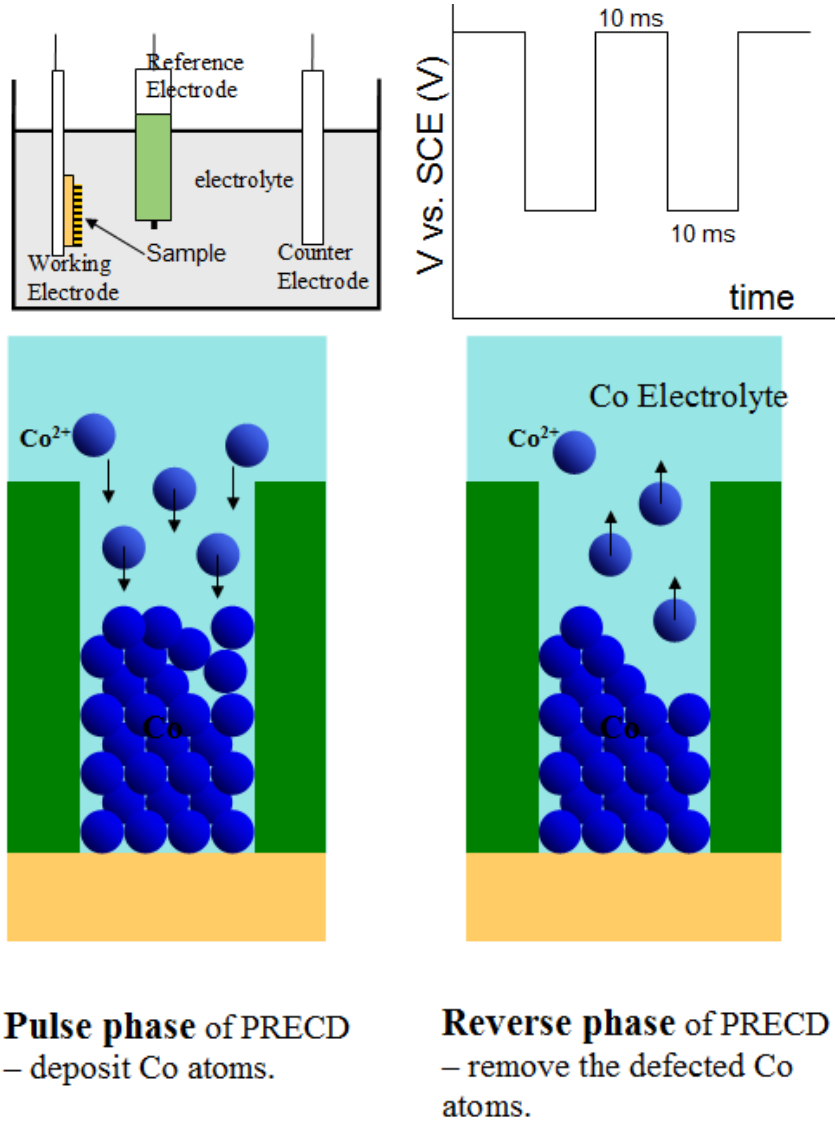

Figure 3.6 Schematic illustration of the PRECD process of fabricating Co perpendicular nanomagnets. *Top*: The three-electrode PRECD cell set up. *Bottom*: Illustration of the separate pulse and reverse phases of the PRECD process. (Reference 8)

3.2 Characterization of the devices using MFM

We measured the magnetic states of three-dot cluster of perpendicular Co nanomagnets by magnetic force microscopy (MFM). MFM is a derivative mode atomic force microscopy (AFM). The tip is coated with a magnetized material (e.g., CoCr or NiFe). The magnetic dipolar moment of the AFM tip couples to the stray magnetic field emanating from the sample surface, giving rise to the magnetic force between the tip and the sample. This force, typically in the 10's of pN's, is much smaller than the forces during intermittent tapping AFM used for topography imaging during the first trace of scans. To detect this weak magnetic interaction with MFM, the cantilever must be lifted up above the sample surface to eliminate the dominating short range Van der Waals force. During the second trace of scans with lifted up cantilevers, the servo keeps the cantilever on the same topography trace scanned from the first tapping AFM scan trace.[14-16] Also, cantilevers with low stiffness are used here: spring constant typically 0.01-0.1nN/ nm. The MFM cooperating with tapping AFM is shown in the schematic drawing in Figure 3.7 below.

In our experiments, the lift up distance was set to be below 50 nm. The interaction between the tip and the sample's stray magnetic field leads to changes in the amplitude and phase of the cantilever oscillations and also to a change of the resonance frequency of the cantilever. Since the tip oscillates with a non-zero amplitude, the distance between the tip and the sample changes during each oscillation cycle, and with it so does the strength of the stray magnetic field and the tip-sample

magnetic interaction: The gradient of the magnetic field above the sample surface leads to a gradient of the tip-sample force, which then alters the cantilever's motion.

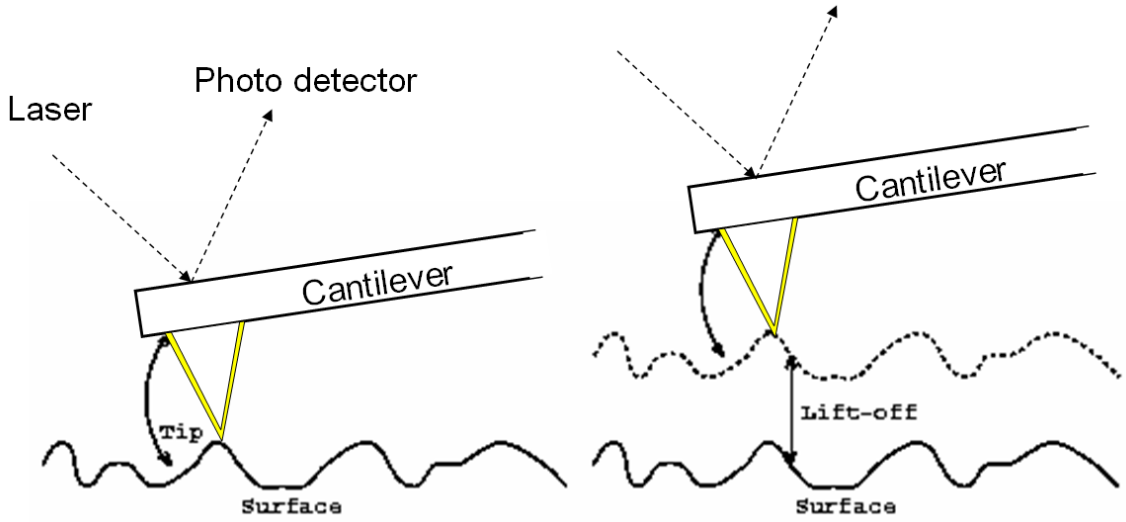

Figure 3.7 Schematic drawing of traces of AFM and MFM. *Left*: The first pass is a standard AFM trace that maps out the surface topography by gently tapping the tip along the surface. *Right*: A second pass then samples the magnetic stray field by scanning at constant height above the surface. The tip is coated with a magnetized material (e.g., CoCr or NiFe), so changes in the magnetic field affect the resonance characteristics of the cantilever, which are detected by the laser/photo-detector setup.

It is this force gradient that the MFM mode detects and maps into the image. At a given drive frequency, the phase and the amplitude of the cantilever oscillations change. These changes can be recorded pixel by pixel to generate an MFM image. When the phase signal is mapped in this way, an MFM phase image is created. This is the mode of MFM we used in our experiments for this project by keeping a constant cantilever frequency. Alternatively, the phase signal can be used in a feedback loop, which controls the frequency of the drive signal in such a way to maintain a constant

phase difference between the drive signal and the cantilever oscillations. In that case, one obtains a frequency modulation MFM image (FM-MFM).[19]

In general, the measurement performance of Magnetic Force Microscopy is a compromise between sensitivity, resolution and sample disturbance. High sensitivity to magnetic signal requires a strong magnetic moment of the tip. However, this high magnetic moment may disturb the domain structure of the sample itself and usually the lateral resolution drops with increasing magnetic moment of the tip. For improvement of the lateral resolution sharp high aspect ratio tips and thin magnetic coatings are required. Because of the low magnetic moment of such thin magnetic films the sensitivity is decreased. An optimum trade-off between lateral resolution and sensitivity is necessary. The magnetic domains of low coercivity samples are predominately "wiped out" by hard magnetically coated tips. This kind of sample can only be visualized by low coercivity probes which, on the other hand, may change their magnetization under the influence of a magnetic sample with higher coercivity. Therefore, in order to achieve optimum results, the MFM probe has to be chosen carefully and in accordance with the particular sample under investigation.

We label the remanent magnetization states of the cluster as +3, +1, -1 and -3, corresponding to the natural counting of the total net perpendicular moment in units of a single Co nanomagnet perpendicular moment. Shown in Figure 3.8, we achieved the four discrete perpendicular magnetic states of the Co three-nanomagnet cluster as we swept the applied field. The dimensions of cluster from the topography AFM image, shown in Figure 3.8 (a), are 30 nm in diameter and 50 nm in height for an individual

Co nanomagnet, with 100 nm separation between the neighboring nanomagnets. The MFM images in Figure 3.8 (c-f) show the perpendicular magnetoanisotropy of the Co nanomagets, and the distinct states of the cluster corresponding to the four magnetostatic states predicted previously. It needs to be emphasized that the MFM images in Figure 3.8 (c-f) are remanent magnetostatic states of the cluster, which are meant to be stable for the purpose of holding the data information written into the cluster after the external applied field is turned off. In our experiments the stability of the remanent states of the clusters was confirmed again by the series of MFM scans.[7]

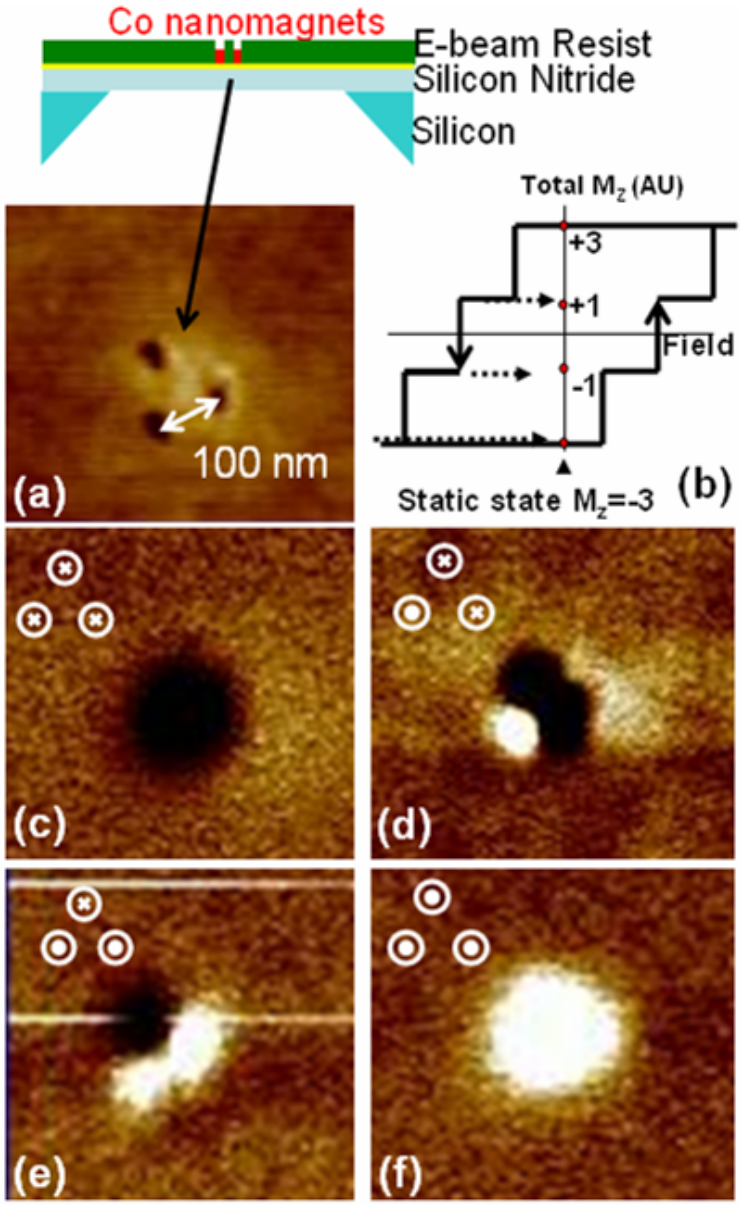

Figure 3.8 Magnetic switching process resulting in four stable remanent magnetic states with distinct total perpendicular magnetization. (a) AFM topography of the cluster of three Co nanomagets fabricated by PRECD. (b) Schematic magnetic switching curve of the 3-dot cluster showing the four distinct states. MFM images of the four magnetic static states in: (c) Remanent state with all nanomagnets pointing down, total M_z = -3. (d) One of the nanomagnets pointing up, total M_z = -1. (e) Two of the nanomagnets pointing up, total M_z = 1. (f) All nanomagnets pointing up, total M_z = 3. (Reference 7)

The magnetic switching experiments were performed qualitatively, using a magnet outside of the MFM platform. The sample consists of an array of three-dot Co nanomagnet clusters fabricated on the SiN/Si wafer. The external magnetic field was applied in discrete steps, precisely controlled by the superconducting coil in a Magnetic Property Measurement System (MPMS). The sample was loaded into the MPMS, where the field was ramped from zero to -2 T and sustained for 5 seconds. After that, the field was returned to zero, the sample was retrieved and MFM measurements were performed. The experimental protocol was repeated consequently at 0.2 T and 2 T applied fields. Repeating MFM experiments showed the clusters to have stable remanent states at room temperature and zero applied field, which is a valuable property for data storage application. For the ± 2 T field experiments, the magnetization of the clusters is completely switched to the all up/down states, as shown in Figure 3.8 (f), (c). The remanent state of the array of clusters for the 0.2 T experiment is a mixture of the intermediate states, shown in Figure 3.9.[7]

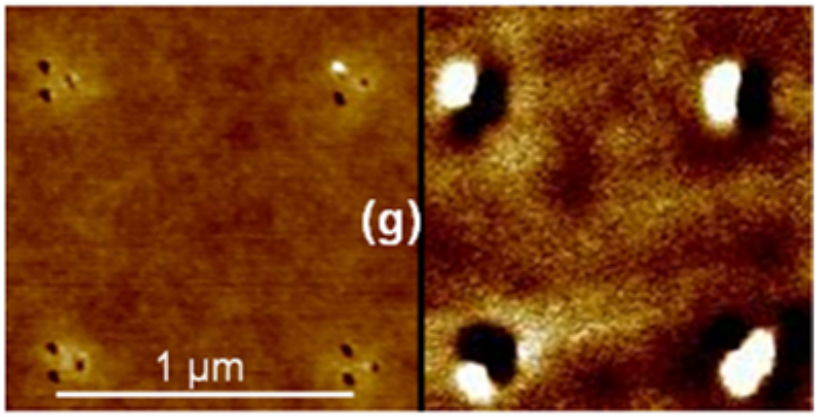

Figure 3.9 AFM (left) and MFM (right) images of the mixed remanent states of the clusters after applying 0.2 T field during the switching experiment. (Reference 7)

One reason for this mixture of the states is the inhomogeneity of the physical dimension of the nanomagnets fabricated by PRECD. This inhomogeneity can be caused by nucleation variation of the electrodeposition processes of the Co nanomagnets, conducting underlayer roughness and nonuniformity of the PMMA nanotemplates after EBL. Uniform electrochemical deposition is a topic of great research and engineering interests for many applications.

From the aspect of switching physics, the physical dimension of our Co nanomagnets is beyond the single domain scheme which enables coherent switching process, given the coherence diameter of Co to be 15 nm. The switching behavior of magnetic particles of similar sizes is called quasi single domain switching. The micromagnetic simulations show the magnetic moments orientations inside the Co magnetic body of 30 nm in diameter. The moments are almost perfectly aligned along the easy axis, except for small perturbation around the edges, shown in Figure 3.10. More research is yet to be done on the details of the switching processes of the quasi single domain nanomagnets as the Co nanoparticles we introduce in this thesis, in order to understand the phenomenon of mixed intermediate states we observed.

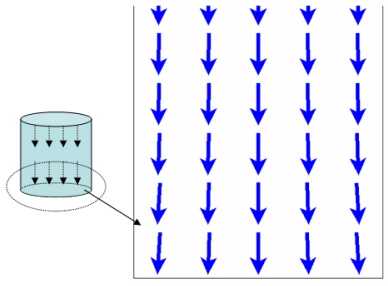

Figure 3.10 Micromagnetic simulations showing the quasi single domain particle behavior of the Co nanomagnet with 30 nm in diameter

It is also caused by stochastic thermally driven switching processes of the nanomagnets, which also depend on the applied field sweeping rate and history.[20] Co has $M_s = 1.42 \times 10^6$ $A \cdot m^{-1}$.[21] By approximating the nanomagnets as dipoles that only have the magnetization in the normal-to-substrate directions, one can estimate the interaction field from a Co nanomagnet to its neighbors.[22] For the Co three-dot clusters we report here, the net interaction field to one Co nanomagnet due to all its neighbors is no more than 100 Oe. As we described in the simulation and theoretic consideration sections, the switching steps from states to states are separated by the interaction fields. If the field is not strong enough, the overlapping of the switching field distribution curves can not be prevented and mixing of the intermediate states at one given applied field will happen. It should be emphasized that follow up experiments will be needed to prove the deterministic control of the magnetic states of the clusters by an applied field.

3.3 Summary

To conclude, in this work we develop prototype elements for multistate (beyond binary) perpendicular data storage using interacting single domain Co nanomagnet clusters. This experimental work confirms earlier theoretical work that predicted multiple discrete values of stable remanent magnetization for such clusters. The fabrication scheme is based on ultra-high resolution e-beam lithography (EBL) performed on a thin suspended silicon nitride membrane to reduce the secondary backscattered electrons from the substrate. A Co nanomagnet cluster array is deposited into the nanotemplate via pulse-reverse electrodeposition (PRECD) to create

nanomagnets with the favored uniaxial perpendicular anisotropy.[8, 9] MFM measurements show the perpendicular magnetization of individual Co nanomagnets and the combined multi-configuration behavior of a nanomagnet cluster. In concept, the discrete values of net remanent magnetization of the cluster, which represent distinct information states, can be "programmed" by a uniform applied field. We have shown the applicable physical properties of the interacting perpendicular nanomagnet clusters as novel multistate perpendicular storage device prototypes as a potential means to circumvent the eventual limitations of conventional data storage designs. We described the enabling EBL fabrication technique in great detail such that this method can be used to fabricate other new nanostructured devices. As we showed in Figure 3.4, we have the capability to fabricate smaller clusters by shrinking the center-to-center distance of the nanomagnets from 100 nm to 60 nm. This will greatly enhance the interaction field in the cluster and increase the separation between transitions. With refined control of applied field sweeping and state-of-art nanofabrication technologies, e.g. nanoimprinting and diblock copolymer self assembly, more work focused on quantitative analysis on the switching behavior of more closely packed clusters will be performed to help further advance the field of multistate data storage.

3.4 References

1. J. Cheng, C. A. Ross and A. Mayes, *Nature Materials* **3**, 823-8 (2004)

2. T. Thurn-Albrecht, J. Schotter, G.A. Kästle, N. Emley, T. Shibauchi, L. Krusin-Elbaum, K. Guarini, C. T. Black, M. T. Tuominen and T. P. Russell, *Science* **290**, 2126 (2000).

3. K. Naito, H. Hieda, M. Sakurai, Y. Kamata and K. Asakawa, *IEEE Trans. Mag*. **38**, 1949 (2002)

4. M. Rooks, N. Belic, E. Kratschmer, and R. Viswanathan, *J. Vac. Sci. Technol. B* **23**, 2769 (2005)

5. P.Rai-Choudhury, *Handbook of Microlithography, Micromachining and Microfabrication* (SPIE, 1997)

6. A. N. Broers, *J. Electrochem. Soc.* **128**, 166 (1981)

7. Q. Xiao, T. Yang, A. Ursache, and M. T. Tuominen, *J. Appl. Phys.***103**, 07c521 (2008)

8. A. Ursache, J. T. Goldbach, T. P. Russell, and M. T. Tuominen, *J. Appl. Phys.* **97**, 10J322 (2005)

9. A. Ursache, M. Bal, J. T. Goldbach, R. L. Sandstrom, C. T. Black, T. P. Russell and M. T. Tuominen, *Mater. Res. Soc. Symp. Proc.* **721**, E3.3 (2002)

10. H. Zeng, M. Z. R. Skomski, D. J. Sellmyer, Y. Liu, L. Menon and S. Bandyopadhyay, *J. Appl. Phys.* **87**, 4718 (2000)

11. M. Sun, G. Zangari, M. Shamsuzzoha and R. M. Metzger, *Appl. Phys. Lett.* **78**, 2964 (2001)

12. D. Dobrev, J. Vetter, N. Angert and R. Neumann, *Appl. Phys. A: Mater. Sci. Process.* **69**, 233 (1999)

13. D. Dobrev, J. Vetter, N. Angert, and R. Neumann, *Appl. Phys. A: Mater. Sci. Process.* **72**, 729 (2001)

14. D.A. Bonnell, *Scanning Probe Microscopy and Spectroscopy* (Wiley, 2000)

15. U. Kaiser, A. Schwarz and R. Wiesendanger, *Nature Letters* **446**, 522 (2007)

16. U. Hartmann, *Annu. Rev. Mater. Sci.* **29**, 53 (1999)

17. T. Suzuki *et al., J. of Magnetism and Magnetic Mat.* **286**, 306 (2005)

18. R. Behrisch and W. Eckstein, *Sputtering by Particle bombardment: Experiments and Computer Calculations from Threshold to Mev Energies*. (Springer, Berlin. 2007)

19. Digital Instruments, *Support Note* No. **229**, Rev. B

20. D. J. Sellmyer, M. Zheng and R. Skomski, *J. Phys. Condens. Matter* **13**, R433 (2001)

21. D. Jiles, *Introduction to Magnetism and Magnetic Materials,* (Chapman & Hall, 1998)

22. Q. Xiao, R. V. Krotkov, and M. T. Tuominen, *J. of Appl. Phys*., **99**, 08G305 (2006)

CHAPTER 4

NANOFABRICATION WITH THE AID OF DIBLOCK COPOLYMER SELF ASSEMBLY NANOTEMPLATES

4.1 Introduction

The majority of this part of work is done in collaboration with Professor Thomas Russell's group in UMass Amherst. Block copolymer self assembly has been investigated intensively for the application of nanopatterning templates. The unique advantages of this technology include, not limited to, nanoscale pattern engineering and self assembly of the block polymers which enables massive and parallel production. It has already been proved valuable in various applications e.g. solar cells, microelectronics, magnetic recording media, drug delivery and photonic crystals.[1-7]

Block copolymers are a fascinating class of polymeric materials belonging to the big family of soft materials. This class of polymers is made by the covalent bonding of two or more polymeric chains that give rise to a rich variety of microstructures in bulk and in solution. The length scale of these microstructures is comparable to the size of the block copolymers molecules (typically 3-50 nm).[8, 9] Therefore, the microstructures are highly coupled to the physical and chemical characteristics of molecules. The conventional and potential high technology applications of block copolymers are based on their ability to self assemble, in bulk or in selective solvents, into ordered nanostructures with dimensions comparable to chain dimensions. By changing the molecular weight, chemical structure, molecule architecture, and composition of block copolymers, one can engineer the size scale, the

type of ordering and the characteristics of these nanostructures.[10] In our work only the type of linear diblock (A-B) copolymer was involved, the nanostructures of the self assembly are illustrated in Figure 4.1. For other types e.g. triblock copolymer and non-linear block copolymers please refer to the references.[10]

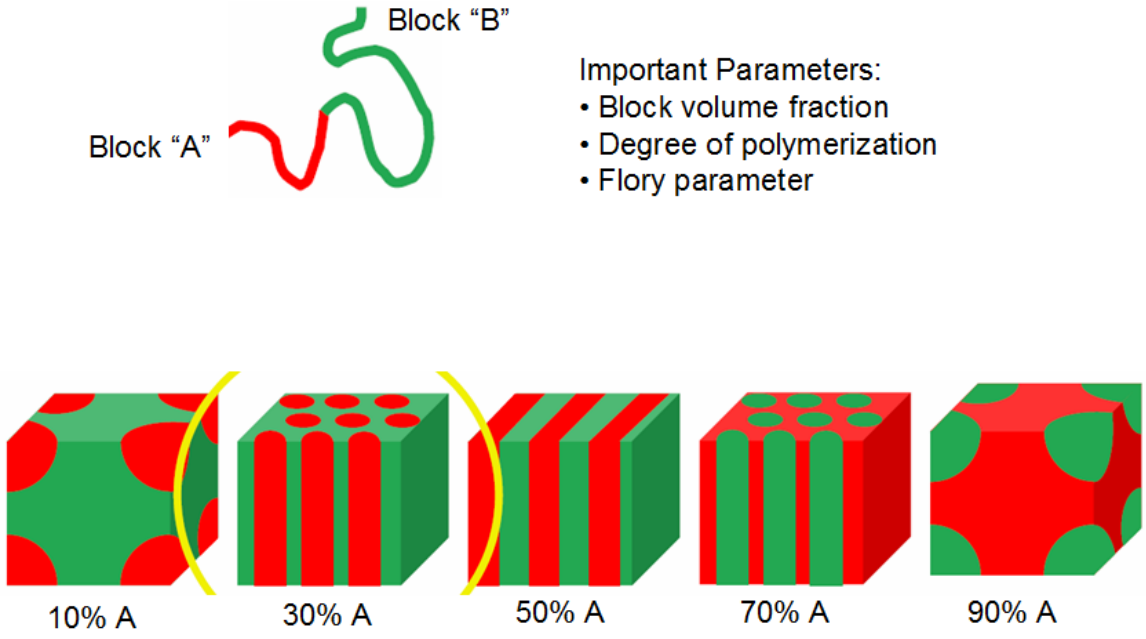

Figure 4.1 Schematic drawing of a linear diblock (A-B) copolymer chain. The nanostructures corresponding to different block volume fraction are shown on the bottom half of the plot. *Red*: micro domains of block A after the self assembly. *Green*: micro domains of block B after the self assembly. (Drawing from Reference 11)

Several critical parameters are in governing morphology of the nanostructures of the linear diblock copolymer self assembly:[10] degree of polymerization N, block volume fraction and Flory parameter χ. Degree of polymerization N is the total number of the repeating polymeric segments in the chain, and determines the length of the whole copolymer molecule. Block volume fraction is the volume ratio of the two

polymeric segments total volumes in the molecule. And the Flory parameter χ determines the interaction strength at the interface of the two different polymeric segments.

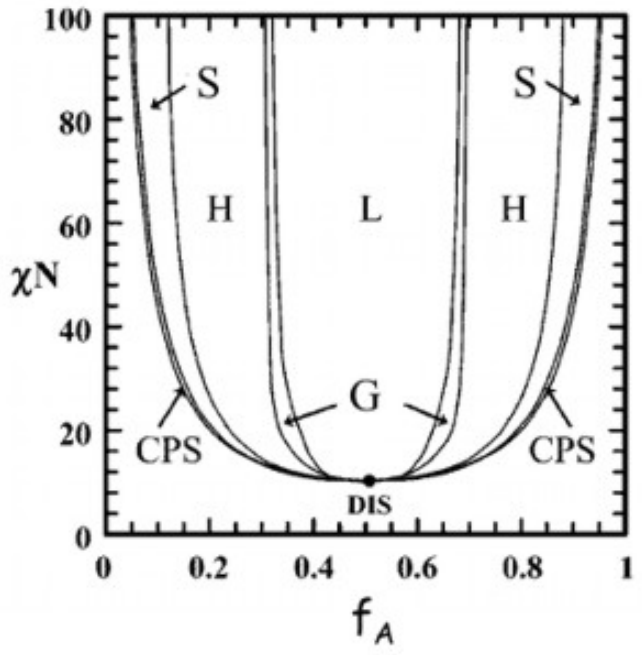

Figure 4.2 Diblock copolymer theoretic phase diagram, as the function of the block volume fraction and $N\chi$. Explanation of the letters built in the plot - **S**: spheres, **H**: hexagonal cylinders, **G**: gyroid, **L**:lamellae, **DIS**: disordered (homogeneous) state, **CPS**: close-packed spheres. (Figure from reference 12)

Figure 4.2 shows the theoretical simulation of the diblock copolymer self assembly phase diagram.[12] One of the dominating parameters is the product of degree of polymerization and Flory parameter $N\chi$.[10] The forming of the self assembly is not entropic favorable, because the copolymer chain undergoes the change from disordered (homogenous mixture of the A, B blocks) states to the well separated and ordered states. On the other hand, interfacing of A and B polymeric segments costs internal

energy of the system. By forming microdomains of separated A and B blocks, the system can minimize the A-B block interface area and thus lower the total internal energy. This energy term is solely controlled by the Flory parameter χ. Degree of polymerization N contributes to the size of the diblock copolymer molecule and thus governs the dimensions of the microdomains of the blocks after the microphase separation (self assembly). For larger N, the molecule is longer and has more degrees of freedom of motion. This means the polymeric chain of the diblock copolymer is softer to stand more bending and deforming which are necessary for the microphase separation. Degree of polymerization N plays directly with the competition between the entropic energy and interfacial interaction energy for the formation of the diblock copolymer self assembly - so that with larger N one can allow weaker A-B block interaction (smaller χ) to form the self assembly, and vice reverse for the smaller N and larger χ. This is the reason that the product of $N\chi$ is plotted as the dominating factor for the self assembly formation. Certain diblock copolymers with stronger χ are particularly interested for nanomanufacturing because they can enable the diblock copolymer self assembly with smaller degree of polymerization N, so that the self assembly nanostructures have smaller domain sizes. For example, this is intensively under investigation in the field of magnetic storage media as the industry is trying to shrink the critical dimension (CD) of the perpendicular bit media below 10 nm and increase the storage density to the new record. Poly(styrene)-*b*-Poly(ethylene oxide) (PS-*b*-PEO) [13] and Poly(styrene)-*b*-Polydimethylsiloxane (PS-*b*-PDMS) [14] are two of the well known diblock copolymers with high χ.

Block volume faction f_A determines the type of the nanostructures for the self assembly, assuming that the copolymer is incompressible.[10] It is worth noticing that same volume faction f_A does not necessarily indicate same unique self assembly nanostructures. For example, with block volume faction f_A=30% which means the total volume of the block A in the whole molecule chain is 30%, the microdomain of block A after the self assembly can be either standing up cylinders or laying down lamellas. In both cases the volume fraction of the block A domains is 30%. In the real applications, other critical conditions need to be considered, e.g. the difference of A, B block interfacial energy to the substrate.[15-21] As for thin films, preferential wetting of one block component with the substrate or difference in the surface energy of two components will lead to a parallel microdomain orientation to the substrate, while the balanced interfacial interactions at surface (the so-called neutral surface) favors a microdomain orientation normal to the film surface.

4.2 Poly(styrene)-*b*-Poly(methyl methacrylate) system

4.2.1 Introduction

The first diblock copolymer sample I used in the research for this project is Poly(styrene)-*b*-Poly(methyl methacrylate) (PS-*b*-PMMA). PS-*b*-PMMA has been intensively studied for the self assembly phenomena in various applications.[22-25] The distinctive chemical property contrast between PS and PMMA is one of the unique features of this material. As a commonly used electron beam lithography resist and UV photoresist, the polymeric PMMA chain can be degraded by UV exposure or electron

beam radiation into smaller segments.[26] PS on the other hand is a more robust material and will crosslink under the radiations. The crosslinked (hardened) PS can form the backbone matrix for further application as the nanostructured templates.

4.2.2 Permalloy nanowire array fabricated by thick PS-*b*-PMMA template

4.2.2.1 Permalloy nanowire array fabrication

My first attempt of using PS-*b*-PMMA to fabricate nanoscale media devices was on thick PS-*b*-PMMA template. In this case, external field was needed for the alignment of the cylindrical phase-separated microdomains along the perpendicular direction normal to the substrate.[26, 28, 29] In the thin film case, the film is thin enough that it is commensurate with only one or two layers of the micro domains after the self assembly to from along the 2-D substrate plane, so that there is no need to consider the ordering in the direction normal to the substrate (because there is only a monolayer of the microdomains). For the thicker films (~1 micron), the stacking and the orientation of the microdomains can be varied along the direction normal to the substrate. For a uniform self assembly orientation along this direction, external field is needed to align the microdomains, due to dielectric constant contrast between the two blocks. In our case we use an electrical field applied normal to the substrate, as shown in Figure 4.3.

The sample is made of 42k molecule weight PS-*b*-PMMA with 28% PMMA volume fraction, and dissolved in toluene with the concentration of 10% (weight). A piece of silicon wafer is coated with 5nm of Cr (sticking layer) and subsequently 50nm of Au by thermal evaporation, as the bottom electrode as we apply the external

electrical field. The solution is spun cast onto the Au coated surface of the silicon wafer. The rotation speed during the spin coating modulates the thickness of the resulted diblock copolymer film, and in order to get a 1 micron thick 42k PS-*b*-PMMA with 10% (weight) concentration in toluene I used 800 RPM rotation rate. A piece of Al coated Kapton sheet is kept in firm touch on the top, with the Kapton facing the copolymer film. The Al layer works as the top electrode as we introduce the electric field and the Kapton layer servers as the insulating layer.

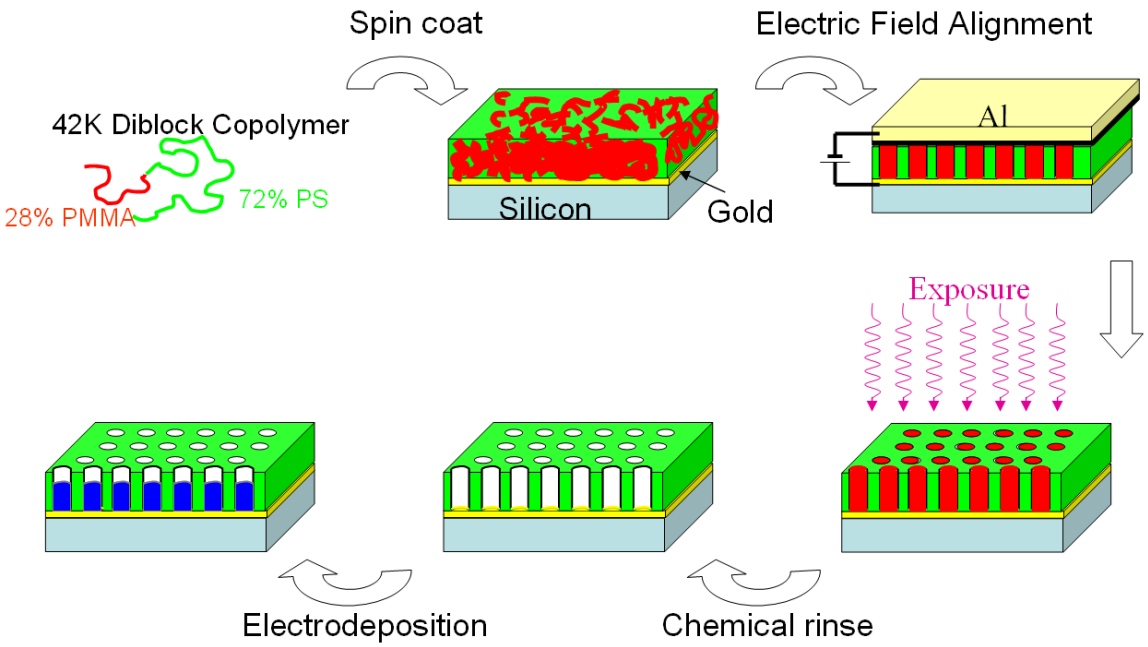

Figure 4.3 Schematic illustrations of processes to fabricate long metallic nanowire array by the aid of thick (1 micron) PS-*b*-PMMA film in our experiments. Process flow is indicated by the arrows, consequently: spin coating of the 42k molecule weight PS-*b*-PMMA with 28% PMMA volume fraction in toluene; electric field alignment applied during the annealing; UV or e-beam exposure to degrade the PMMA blocks after self assembly; rinse the sample in acetic acid to remove the degraded PMMA blocks; and finally use the nanoporous template as electrochemical deposition mask to fabricate the ordered magnetic nanowire array. (Reference 26)

According to the reference works,[26] one needs to apply above 30~40 volts per micron electric field in order to align the cylindrical PMMA microdomains built inside the PS matrix along electrical field which is applied normal to the substrate. The Kapton film is measured to be 25 microns thick, so we chose to apply 1000V voltage across the top (Al) and bottom (Au) electrodes. In some of our experiments we add an additional PDMS layer to the Kapton film to make it smoother for the surface in contact with the diblock copolymer film. With this additional thickness one needs to increase the applied voltage accordingly.

With sufficient vertical (normal to the substrate) electric field in presence, the diblock copolymer is annealed to the temperature of 178^{o}C. PS have the glass transition temperatures T_g around 100^{o}C and PMMA has T_g around 115^{o}C, but in order to achieve high mobility for the copolymer molecules one needs to heat the system well above the glass transition temperature,[27] so that the copolymer molecules can have the thermally activated high enough possibilities to explore various molecule arrangements and find the states with lowest local free energies. This mobility is essential for the self assembly forming process.

After 18 hours of annealing at 178^{o}C with the external electric field in presence, the sample was cooled down to room temperature slowly. The electric field was turned off subsequently. The diblock copolymer film was ordered and the microdomains were aligned along the electric field direction, as indicated in Figure 4.3. The next step is to remove the well ordered cylindrical PMMA microdomains to make the hexagonal nanoporous PS matrix for further pattern transferring. Two methods were used to degrade the PMMA blocks in the self assembly: UV exposure [26]

and electron beam exposure [30]. For the UV exposure method, total dosage was set to be 1 J/cm^2. Exposure intensity from a wide spectrum UV lamp was measured from 2.85 mJ/cm^2·s to 4.00 mJ/cm^2·s, any intensity in this range worked well. This method is simple and fast, but it is difficult to precisely control the exposed sample area for precise nanotemplate engineering. In the electron beam exposure method, one can expose any arbitrary area of the sample by pre-designed patterns as in the case of e-beam lithography.[30] Corresponding to different electron beam exposure doses, the self-assembled diblock copolymer film will have various properties. We can divide the dose roadmap approximately into three regions: low dose region (0 to 60 μC/cm^2) in which the dose is too low to induce complete PMMA block degradation, appropriate dose region (60 to 300 μC/cm^2) in which the PMMA blocks are degraded, high dose region (300 μC/cm^2 and above) in which the PMMA blocks are cross linked partially or completely. In my experiments the optimal dose was set to be 80 μC/cm^2. Too low doses (in the low dose region) or too high doses (in the high dose region) will cause the cases in which the PMMA blocks can not be removed from the self assembly film afterwards. The degraded PMMA blocks were submerged in pure acetic acid (AA) for more than four hours and dissolved, therefore leaving the intact PS matrix forming the nanoporous template. Based on the degree of polymerization of the diblock copolymer I used, the nanopores in the template have the mean diameter of 14 nm, and they are arranged hexagonally with center to center distance of 30 nm.[30, 31, 32,]

In my experiments, Permalloy (Fe20% Ni 80%) was electrochemically deposited into the PS nanotemplates to form a uniform Permalloy nanowire array. The recipe of the Permalloy electrolyte is: $NiSO_4 \cdot 6H_2O$ (16 gm/L), $NiCl_2 \cdot 6H_2O$ (40 gm/L),

$FeSO_4 \cdot 7H_2O$ (1 gm/L), $H_3BO_3 \cdot 7H_2O$ (25 gm/L), and 20% volume of methanol to adjust the surface tension of the electrolyte so that it can get into the 14 nm diameter nanoholes. The deposition was done in DC mode, with constant 1.4 V on the working electrode versus SCE reference electrode. The cross section of the final fabricated Permalloy nanowire array built inside the diblock copolymer template is shown in Figure 4.4 below. In the left of the figure, an overview of the structure can be observed: from the bottom to the top, there are silicon wafer, thin Cr and Au layer serving as electrode during the ECD, Permalloy nanowire array deposited and ordered inside the nanoporous diblock copolymer template, and the unfilled copolymer template. In the right side figure a zoom-in image of the nanowire array shows the fine dimensions of the Permalloy nanowires defined by the diblock copolymer template.

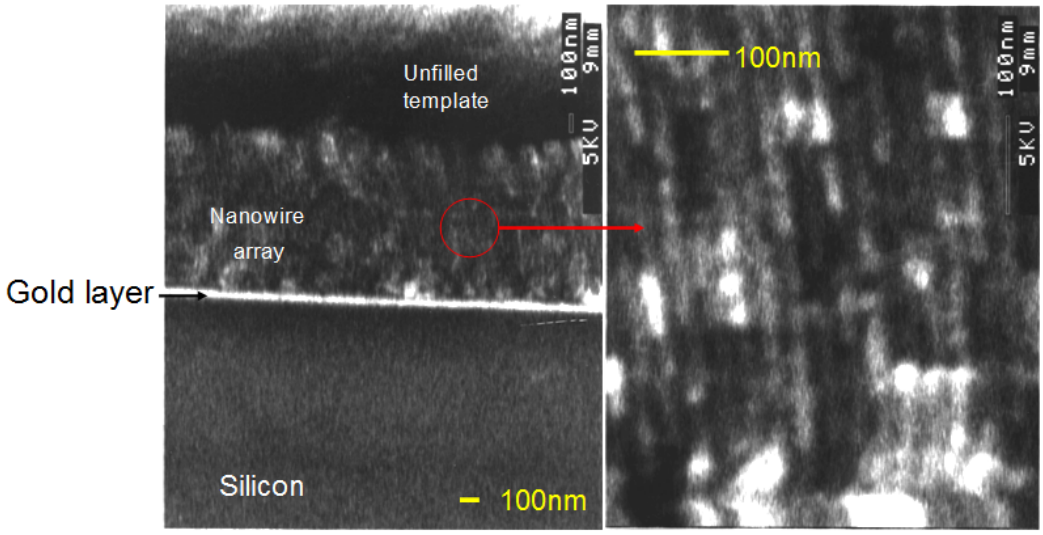

Figure 4.4 Field emission SEM images of my Permalloy nanowire array grown inside the thick diblock copolymer template.

4.2.2.2 Characterization

In bulk form, Permalloy is a soft ferromagnetic material and with negligible magneto crystalline anisotropy. In the nanowire form, the shape anisotropy dominates the magnetic behavior of the Permalloy samples, with the preferred magnetic easy axis along the nanowire orientation due to the extremely high aspect ratio of the nanowires. The length of the nanowires can be controlled by monitoring the total charge transferred during the electrochemical deposition process.[30] The purpose of this experiment was to compare with the Co nanowire array fabricated in earlier projects,[31, 32] for potential application in the data storage devices. The Co magnetic nanowire arrays are harder magnetically, with the uniaxial anisotropy enhanced by the crystalline anisotropy oriented along the nanowire direction. A brief comparison of these two systems is shown in Figure 4.5 below, with 800 nm Permalloy nanowire array and 500 nm Co nanowire array fabricated from the same 42k PS-*b*-PMMA with 28% PMMA volume fraction template.

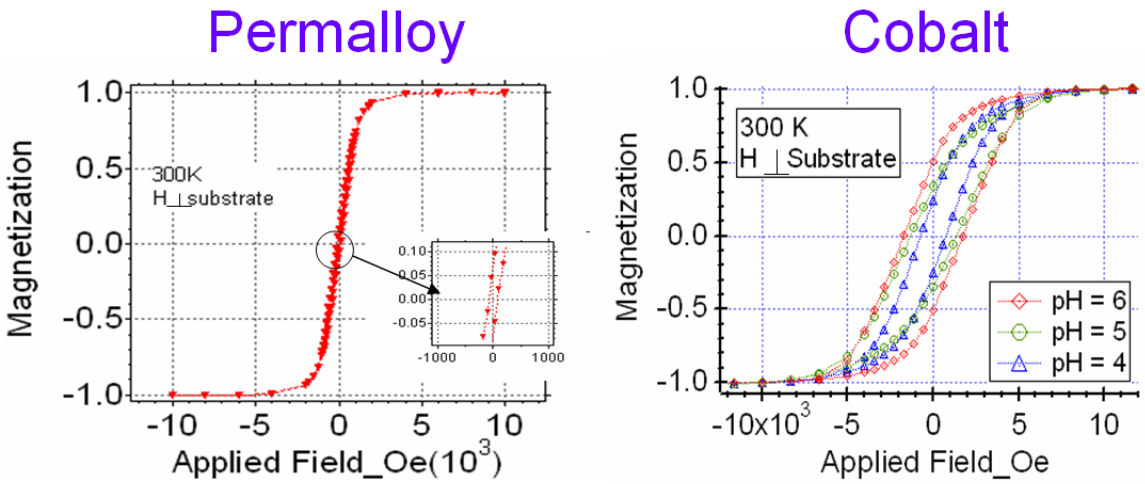

Figure 4.5 Comparison of 800 nm Permalloy nanowire array and 500 nm Co nanowire array [32] fabricated with same diblock copolymer template. (Right side figure from reference 32)

In Figure 4.5, both of the hysterisis curves were measured by SQUID (Superconducting Quantum Interference Device) at 300 K. The external magnetic field was applied perpendicular to the substrate (parallel to the nanowires), which is the easy axis direction of the magnetic nanowires. Due to the significant difference of the magnetic hardness of these two samples, Permalloy nanowire array showed extremely low coercivity (88 Oe) compared to the Co sample. As explained previously, this is because that the Permalloy nanowires only have shape anisotropy, but the Co samples also have enhanced uniaxial magneto crystalline anisotropy aligned along with the shape anisotropy.

Based on the dimensions of the fabricated nanowires inherited from the diclock copolymer self assembly nanotemplates, the magnetic properties are unique in various aspects. The first one is the switching behavior of a single Permalloy nanowire. In nanoscale particles wires the magnetization reversal is uniform (coherent) in the cross section of objects, but in macroscopic ellipsoids it is incoherent. In perfect wires, the transition from coherent to incoherent nucleation occurs at an anisotropy independent coherence diameter [33] $d_{coh} = 7.31\ L_{ex}$, where $L_{ex} = \sqrt{\frac{A}{4\pi M_S^2}}$ is the exchange length (A denotes the exchange stiffness). In our system, the diameter of the nanowire (14 nm) is smaller than the coherence diameter of Permalloy (89 nm), so the magnetization rotation of the Permalloy nanowire can be considered as coherent on the cross section planes of the wires. On the other hand, along the direction throughout the nanowire the magnetization rotation is not coherent for the thin and long wires with the geometry of our samples here. The magnetization rotation involves localized reversal, which starts in a very small region of the nanowire with inhomogeneous magnetization states and is

therefore unfavourable from the point of view of internal magnetic exchange. However, magnetization processes localized in the vicinity of imperfections may be favorable due to locally reduced anisotropy and magnetostatic energies. This localized region is called activation region (of magnetic reversal), and the process of forming the activation region at the beginning of the magnetic reversal is called nucleation. The activation region creates certain magnetic domain walls during the nucleation. The domain walls will propagate throughout the magnetic nanowire to completely switching the magnetization of the nanowire, under the influence of the external applied magnetic field.[53, 54] This process is illustrated in Figure 4.6 below.

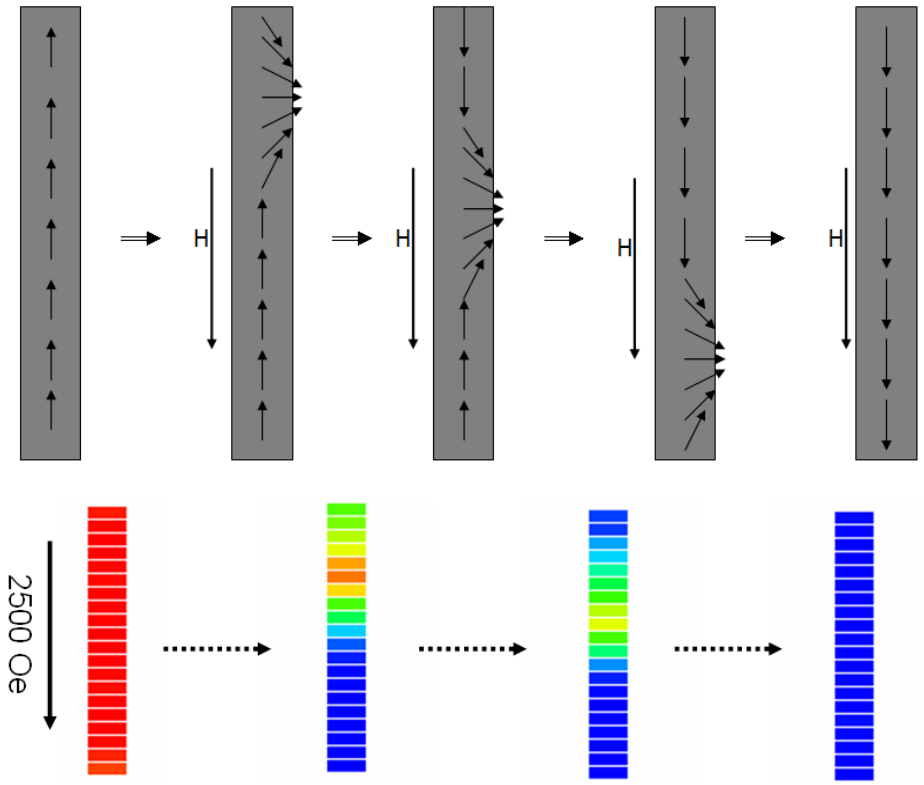

Figure 4.6 Nucleation and propagation of the activation region during an incoherent magnetic reversal of thin, long magnetic nanowire. On the top: schematic drawing of the incoherent reversal process. On the bottom: micro magnetic simulation of switching event of a Permalloy nanowire.

In the bottom part of Figure 4.6, micro magnetic simulation of a random switching event of a Permalloy nanowire is shown. The nanowire has the dimension of 14 nm in diameter and 100 nm in length. The temperature is set at 300 K. The nanowire is meshed into nano scale grids with the dimension much smaller than the exchange length of Permalloy (12.2 nm),[33] so that one can assume the magnetization of each individual mesh is uniform and stays uniform during the magnetic reversal. The initial magnetic state of the nanowire is set to perfect alignment along the up direction, indicated by the red meshes. A constant external field of 2500 Oe is applied along the opposite direction (down). Afterwards, the nucleation and propagation of the activation region are clearly demonstrated by the intermediate simulation states. And the final state of the nanowire is that all of the meshes have uniform magnetization pointing down, indicated by the color of blue. The colors between red and blue indicate the magnetization pointing to off axial directions.

Thermal variation of the magnetic properties is particularly interested in the data storage applications, due to the significance of obtaining thermal stability. The temperature dependence of the coercivity of 800 nm Permalloy nanowire array is measured and plotted in Figure 4.7. In this figure the external field is applied along the easy axis of the magnetic nanowires and perpendicular to the substrate. From the measurements, the coercivity (in Oe) of the 800 nm Permalloy nanowire array is determined to be 713, 592, 360, 227, 88, at temperatures of 5 K, 20 K, 77K, 150K and 300 K respectively. It is worth noticing that the hysterisis loop at 5 K is not symmetric by the original y axis (applied field = 0). This shift is caused by the presence of anti-ferromagnetic material under this temperature. Unlike the cases under higher

temperatures in which the coercivity is the same on both sides of the hysterisis loops, the coercivity under 5 K is calculated by averaging the two coercivity readings on both sides.

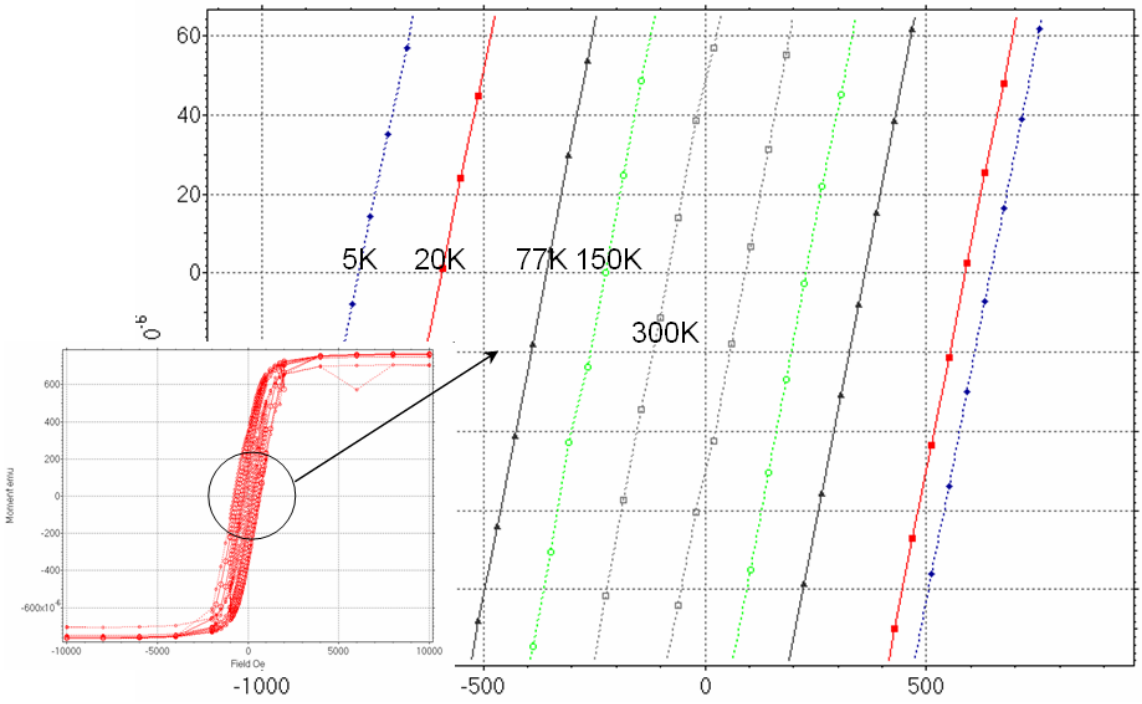

Figure 4.7 Temperature dependence of the coercivity of 800 nm Permalloy nanowire array. The zoom-in curves show the detailed hysterisis loops near the coercivity points with temperature labels.

In a Stoner-Wohlfarth ellipsoid particle, the magnetic reversal is coherent. The switching energy barrier can be written as $E_B(H) = K_\mu V(1-\frac{H}{H_A})^2$, [33] in which H is the applied field (along the opposite orientation of the initial magnetization), K_μ is the anisotropy constant, V is the volume of the particle, and $H_A = \frac{2K_\mu}{M_S}$ is defined as anisotropy field.[33] It is also a good approximation to include the thermal excitation in

the factors that are needed to overcome the energy barrier during the magnetic switching process by the formula $E_B(H) = k_B T \ln(f_0 \tau)$,[55] in which f_0 is the attempt frequency and τ is the relaxation time constant. Therefore, the coercivity H_C can be written as $H_C = H_A - \left[\frac{k_B}{K_\mu V}\ln(f_0\tau)\right]^{\frac{1}{2}} H_A T^{\frac{1}{2}} = A - B \cdot T^{\frac{1}{2}}$. This indicates that the temperature dependence of the coercivity of a SW ellipsoid magnetic particle is proportional to the square root of temperatures. The measured coercivity versus temperature curve of the 800 nm Permalloy nanowire array is plotted in Figure 4.8, and compared to a fitting curve using the $A - B \cdot T^{\frac{1}{2}}$ relation derived above for the SW particles. The measured curve matches with the fitting well.

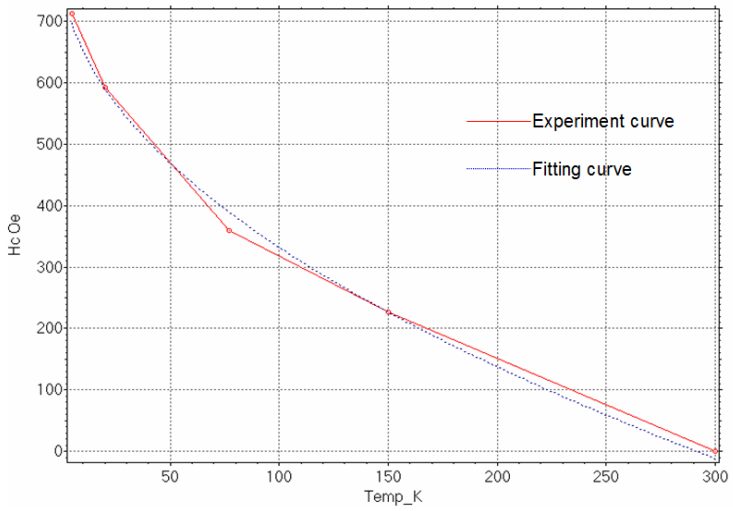

Figure 4.8 Measured temperature dependence of coercivity of the 800 nm Permalloy nanowire array with external field applied along the nanowires. And comparison to the fitting curve with the fitting formula $A - B \cdot T^{\frac{1}{2}}$.

4.2.3 Thin self-assembled PS-*b*-PMMA template

Using controlled interfacial interactions, a thin layer of PS-*b*-PMMA can form a well-ordered self assembly in the substrate plane without extra field alignment.[15,35] This system had been studied intensively for various nanofabrication applications, and I have found it is more relevant to my goal of fabricating the quasi two dimensional array of interacting single domain nanomagnets, compared to the thick diblock copolymer templates which are favor the formation of long nanowire array. In my experiments, I am interested in the cylindrical microphase separation of the self assembly because of the nanoporous template inherited from the self assembly. For this kind of block copolymer PS-*b*-PMMA with around 30% PMMA volume fraction, thin film morphology depends on the many factors including the film thickness and surface interaction.

If the surface has a stronger preference to one component of the copolymer, the copolymer will form self assembled cylinders in the substrate plane,[56] given that the thickness of the copolymer film is about the same as an intrinsic polymer length scale [34] $l \equiv \sqrt{3}d/2$ (d is the center to center separation of the adjacent PMMA cylindrical domains).[34] In this case, if the thickness of the polymer template is lower than l there is no ordered self-assembly; and if the thickness is much higher than l there are multi layers of mixture of in-plane and perpendicular self-assembly patterns. If one treats the substrate first to be a neutral surface to both PS and PMMA, i.e. treating the substrate with random copolymer brush,[35] the copolymer template will form perpendicular PMMA cylindrical domains in a PS matrix, given the film is of appropriate thickness.

In my experiments it is preferable to have perpendicular PMMA cylindrical micro domains after the self assembly on top of a piece of silicon substrate. Native or thermally grown SiO_2 will be found on the surfaces of silicon wafers. Because of the affinity of PS blocks to the SiO_2 surface, it is necessary to process the silicon substrate surface with the neutralization steps prior to spin coating of the copolymer. It had been reported that one can dissolve the native SiO_2 layer of the wafer by dipping it into diluted HF solution (1%), and hence terminate the surface with hydroxyl bonding.[57,58] The modified surface acts "neutrally" to both blocks of the PS-*b*-PMMA copolymer film and thus supports the formation of perpendicular PMMA cylindrical micro domains after the self assembly. In our experiments we employed another method by anchoring a monolayer of neutral block copolymer prior to applying the PS-*b*-PMMA template. This neutral layer of copolymer consists of the copolymer PS-*r*-PMMA with alternating segments of PS and PMMA blocks of random segment lengths. The random distribution of the PS and PMMA blocks on the neutral surface after the anchoring will show equal affinity to both blocks of the PS-*b*-PMMA copolymer layer spun cast on top of it. The processes are demonstrated in the following figure 33 for example, as we used in our experiments.

First of all, as shown in Figure 4.9 (a), random copolymer solution PS-*r*-PMMA (58/42) 1% in toluene was spin coated onto the substrate (silicon, glass etc.).[35] The random copolymer has average molecule weight of 10K Daltons, and is functionalized with hydroxyl groups. The sample was then annealed in vacuum at 175 ^{o}C for 3 days, allowing the random copolymer molecules to be anchored to the substrate surface via the hydroxyl groups.

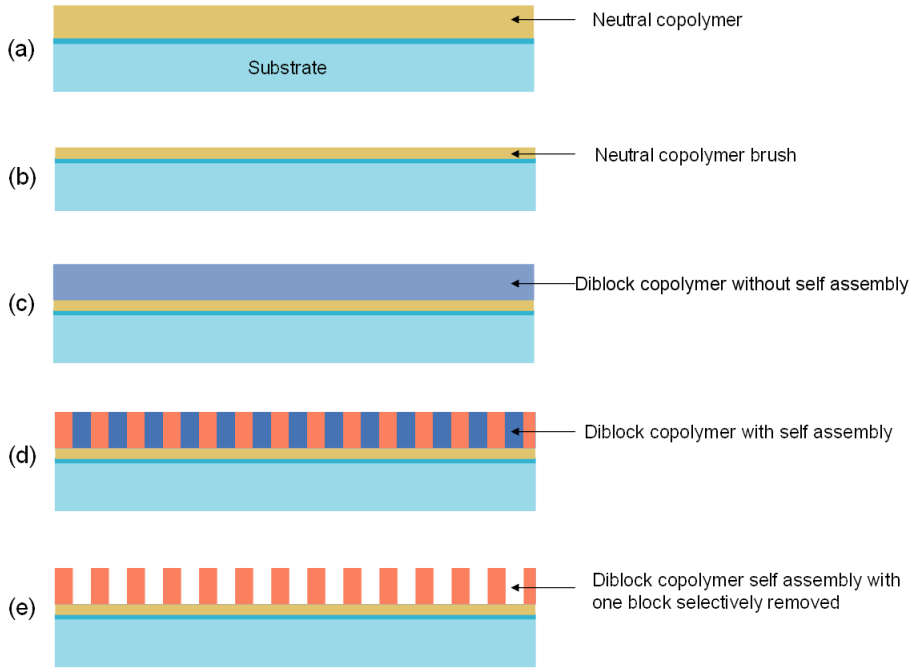

Figure 4.9 Demonstration of process flow for applying diblock copolymer self assembly on a neutralized substrate surface by anchoring a monolayer of random copolymer brush. (Concept from reference 15, 35)

The sample was rinsed by toluene afterwards, in order to remove the excess of the random copolymer molecules that are not attached to the substrate surface. This results in the monolayer of the random copolymer brush with the thickness of 2~3 nm, as shown in Figure 4.9 (b). The sample surface at this point shows unbiased affinity to both PS and PMMA blocks.[35] A thin layer of PS-*b*-PMMA with 70:30 volume fraction was spin coated onto the neutral surface, as shown in Figure 4.9 (c). The self assembly was then introduced by annealing the sample at 178 ^{o}C for 15 hours, and the PMMA blocks formed perpendicular cylindrical microdomains built inside the nanoporous PS matrix, shown in Figure 4.9 (d). In Figure 4.9 (e), the self assembled film was

developed in pure acetic acid for 30 minutes to selectively dissolve the PMMA blocks, and thus one can fabricate an ordered nanoporous PS template for further applications. Some real examples are shown in Figure 4.10 for demonstration.

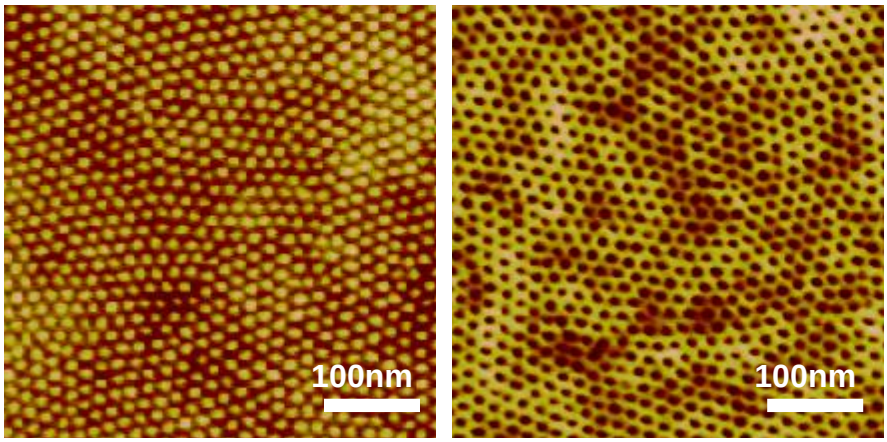

Figure 4.10 *Left*: AFM height image of ordered PS-*b*-PMMA(72:28) self assembly. The hexagonal array of bright dots are cylindrical PMMA blocks. *Right*: AFM height image of the nanoporous PS matrix after the PMMA blocks were removed by Acetic acid development.

Popular and powerful system as it is, the PS-*b*-PMMA self assembly requires extra certain steps to neutralize the substrate surface, and also needs time consuming thermal annealing processes. These complexities may limit the applications and increase the fabrication costs.

4.3 Poly(styrene)-*b*-Poly(4-vinylpyridine) systems

4.3.1 Introduction

In addition to the PS-*b*-PMMA self assembly templates, poly(styrene)-*b*-poly(4-vinylpyridine) (PS-*b*-P4VP) is the other block copolymer I used in the experiments. The solubility difference of the two blocks in selected solvents gives rise

to controllable self assembly and pattern reconstruction. This phenomenon had been discussed with great details in the references.[37, 38] With comparison to the thermally assisted self assembly of the PS-*b*-PMMA systems, the self assembly of PS-*b*-P4VP can be guided by the presence of particular selective solvents during the microphase reconstructions of the solvent annealing process. This process had been proved to be fast, easy to control, and high yield as a fabrication approach for the nanoscale templates. A schematic illustration [36] is shown in the next Figure 4.11.

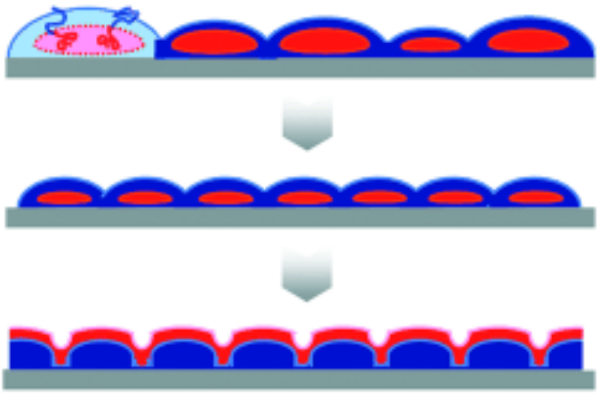

Figure 4.11 Solvent annealing process of PS-*b*-P4VP nanotemplate. The blue blocks are PS and the red blocks are P4VP. The process flow is indicated by the arrows from top to bottom. *Top drawing*: The rough micelle template on substrate after the PS-*b*-P4VP solution in toluene is spin coated. *Middle drawing*: Ordered micelle array of the PS-*b*-P4VP self assembly after the solvent annealing process. *Bottom drawing*: Inversed nanostructures after the surface reconstruction by development in ethanol. (Drawing from reference 36)

As dissolved in toluene, diblock copolymers such as PS-*b*-P4VP, aggregate into micelles. This is because toluene preferentially solvates PS, so that the PS blocks form a corona around the less soluble P4VP blocks to reduce energetically unfavorable interactions with the solvent.[36] The diameter and separation distance of the micelles can be tuned by the molecular weight of the block copolymers, the interactions

between the polymer blocks and the blocks with the solvent.[59] A micellar solution of PS-*b*-P4VP in toluene was spin coated onto silicon substrate. As spin coated, the PS-*b*-P4VP micelles have a broad size distribution, resulting in a short-range hexagonal order as shown in top drawing of Figure 4.11. When the micelle films were exposed to tetrahydrofuran (THF) vapor at room temperature, a significantly enhanced lateral order was obtained, as shown in the middle drawing of Figure 4.11. The resulted nanostructures are the same micelle array with the PS corona shielding the P4VP cores of better lateral ordering, compared to the as-spun roughly ordered PS-*b*-P4VP micelle array. This is because THF, similar to toluene, is a preferred solvent to PS as well. This procedure is normally referred as solvent annealing.[60-63] Next, the solvent annealed well ordered PS-*b*-P4VP micelle arrays are immersed in ethanol, which is a good solvent for P4VP and a no-solvent for PS. Because of the strong affinity between the P4VP blocks and ethanol, the P4VP blocks are preferentially attracted to the surface of the micelles, and the non-solvable PS blocks become the cores of the micelles. This surface reconstruction of the film, resulting in a highly oriented array of nanoscopic pores without changing the lateral ordering of the circular domains. Upon drying, a reconstruction of the film is observed where pores are opened in the positions of the original P4VP cores as the P4VP blocks within the pores are transferred to the surfaces. The self-assembly of block copolymers to nanoscale arrays, as a perfect example of bottom-up fabrication approach, makes them ideal candidates as templates and scaffolds for the fabrication of desired nanostructured materials with potential applications in optical, optoelectronic, and magnetic devices.

4.3.2 Direct e-beam patterning of featureless PS-*b*-P4VP thin films

This part of work of mine was inspired by the work done [39] by my colleagues Dr. Soojin Park and Dr. Ozgur Yavuzcetin. Their work involved e-beam patterning on the perfected ordered PS-*b*-P4VP self assembly, in order to combine the top-down fabrication approaches (e.g. lithographic patterning) with the bottom-up fabrication approaches (e.g. self assembly).

An important feature in the fabrication of functional nanostructures is the precise control of locations of nanometer-sized objects. We proposed to take advantage of the traditional lithographic patterning which is able to generate precisely designed nanostructures, to guide the nanostructures formed by the block copolymer self assembly. It is of great interests to investigate these guided self assembly behavior in many applications. For example, in next-generation perpendicular magnetic bit-media, it demands the bit densities up to 10^{12} bit/in^2 which is of the same infrastructure enabled by the copolymer self assembly systems, with perfect control of the nanobits shape and ordering distribution. In other words, it is desirable to have precise arrangement of the orientation and the lateral ordering as we have in the top-down approaches, and keep the signatures of the fine nanostructures introduced by the self assembly methods. For these purposes, top-down approaches, like photolithography, electron beam (e-beam) lithography, contact molding, zone-plate array lithography, and x-ray, are used to pattern a surface and are coupled with a bottom-up approach, like self-assembly, to control the lateral ordering and spatial location of nanoscopic elements. Though, it has been proved by these references that generating any arbitrary

irregular nanostructures inherited from the copolymer self assembly systems is extremely challenging in the large scale.

Dr. Soojin Park and Dr. Ozgur Yavuzcetin worked on a convergence of top-down and bottom-up approaches using PS-*b*-P4VP diblock copolymers with a high degree of lateral ordering as a model system.[39] Solvent annealing of PS-*b*-P4VP films in organic solvent exhibits the lateral ordering of block copolymer microdomains. Next, e-beam lithography was employed to prepare periodic and irregular patterns, keeping the high degree of lateral ordering in templates. Highly oriented PS-b-P4VP was cross-linked in e-beam exposed regimes, while unexposed ones were transformed into nanoporous structures after immersion in the preferential solvent of one of the blocks. A brief introduction of their work is shown in Figure 4.12.

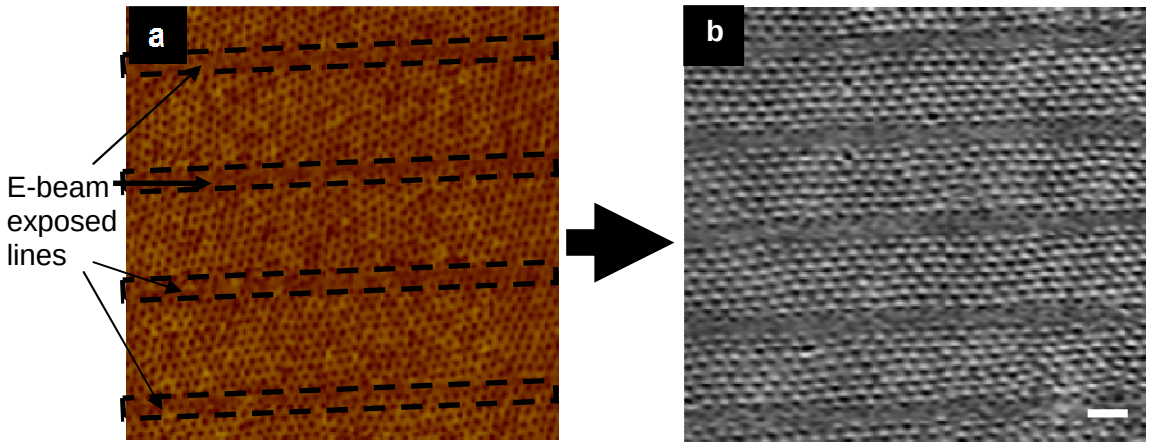

Figure 4.12 EBL patterning on ordered PS-*b*-P4VP templates. (a) EBL patterned nanoporous ordered PS-*b*-P4VP template after solvent annealing and surface reconstruction. (b) The pattern transferred to 14 nm height Ni nanodot array by evaporation and liftoff. Scale bar = 100 nm. (Reference 39)

They have demonstrated a method that can be used to generate periodic and irregular nanoscale patterns using solvent annealing, e-beam writing, and surface

reconstruction process. This method does not need to use topographic or chemically patterned substrates to create guided ordered arrays of microdomains of block copolymers, and can be applied to a variety of metal dotted arrays. Inspired by this work, I first tried to use the same method to define the ultra fine cluster patterns on ordered PS-b-P4VP templates. The resolution of the EBL patterning was proved to be sufficient for the designed isolated clusters of nanoscale elements in the self assembly with expected numbers and geometry. The results are shown in Figure 4.13 below.

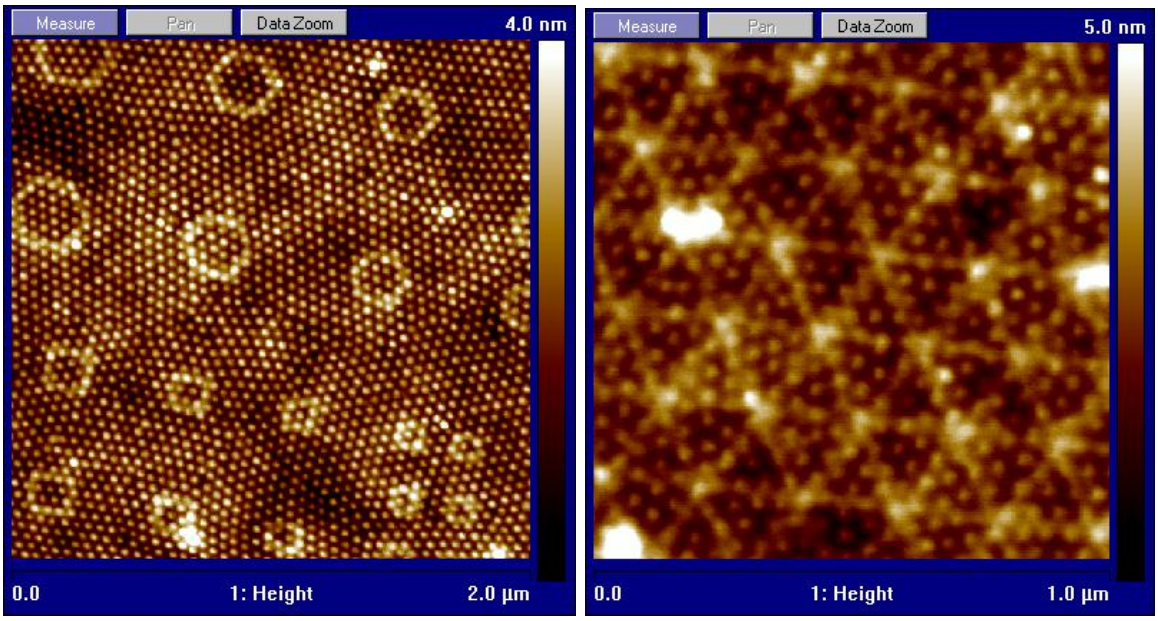

Figure 4.13 Direct EBL patterning on ordered PS-b-P4VP templates to generate ultra fine clusters of designed geometries. *Left*: Separated polygonal patterns with various shapes written by this method. *Right*: Triangular grids defining a three-dot cluster array written by this method.

In these experiments, I used the JSM-6400 SEM equipped with NPGS EBL module. The electron acceleration voltage was set to 20kV, and the line dosage of the EBL patterning was 6 nC/cm. The results turned out to be a rather random matching/mismatching of the EBL patterning and the lateral ordering of the self

assembly itself, as shown in Figure 4.13. This is obvious, because I do not have any information on the self assembly lateral ordering during the EBL patterning process. In order to overcome the problem arisen from the unknown self assembly lateral ordering during EBL, I invented a new approach similar to the old one: EBL patterning on featureless PS-b-P4VP film instead of on the ordered PS-b-P4VP template after the solvent annealing and surface reconstruction. Because there is no ordering inherited from the self assembly system when the EBL direct patterning is done, there is no matching/mismatching between the EBL pattering and the self assembly lateral ordering. The e-beam exposed patterns serve as the guiding features during the sequential solvent annealing and surface reconstruction processes due to the contrast of the exposed area and the non-exposed copolymer film.

The first step was to spin coat a featureless PS-b-P4VP thin film. The PS-*b*-P4VP used in this study was purchased from Polymer Source (number-average molecular weight Mn^{PS} = 41.5 kg/mol, Mn^{P4VP} = 17.5 kg/mol, molecular weight distribution Mw/Mn = 1.07). Unlike the previously reported experiments in which the PS-b-P4VP solutions were dissolved in toluene, we used dimethylformamide (DMF) as the solvent. PS and P4VP have significant solubility difference in toluene (solvent for PS but non-solvent for P4VP), so that the PS-b-P4VP copolymer mixed in toluene will form micelles in solution and un-evenly distribution of the micelles as spin coated to a substrate. The random distributions of the micelles shape, size and lateral ordering are not desired for the controlling purpose of direct EBL patterning. Instead, we chose DMF as the solvent. DMF can dissolve both PS and P4VP blocks so that the solution is transparent after the complete dissolving. The copolymer film is evenly distributed on

the substrate after spin coating without forming the micelles of PS shelled P4VP cores. Extra care must be taken during the spin coating process, though. Due to the fact that DMF has a strong affinity to the water vapor in the air, the spin coating procedure must be taken in a dehydrated enclosure otherwise the absorbed water vapor will cause wetting/de-wetting of the spin coated copolymer film. In our experiments the concentration of the solution is 0.5% by weight, and the whole process was done inside a sealed box with the ventilation hole on the top. The box was purged by argon. Argon was used because it is heavier than the air so that the flushing of Ar can force the remaining air to be purged through the ventilation hole on the top. This purging process took 30 minutes to make sure there was minimum amount of water vapor left inside the spin coater box, before the actual spin coating was done. The contrast of the thin films as spin coated with these two solvents (toluene and DMF) and different ambient environment conditions is shown in Figure 4.14 below. It proved that this spin coating process protected by argon purging supports the formation of a uniform smooth featureless PS-*b*-P4VP thin film, as I anticipated for further experiments.

Another significant difference between the PS-*b*-P4VP systems dissolved in toluene and DMF, is the different thin film profile dependence on the spin coating speeds. For the micelle solution of PS-*b*-P4VP prepared in toluene, the spin coating speed did not show significant influence on the thin film surface profile as spin coated. Spin coating this kind of the micelle solutions can be considered as distributing and arranging of the micelles on the substrate surface. In our experiments, we have tried a series of spin coating speeds from 1000 RPM to 3500 RPM with the PS-*b*-P4VP

solution in toluene, and all of the films as spin coated showed similar surface profile of micelle array, as shown in the right side figure of Figure 4.14.

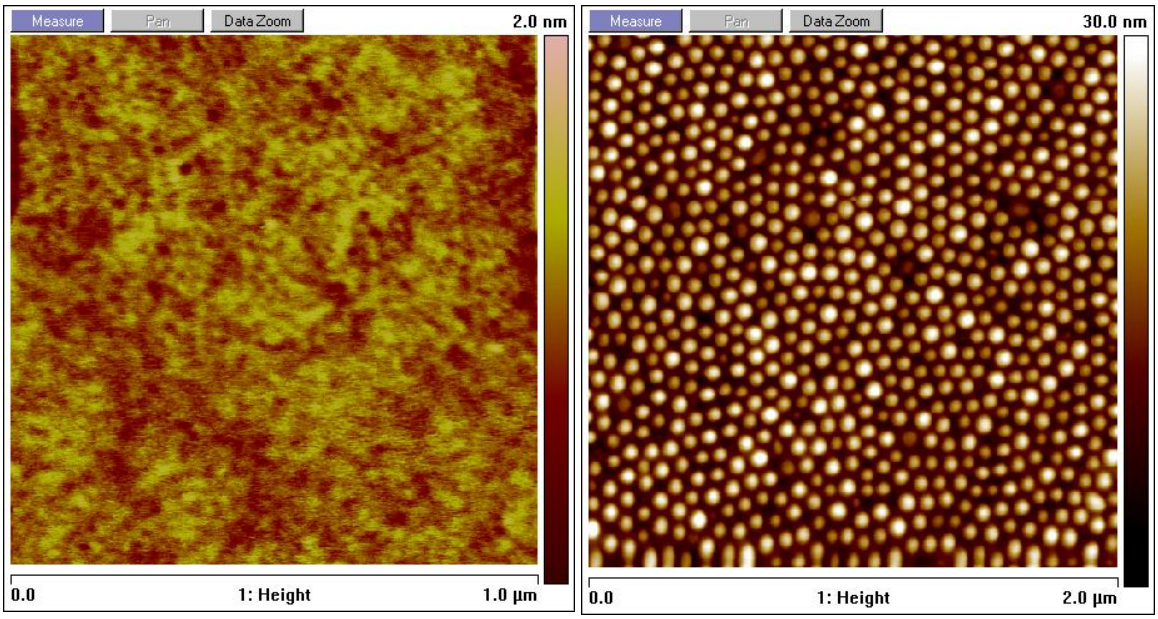

Figure 4.14 AFM height images of PS-*b*-P4VP thin films as spin coated, with different solvents and ambient conditions. *Left*: 0.5% weight concentration PS-b-P4VP dissolved in DMF, spin coated in Ar purged sealed enclosure. *Right*: 0.5% weight concentration PS-b-P4VP dissolved in toluene, spin coated in open air.

For the well dissolved solution of PS-*b*-P4VP in DMF, the resulted thin film thickness as spin coated is dominated by the spin coating speed. As we described in previous sections, the diblock copolymer thin film self assembly nanostructures are very sensitive to the thickness of the film. In this case, if the thickness of the PS-*b*-P4VP film is lower than a certain threshold value, there will be no self assembly after the solvent annealing. A series study of the dependence of the formation of lateral ordered PS-*b*-P4VP self assembly thin film on the spin coating speed was conducted, using the 0.5% PS-*b*-P4VP weight solution in DMF and under the argon purged ambient environment. Thin films were spin coated with various speeds from 1000

RPM to 3500 RPM. AFM metrology scans showed similar smooth and featureless surface profile for all of the samples, as shown in the left image of Figure 4.14. Then, the samples were put into THF solvent vapor annealing process for three hours to induce the self assembly and surface reconstruction. On the samples post the solvent annealing, the AFM metrology results showed a clear threshold, which is 1500 RPM found in our experiments, for the spin coating speed and hence the resulted film thickness. For the spin coating speeds below the threshold, the film was thick enough to support the formation of the lateral hexagonal self assembly of the copolymer blocks. For the spin coating speeds above the threshold, there were no observed self assembly because the spin coated films are too thin. The contrast is shown in Figure 4.15 below.

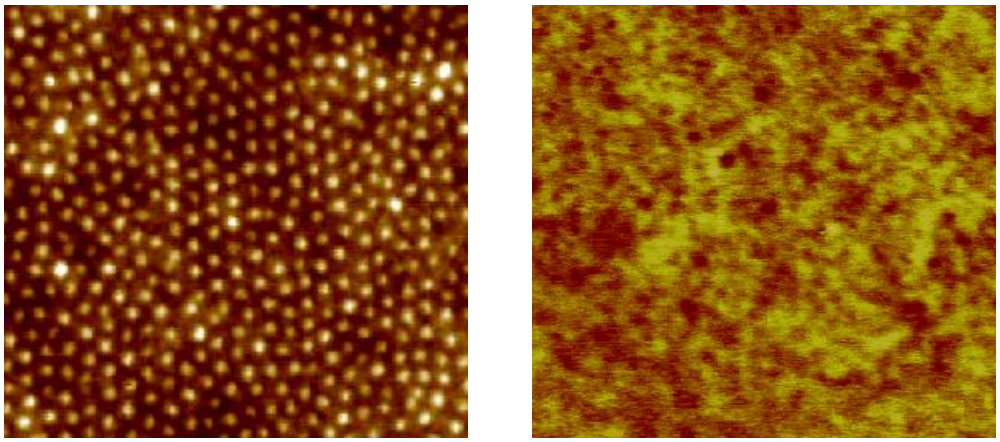

Figure 4.15 AFM height images of PS-*b*-P4VP thin films post THF solvent annealing. PS-*b*-P4VP dissolved in DMF by 0.5% weight concentration and spin coated in argon purged space. *Left*: Self assembly was observed on the thin films spin coated with speeds of 1500 RPM and below. *Right*: No noticeable change on the thin films spin coated with speeds above 1500 RPM.

With the appropriate film thickness and featureless surface profile after spin coating, I performed direct e-beam lithographic patterning on the PS-*b*-P4VP diblock

copolymer thin film, to induce the self assembly by the order as lithographic patterns defined in the following solvent annealing process. The designed goal was to crosslink the copolymer in the exposed area with high enough dosage, so that these solid area serve as the boundaries to confine the unexposed area in between and hence induce the guided self assembly with desired lateral orientation of ordering during the solvent annealing processes. The results were serendipitous compared to my anticipation. With high enough dosages, in the exposed area, there are ordered guided self assembly patterns and no self assembly in the proximity. This result is shown in Figure 4.16 below.

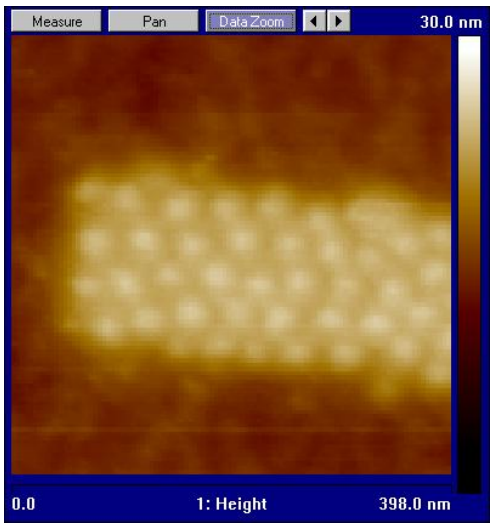

Figure 4.16 AFM height image of the guided self assembly after solvent annealing guided by EBL patterning. The bright nanodomain array is the area exposed by e-beam, and there is no ordered self assembly in the nearby unexposed area.

The sample shown in Figure 4.16 was patterned by EBL, using our JSM-6400 SEM equipped with NPGS EBL module. The electron acceleration voltage was set to 20kV, and the area dosage at the EBL patterned area was 10000 $\mu C/cm^2$. Immediately

after the EBL, AFM metrology scans showed no significant change applied to the featureless PS-*b*-P4VP thin film, as the metrology result shown in the left image of Figure 4.14. The samples then were put into THF solvent vapor annealing process at room temperature for four hours, and the nanostructures at the exposed area were observed by following up AFM metrology scans. It proves that this surface reconstruction occurred during the THF solvent annealing procedure.

A series of tests on the EBL patterning the featureless PS-*b*-P4VP thin film were conducted with a wide range of e-beam exposure dosages, followed by four hours THF solvent annealing to induce the self assembly. Presenting results with different dosages are shown in Figure 4.17 below. The e-beam exposure dosages used for the samples shown in Figure 4.17 (a), (b), (c) and (d) were 600 $\mu C/cm^2$, 2600 $\mu C/cm^2$, 3800 $\mu C/cm^2$ and 10000 $\mu C/cm^2$ respectively. In sample (a), it is most obvious that the proximity to the exposed area were not influenced much by the EBL patterning. Self assembly with the same lateral ordering and spatial dimensions as we observed previously on normal samples without e-beam exposure, were produced in these proximity area. In the exposed area, the ordering of the self assembly is significantly worse than the unexposed area. In sample (b) and (c), higher exposure dosages suppressed the formation of the self assembly in the proximity, but enhanced the uniform lateral ordering of the self assembly in the exposed area. Above certain high exposure dosage, as shown in sample (d), the extremely high dosage completely eliminated the nearby unexposed self assembly, and patterns formed in the exposed area were of the highest quality.

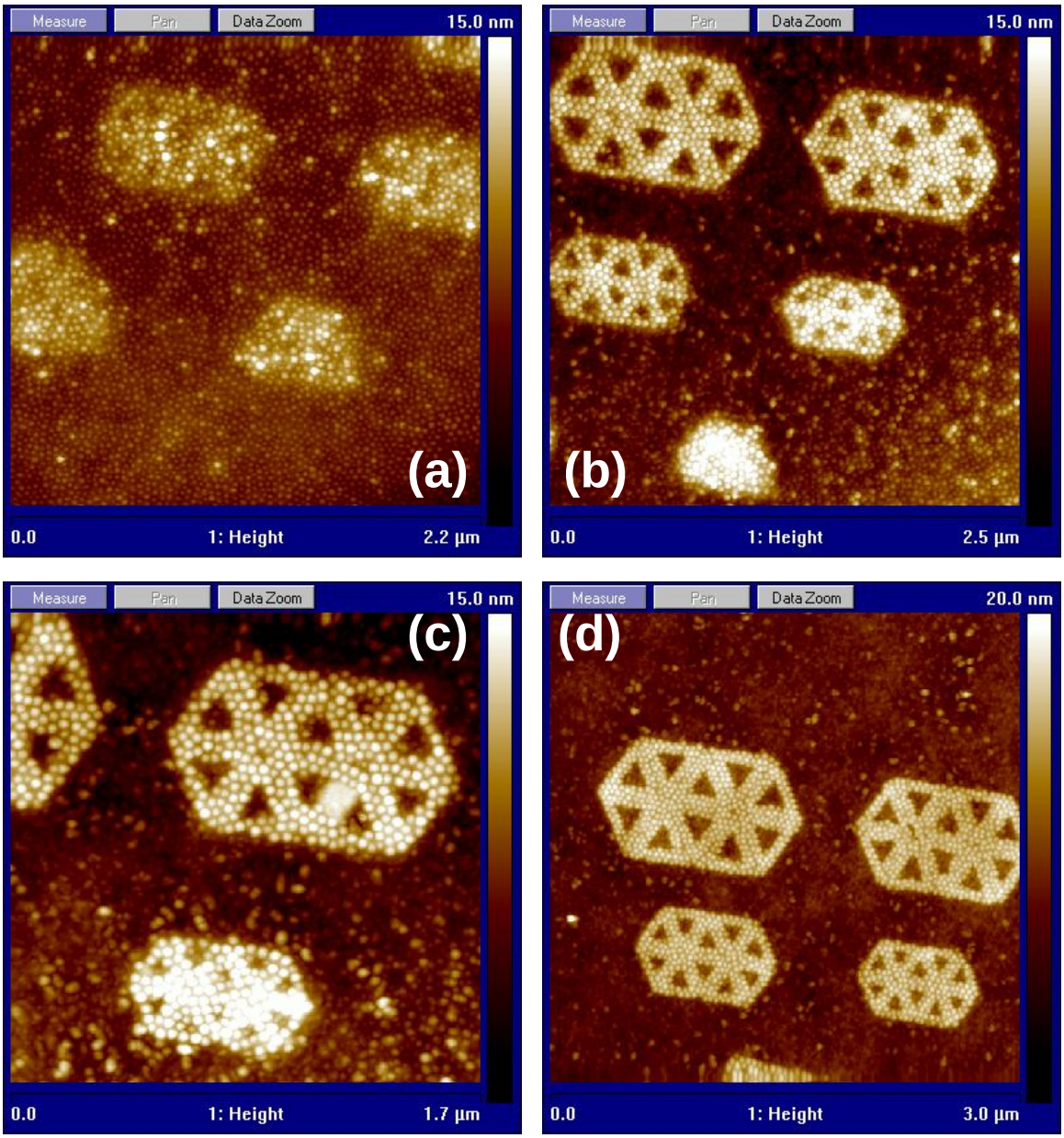

Figure 4.17 AFM height images of the EBL patterned featureless PS-*b*-P4VP thin films, followed by four hours THF solvent annealing process to induce the self assembly and surface reconstruction. Four different e-beam exposure dosages were used: (a) 600 µC/cm^2; (b) 2600 µC/cm^2; (c) 3800 µC/cm^2; (d) 10000 µC/cm^2.

One of the proposed explanations involves the EBL proximity effect. During e-beam exposure, the back scattered secondary electrons can expose a much larger area to the proximity of the EBL pattern. These secondary electrons are of much lower energies (less than 1 keV) [40] compared to the incident ones (20 keV in our case). These back scattered exposure events occurred to the nearby PS-*b*-P4VP will produce scission of the polymer chains and hence increase the polymer mobility greatly during the solvent annealing process. Inside the exposed area, the much higher exposure dosage crosslinks the copolymer chains. During the solvent annealing process, the broken chains from the proximity of the exposed patterns aggregate on the scaffolds of the crosslinked copolymers and form the self assembly after the surface reconstruction. This hypothesis has yet to be tested by further experiments.

The patterned samples were developed in ethanol for 30 minutes in the following up experiments. Surface reconstruction, which converts the nanoscale micelle array to nanoholes and keeps the lateral ordering and dimension of the self assembly, was observed. As an example, the sample patterned with 10000 $\mu C/cm^2$ and then developed in ethanol is shown in Figure 4.18 below. It proves the feasibility for further engineering of this method of pattern transfer.

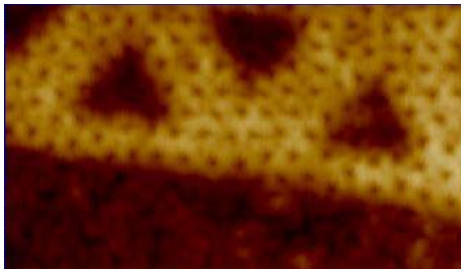

Figure 4.18 Surface reconstructions after 30 minute development in ethanol.

Ultra fine single period line of the diblock copolymer self assembly was also achieved by this method. As shown in Figure 4.19 below, a bullseye structure was first patterned by writing continuous concentric lines with EBL at 10 nC/cm line dosage on the featureless PS-*b*-P4VP thin film. Upon THF solvent annealing, the self assembly was induced and enhanced along the pattern exposed, and formed the semi-continuous bead lines. This kind of structures is of particular interests for certain plasmonic optical applications.

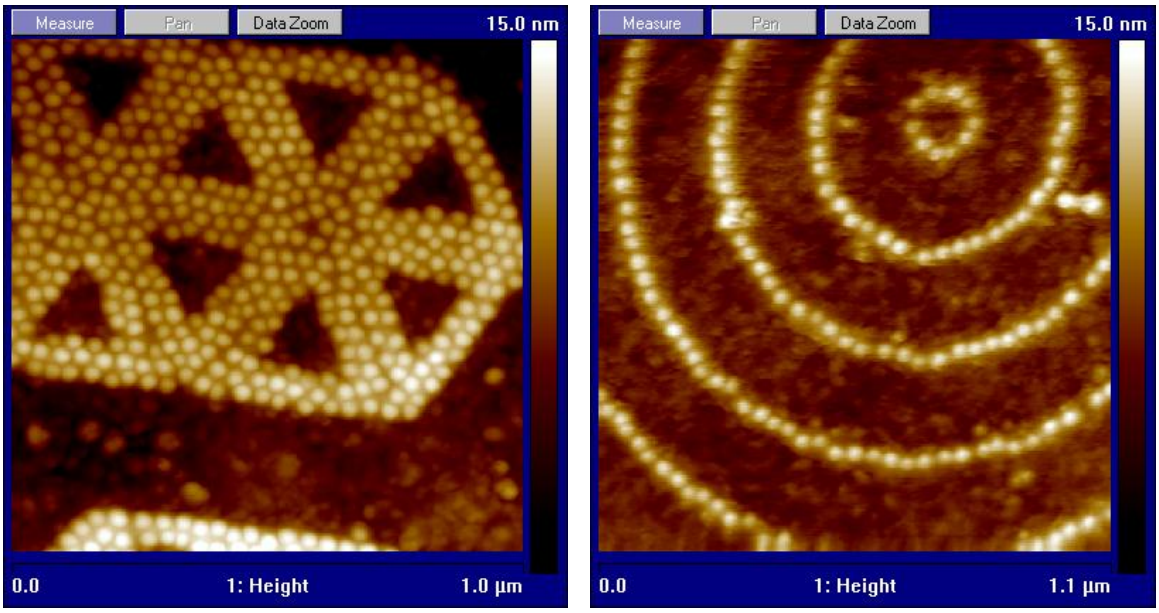

Figure 4.19 Examples of the best patterns generated so far. EBL patterning on originally featureless PS-b-P4VP (as spin coated) and followed by THF vapor annealing.

In summary, after the featureless PS-b-P4VP thin films were spin coated, we did direct EBL patterning on the film with various designed patterns, followed by four hours of THF solvent annealing at room temperature in order to introduce the self

assembly of copolymer. Although the concept is similar to the widely reported geographic epitaxial patterning of diblock self assemblies, this method does not require prerequisite substrate surface patterning. The results showed nearly perfect, and arbitrary, micro domain ordering defined by the EBL patterning. These unique features of this method are advantageous for experiments and applications that require ultra fine and complex nanotemplates.[64, 65]

4.3.3 Graphoepitaxy of self-assembled PS-*b*-P4VP

4.3.3.1 Nanofabrication processes and sample preparation

In Using the block copolymer self assembly as a patterning tool for nanofabrication, one of the critical issues is to control the size/spacing distribution and lateral ordering of the self assembly. Topographic features on the substrate surfaces, such as simple edges, well-defined trenches and more complex features, have been experimented to provide a way for controlling the hierarchical ordering where the bottom-up methods such as self-assembly of block copolymers are combined with the top-down lithographic methods.[41-48] Excellent examples include Professor C. A. Ross's group in MIT working on graphoepitaxy of self-assembled block copolymers on two-dimensional periodic patterned templates,[41] and Professor P. F. Nealy's group in University of Wisconsin working on guided self assembly by surface chemistry patterning.[24] However, in most previous work, the surface epitaxial patterns which had been studied most to confine and guide the block copolymer self assembles were of extremely large geometries, (e.g. long trenches and macroscale periodic array of

guiding features), compared to the characteristic scale of the block copolymer self assemblies. In our case, I introduce the idea of confining the copolymer self assembly within a closed system with an overall size comparable to the lattice period spacing of the self assembly. The topographic pattern was first defined by EBL (JSM-6400, with NPGS EBL module) on a suspended 100 nm SiN window and then transferred into the SiN layer via reactive ion etching (RIE). The detailed fabrication steps are described next.

A 100 nm thick suspended SiN window was first prepared with the procedure described in previous Section 3.1. A 70 nm thick poly(methylmethacrylate) (PMMA) film was spin coated using 2% PMMA solution in anisole (Microchem Corp.) at 4000 RPM spin speed. The film was immediately sequentially baked at 170ºC on a hot plate to remove the residual solvent and improve the surface roughness and adhesion to the substrate. An array of equilateral triangular patterns was written by EBL, with single line exposure dosage of 1.2 nC/cm at 20 keV electron energy and 5 pA e-beam current density. The exposed line patterns were developed in IPA(isopropyl alcohol):H_2O=3:1 (by volume) under 5 ^oC for 2 minutes. This procedure will remove the exposed PMMA and form the triangular trench patterns on the PMMA layer, hence expose the SiN substrate underneath the exposed patterns. The remaining PMMA layer served as the etching mask, for the following RIE steps to transfer the triangular patterns to the SiN substrate. Two RIE recipes were used during the etching process. The first one is the etching recipe: chamber pressure = 50 mTorr, RF power = 50W, CHF_3 gas flow rate = 30 sccm, processing time = 5 sec. The second one is the cleaning recipe: chamber pressure = 50 mTorr, ICP power = 50W, SF_6 gas flow rate = 30 sccm, processing time

= 5 sec. These two steps were iterated for 5 times each. Any residual PMMA were removed by the final oxygen plasma cleaning for 10 minutes. The final nanostructure templates fabricated are shown in Figure 4.20 below.

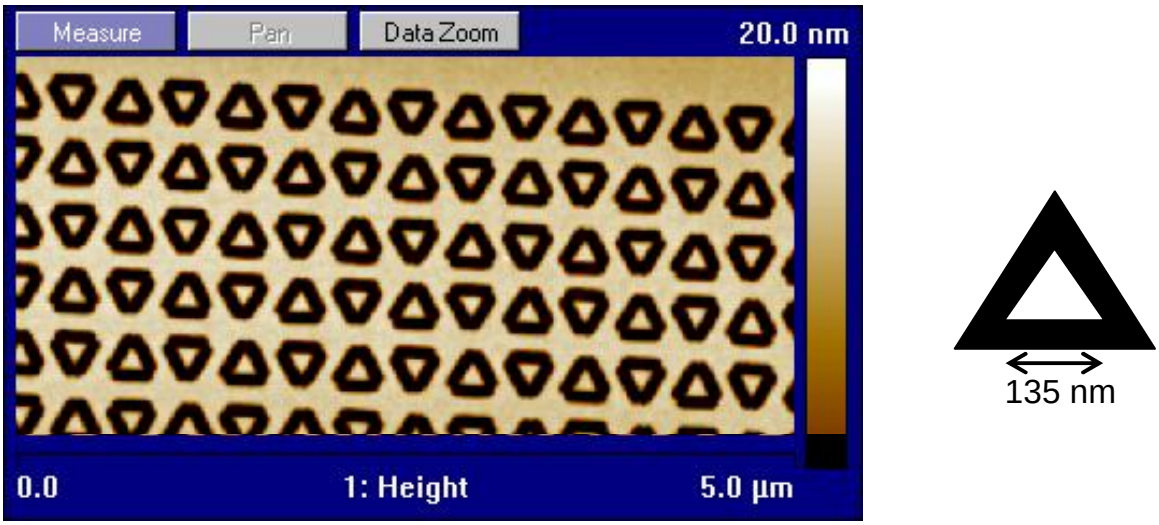

Figure 4.20 Patterns of equilateral triangular trenches transferred from EBL to suspend SiN membrane by EBL, development and RIE.

Due to the ultra fine nanostructure resolution required by the nature of the experiments, there are certain cautions I have taken during the fabrication which are worth of notice. The PMMA layer serves as the RIE etching mask, which dominates the quality of the pattern transferring from EBL to the substrate. So, it is mandatory to achieve straight accurate sidewall profiles along the cross sections of the PMMA patterns after EBL and development. Normal EBL on thick silicon wafer has proximity effects and undercut profiles for the cross sections of the developed features due to the back scattered secondary electrons. This is the reason that I used the suspended SiN window instead of normal silicon wafers, and the low temperature development

process with weaker reagent (IPA:H_2O) instead of the stronger developers methyl isobutyl ketone/IPA (1:3) at room temperature.

Given the fabrication requirement to have an anisotropic etching profile and accurate nano pattern transferring, RIE was chosen for the etching process instead of wet chemical etching method. The iteration of the two etching recipes during the RIE process is necessary due to the etching chemistry using the etching gas CHF_3. During the SiN etching process, it also forms Teflon-like cross lined C-F network covering the sample surface which eventually stops the etching. The alternative cleaning steps, by isotropic SF_6 RIE etching, will remove the polymerized film so that the etching procedure can continue. This concept is similar to the Bosch process for DRIE. [66]

PS-*b*-P4VP (number-average molecular weight Mn^{PS} = 41.5 kg/mol, Mn^{P4VP} = 17.5 kg/mol, molecular weight distribution Mw/Mn = 1.07) micelle solution with 0.5% weight concentration in toluene was spin coated onto the patterned SiN surface at 3200 RPM spin speed. The film as spun showed the randomly distributed micelle array on the substrate, as described in previous sections. This is also shown in Figure 4.21. Upon THF annealing, surface reconstruction was induced, and the resulted film showed improved lateral ordering and better uniform domain distribution, as shown in Figure 4.21. In the area of nanoscale triangular islands isolated from the main substrate by the nanopatterned trenches, ordered triangular array of the PS-*b*-P4VP micelles with discrete numbers of microdomains were observed, guided by the hierarchical confinement of the surrounding trenches. A series of test patterns with different sizes of the equilateral triangular confinement were fabricated. The EBL written single lines on PMMA showed a line width of 50 nm after the development and pattern

transferring, and the smallest final fabricated triangular features on SiN membrane have an average side length of 135 nm, as shown in Figure 4.20. These features were found to enable the finest nanostructures after applying the PS-*b*-P4VP film and the following solvent annealing process, as shown in Figure 4.21.

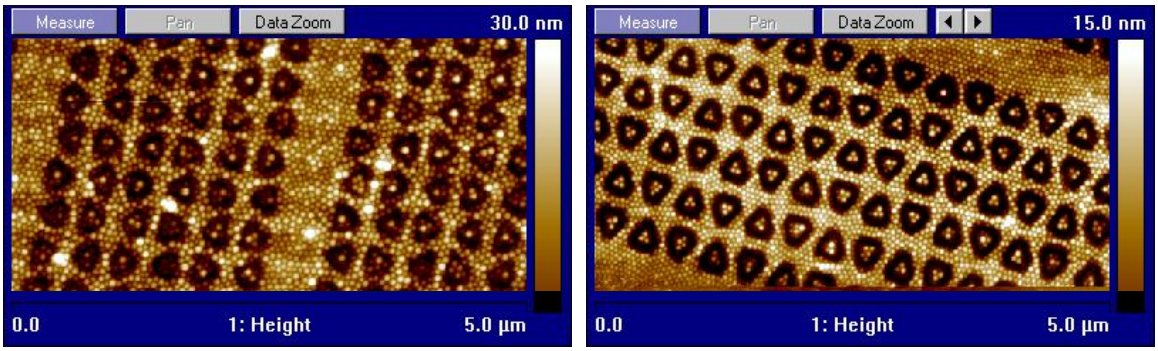

Figure 4.21 AFM height images of the PS-*b*-P4VP micelle array spin coated on the textured SiN substrate (as shown in figure 44). *Left*: The original film after spin coating. *Right*: Surface reconstructed PS-*b*-P4VP ordered array after THF solvent annealing.

As shown in Figure 4.21, most observations indicated a commensurate fitting of either three or six microdomains on top of the isolated SiN plateaus. This is addressed by the circular indicators in Figure 4.22.

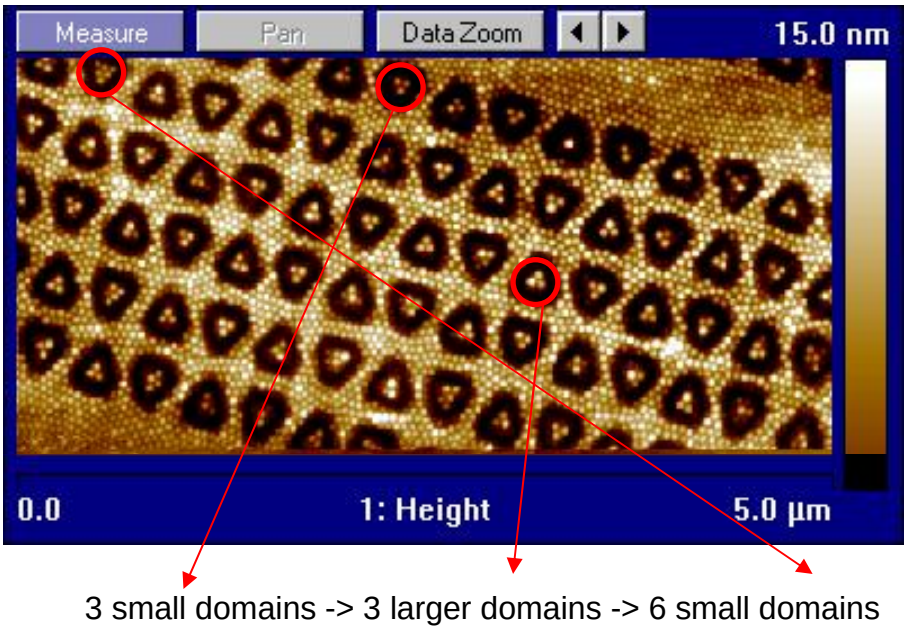

Figure 4.22 Distribution of clusters of different sizes and numbers of the PS-*b*-P4VP microdomains after THF solvent annealing.

4.3.3.2 Theoretical consideration and explanation

It is of particular interest to explore the physics which dominates the distribution of the clustered self assembly sizes and numbers of elements, in order to achieve precise control of the guided self assembly lateral ordering in this case. The resulting self-assembled microphase separation morphologies minimize the Gibbs free energy of the system, $F = H - TS$. For the two components of the free energy, the enthalpy H is related with the block-block interfacial energy which is proportional to the interfacial area of the PS and P4VP blocks; the entropic energy –TS represents the elastic energy related with the temperature. To minimize the enthalpy it requires minimum PS and P4VP block interfacial area, but this is not favored by the entropic energy term because the blocks are compressed or expanded too much. The

competition between the enthalpy and the entropic energy determines the balance point which gives rise to the final configuration of the self assembly.

In order to simplify the theoretical consideration of the system, the self assemblies on the isolated SiN features are approximated as ideal closely packed spherical micelles, as shown in Figure 4.23. The red blocks inside the micelles are P4VP core with the inner radius r_A, and the blue blocks outside are PS shell with the outer radius r_B.

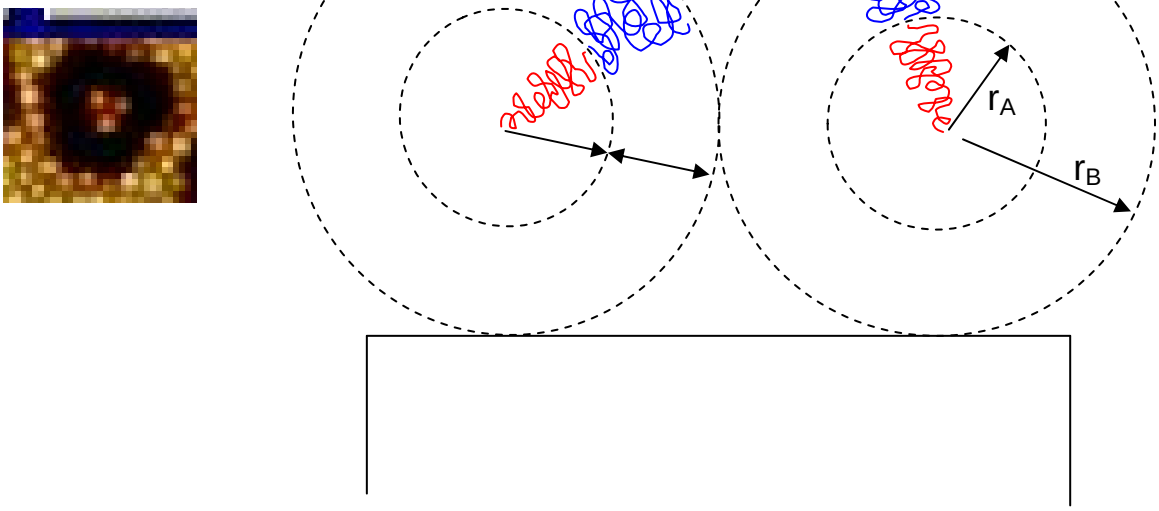

Figure 4.23 Approximation of the self assembly system on the isolated SiN islands for theoretic calculation: Ideal close packing of spherical micelles.

The theoretical treatment below adapts concepts from the earlier work.[67, 68, 69] For a hypothetic state of a linear polymer chain with ***n*** identical repeating monomeric segments of the same unit length ***l***, we can first simplify the calculation by making the assumption in which the bond angle restrictions are retained but the steric hindrances to internal rotations are released. The mean-square end-to-end distance of such freely rotating chains can be readily calculated from the known basic structures of the chains. In our case (PS and P4VP), for the vinyl polymer chains, the C-C segment length is 0.154 nm. For sufficiently long chains, the mean-square end-to-end distance is: $nl^2 \frac{1+\cos\theta}{1-\cos\theta}$, where cosθ = 1/3.

In real polymer chains there exist long-range interactions between monomeric segments and the effect of steric hindrance. To calculate the mean end-to-end distance of the chain in this case, a convenient method is to define the Kuhn statistical segment number $\boldsymbol{n_k}$ and Kuhn statistical segment length $\boldsymbol{l_k}$.[49] For a linear polymer chain with ***n*** identical repeating monomeric segments of the same unit length ***l,*** it can be considered as an effective freely joint polymer chain with $\boldsymbol{n_k}$ repeating monomeric segments of the length $\boldsymbol{l_k}$. Flory characteristic ratio (49) $C_\infty = \frac{< R^2 >_0}{nl^2}$ defines the relationship between the native parameters ***n***, ***l*** and the statistical parameters $\boldsymbol{n_k}$ and $\boldsymbol{l_k}$,

$$n_k = \frac{n}{C_\infty}, \qquad l_k = l \cdot C_\infty$$

Please notice that C_∞ is dependent on the temperature, solvent and the state of the polymer chain; we make the assumption that C_∞ is constant to simplify the theoretic consideration in this work. For instance, the Kuhn segment lengths for the polymer

chains (l_k = 0.73 nm for P4VP and 0.68 nm for PS, denoted as ***a*** and ***b*** for the rest of the discussion) are taken from the reference [50] in our calculation below. These Kuhn segment lengths determine the Flory characteristic ratio by $C_\infty = \frac{l_k}{l}$, which gives C_∞ = 4.4 for PS and 4.8 for P4VP.

For the copolymer we use in the experiments, Mn^{PS} = 41.5 kg/mol, Mn^{P4VP} = 17.5 kg/mol. Given the molecule weights of the styrene (104.15 g/mol) and vinyl pyridine (105.14 g/mol) monomers, the segment numbers are estimated to be 398 and 166 for the PS and P4VP blocks, respectively. The Kuhn statistical segment numbers are calculated as

$$n_{PS} = \frac{n}{C_\infty} = \frac{398}{4.4} \approx 90, \qquad n_{P4VP} = \frac{n}{C_\infty} = \frac{166}{4.8} \approx 35$$

The diblock copolymer chains can be considered as Hookean elastic springs; any deformation (compressing or extending) of the blocks will cost certain amount of the entropic energy. In the reference state (unperturbed coil), the dimension of the polymer chains can be evaluated with the Kuhn statistical values. By comparing the dimension of the system in the state of our interests to the reference state, one can calculate the deformation factors and hence the cost of entropic energy. The unperturbed coil state and the deformed state of our micelle system are illustrated in Figure 4.24 below. Please note that the wedge constrains of the copolymer chains and the end points were averaging approximation of the real situations.

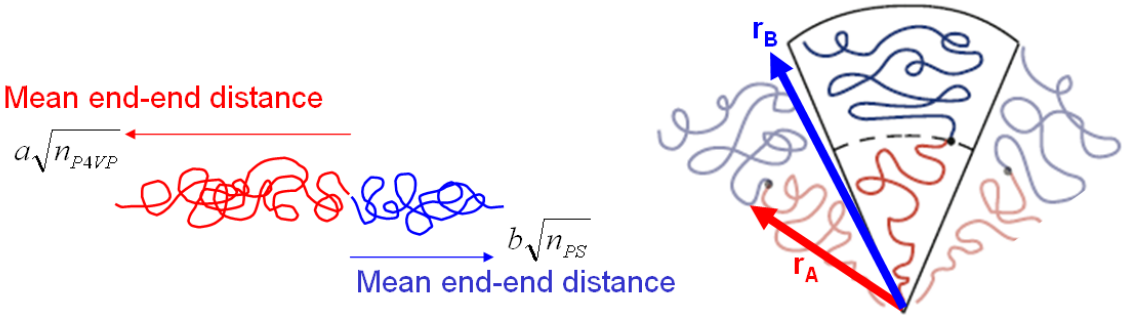

Figure 4.24 Illustration of the reference state and the deformed state for the micelles. The red blocks stand for P4VP chains, and the blue blocks stand for PS chains. *Left*: Unperturbed coil chains as the reference state. *Right*: Deformed micelle state. ***a*** and ***b*** are Kuhn statistical length for P4VP and PS respectively.

In the reference state of a single PS-*b*-P4VP copolymer chain, the mean end-end distance for the P4VP and PS blocks are $a\sqrt{n_{P4VP}}$ and $b\sqrt{n_{PS}}$ respectively. n_{PS}, n_{P4VP}, a,b are the Kuhn statistical segment parameters as we discussed previously. The deformation amplitude of the P4VP blocks is referred with the strain factor h_A:

$$h_A = \frac{r_A}{a\sqrt{n_{P4VP}}}$$

and similarly for the PS blocks we have the strain factor h_B:

$$h_B = \frac{r_B - r_A}{b\sqrt{n_{PS}}}$$

Given the known volume fraction $f = \frac{V_{P4VP}}{V_{PS}} \approx \frac{3}{7}$ of the diblock copolymer, we have

$$r_B = (1+\frac{1}{f})^{\frac{1}{3}} r_A \approx 1.5 r_A$$

The entropic energy costs per chain for the PS and P4VP blocks upon the formation of the micelles are, compared to the reference state:[41]

$$\text{P4VP blocks: } \Delta F_A = \frac{k_B T}{2}(h_A^2 + \frac{2}{h_A} - 3)$$

$$\text{PS blocks: } \Delta F_B = \frac{k_B T}{2}(h_B^2 + \frac{2}{h_B} - 3)$$

The enthalpy of the PS-b-P4VP micelle can be evaluated with the interfacial tension γ_{AB} between the PS and P4VP blocks (Helfand-Tegami expression):[41]

$$\gamma_{AB} = \frac{k_B T}{h^2}\sqrt{\frac{\chi_{AB}}{6}}$$

Where ***h*** is the Kuhn statistic segment length for the whole copolymer chain, and χ_{AB} = 0.3~0.35 is the Flory-Huggins parameter of the PS-*b*-P4VP copolymer.[51] The average Kuhn segment length can be calculated by

$$h = (\frac{f_{P4VP}^V}{a^2} + \frac{f_{PS}^V}{b^2})^{-\frac{1}{2}} = 0.69(nm)$$

where $f_{P4VP}^V = 0.3$ and $f_{PS}^V = 0.7$ are the volume fraction of each blocks in the chain. The total enthalpy per micelle is the product of the interfacial area and γ_{AB}

$$H = 4\pi \cdot r_A^2 \frac{k_B T}{h^2}\sqrt{\frac{\chi_{AB}}{6}}$$

Assuming the density of the P4VP core remains constant as the value from the reference [52] (1.114 g/cm^3, at 20 ^{o}C), the effective volume of a single P4VP chain with 166 monomeric vinyl pyridine units inside the core is estimated to be 26 nm^3. Upon these assumptions, the micelle core diameter r_A is a function of the total number N of the aggregated copolymer molecules:

$$\frac{4}{3}\pi \cdot r_A^3 = N \cdot 26\,(nm^3)$$

It is obvious that r_A is a discrete step function of N, but for large enough N the function is quasi-continuous. The enthalpy per molecule chain can be then written as:

$$H_{PerChain} = \frac{H}{N} = \frac{4\pi \cdot r_A^2 \frac{k_B T}{h^2}\sqrt{\frac{\chi_{AB}}{6}}}{\frac{4}{3}\pi \cdot r_A^3 / 26} = \frac{78(nm^3)k_B T}{h^2 r_A}\sqrt{\frac{\chi_{AB}}{6}}$$

With the above derivations, we can readily write the total free energy of the micelle system per molecule chain by adding up the entropic energy per chain (ΔF_A and ΔF_B) and enthalpy per chain ($H_{PerChain}$):

$$\frac{F}{k_B T} = \frac{1}{2}(h_A^2 + \frac{2}{h_A} - 3) + \frac{1}{2}(h_B^2 + \frac{2}{h_B} - 3) + \frac{78(nm^3)}{h^2 r_A}\sqrt{\frac{\chi_{AB}}{6}}$$

With all of the previous discussion, and set χ_{AB} = 0.34, we can simplify the equation above to:

$$\frac{F}{k_B T} = 0.0298\frac{r_A^2}{(nm^2)} + 56.22\frac{(nm)}{r_A} - 3$$

This formula gives direct prediction on the PS-*b*-P4VP micelle size. For a single micelle, the free energy dependence on the micelle core size (r_A) is plotted in Figure 4.25 below. It shows that the free energy (per chain) minimum which most favors the formation of a single micelle is around 10 nm, and hence implies the radius of the whole micelle is around 15 nm.

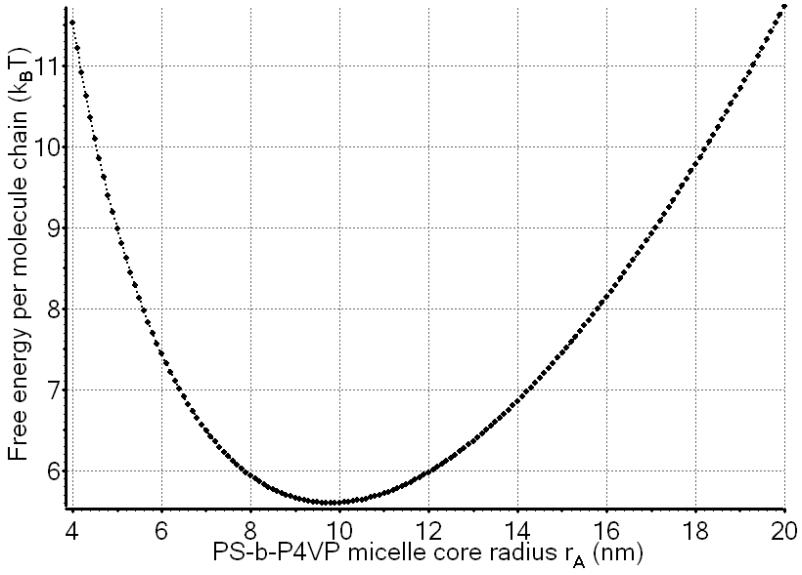

Figure 4.25 Free energy (per molecule chain) dependence on the size of the micelle.

In our experiments we observed a spontaneous formation of clusters with different sizes and geometries on the SiN islands, as indicated in Figure 4.22. Random uneven distribution of the polymer material on top of the SiN plateau during the spin coating process is the reason for this phenomenon. Due to the equilateral triangular geometry of the SiN plateau, it is natural to consider the changing of the micelle clusters from the 3-micelle cluster to the 6-micelle cluster for commensurate fitting of the microdomains. If there are total N copolymer molecules deposited on the plateau, we can arbitrarily divide them into either 3 micelles or 6 micelles. In the 3-micelle cluster state, the micelle core radius r_{A3} can be evaluated by $\frac{4}{3}\pi \cdot r_{A3}^3 = \frac{N}{3} \cdot 26(nm^3)$; in the 6-micelle cluster state the micelle core radius r_{A6}: $\frac{4}{3}\pi \cdot r_{A6}^3 = \frac{N}{6} \cdot 26(nm^3)$. The free energy per molecule chain can be compared in the 3-micelle cluster state and the 6-

micelle cluster state, using the same equations described for the single micelle case. The result is plotted in Figure 4.26 below.

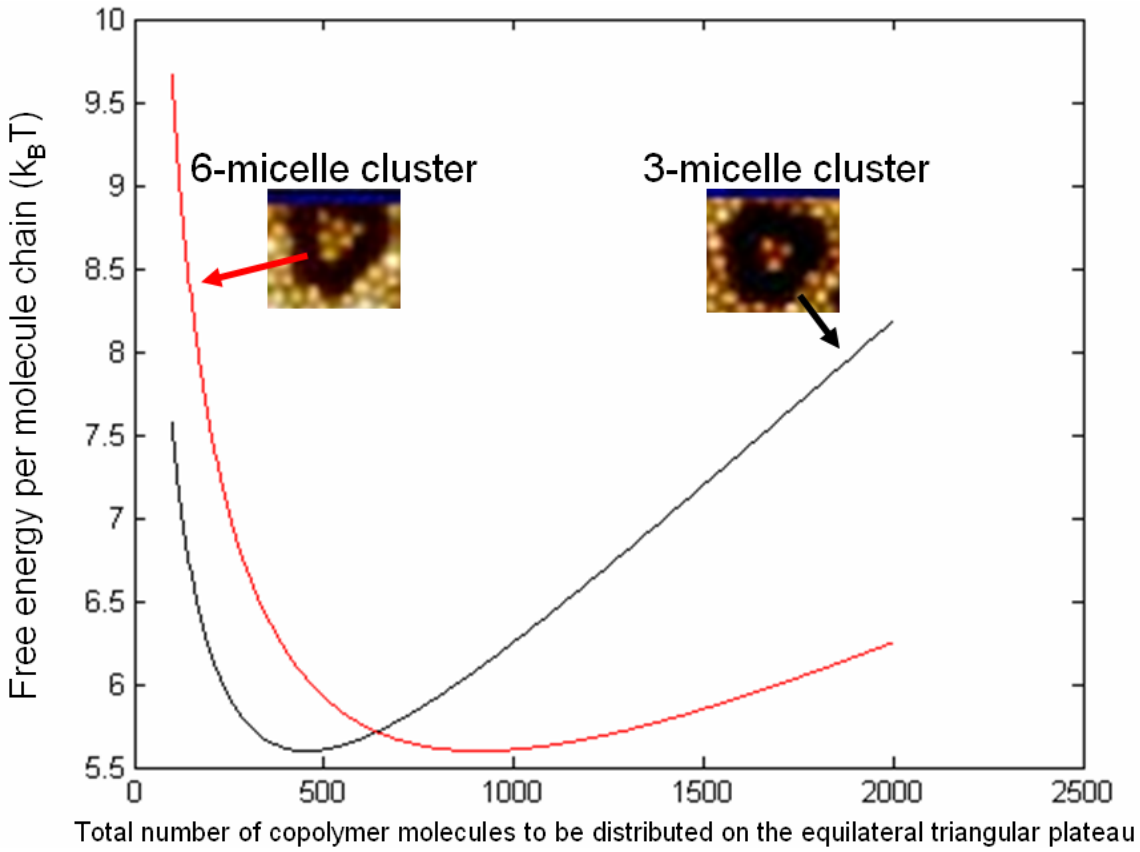

Figure 4.26 Free energy (per chain) comparison for the 3-micelle cluster and the 6-micelle cluster configurations, given the total number of the copolymer chains deposited onto the plateau.

Figure 4.26 clearly demonstrated that a change of number of the elements in the microdomain clusters will occur, when the total number of copolymer chains deposited onto the plateau approaches a threshold (N = 640). At the threshold, the radius of the micelle core for the 3-micelle cluster is about 11 nm, and for the 6-micelle cluster it is 8.7nm. When the amount of the copolymer chains deposited onto the plateau changes

across the threshold point, an abrupt change of the size of the micelles will happen along with the change of the cluster's microdomain number.

To conclude, guided self assembly inside such hierarchical nanoscale structures addresses two significant features: commensurate compatibility and discrete distribution of the individual nanoelements of the self assembly. The experiment results showed a unique way to fabricate arrays of diblock copolymer self assembly clusters with well-controlled nanostructures. The theoretic consideration gave a clear image on the physics beyond the changing of the cluster's size and geometry, and it can be used to guide future fabrication efforts to precisely control the formation of the self assembly clusters. Further possibility for nanofabrication after the pattern transferring is particularly appealing to applications, for instance, the perpendicular three-bit interacting nanomagnet clusters for data storage devices.

4.4 References

1. M. Park, *et al., Science* **276,** 1401 (1997)

2. J. Y. Cheng *et al.*, *Adv. Mater.* **13,** 1174 (2001)

3. J. P. Spatz *et al*., *Adv. Mater.* **11,** 149 (1999)

4. C. T. Black *et al.*, *Appl. Phys. Lett.* **79,** 409 (2001)

5. K. W. Guarini *et al,. IEEE Electron Devices Mtg Tech. Digest*, 541 (2003).

6. C. A. Ross, *Annu. Rev. Mater. Res.* **31,** 203 (2001).

7. S. A. Maier *et* al., Adv. *Mater.* **13,** 1501 (2001).

8. F. S. Bates, G. H. Fredrickson, *Annu. Rev. Phys. Chem.* **41**, 525 (1990)

9. M. J. Park et al., *Nano Lett.* **7**, 3547 (2007)

10. N. Hadjichristidis et al., *Block Copolymers: Synthetic Strategies, Physical Properties, and Applications* (Wiley, 2002)

11. C. Burger *et al*., *Handbook of Polyelectrolytes and Their Applications* (American Scientific Publishers, 2002)

12. E.W. Cochran *et al., Macromolecules*, **39**, (2006)

13. J. Chen, M. Zhang, L.Yang, M. Collins, J. Parks, A. Avallone and T. P. Russell, *Journal of Polymer Science B* **20**, 2912 (2007)

14. Y. S. Jung and C. A. Ross, *Nano Lett.* **7**, 2046 (2007)

15. S. Ji *et al*., *Adv. Mat.* **16**, 3054 (2008)

16. P. Mansky, Y. Liu, E. Huang, T.P. Russell and C.J. Hawker, *Science* **275**, 1458 (1997)

17. P. Mansky, T.P. Russell, C.J. Hawker, M. Pitsikalis and J. Mays, *Macromolecules* **30**, 6810 (1997)

18. E. Huang, P. Mansky, T.P. Russell, C. Harrison, P.M. Chaikin, R.A. Register, C.J. Hawker and J. Mays, *Macromolecules* **33**, 80 (2000)

19. J. Heier, E.J. Kramer, S. Walheim and G. Krausch, *Macromolecules* **30**, 6610 (1997)

20. R.D. Peters, X.M. Yang, T.K. Kim, B.H. Sohn and P.F. Nealey, *Langmuir* **16**, 4625 (2000)

21. W.J. Dressick and J.M. Calvert, *Jpn. J. Appl. Phys.* **32**, 5829 (1993)

22. M. P. Stoykovich, M. Müller, S. O. Kim, H. H. Solak, E. W. Edwards, Juan J. de Pablo and P. F. Nealey, *Science* **308**, 1442 (2005)

23. C. Tang, E. M. Lennon, G. H. Fredrickson, E. J. Kramer and C. J. Hawker, *Science* **322**, 429 (2008)

24. R. Ruiz *et al.*, *Science* **321**, 936 (2008)

25. Du Y. Ryu, K. Shin, E. Drockenmuller, C. J. Hawker and T. P. Russell, *Science* **308**, 236 (2005)

26. T. Thurn-Albrecht, J. Schotter, G.A. Kästle, N. Emley, T. Shibauchi, L. Krusin-Elbaum, K. Guarini, C. T. Black, M. T. Tuominen and T. P. Russell, *Science* **290**, 2126 (2000).

27. M. Doi and S. F. Edwards *Theory of Polymer Dynamics* (Academic Press 1986)

28. T. L. Morkved et al., *Science* **273**, 931 (1996)

29. K. Amundson, E. Helfand, X. Quan, S. D. Smith, *Macromolecules* **26**, 2698 (1993)

30. M. Bal, A. Ursache, J. Goldbach, T.P. Russell, and M.T. Tuominen, *Applied Physics Letters* **81**, 3479 (2002)

31. A. Ursache, J. T. Goldbach, T. P. Russell, and M. T. Tuominen, *J. Appl. Phys.* **97**, 10J322 (2005)

32. A. Ursache, M. Bal, J. T. Goldbach, R. L. Sandstrom, C. T. Black, T. P. Russell and M. T. Tuominen, *Mater. Res. Soc. Symp. Proc.* **721**, E3.3 (2002)

33. D. J. Sellmyer, M. Zheng and R. Skomski, *J. Phys. Condens. Matter* **13**, R433 (2001)

34. C. T. Black and O.Bezencenet, *IEEE Nanotechnology* **3,** 3 (2004)

35. T. Xu, C. J. Hawker, and T. P. Russell, *Macromolecules* **36**, 6178 (2003)

36. B. Kim, S. Park, T. J. McCarthy and T. P. Russell, *Small* **3 No. 11**, 1869 (2007)

37. T. Xu, J. Stevens, J. Villa, J. T. Goldbach, K.W. Guarini, C. T. Black, C. J. Hawker and T. P. Russell, *Adv. Funct. Mater*. **13**, 698 (2003)

38. S. Park, J. Y. Wang, B. Kim, J. Xu and T. P. Russell, *Adv. Mater*. (2007)

39. S. Park, O. Yavuzcetin, B. Kim, M.T. Tuominen and T.P. Russell, *Small* **5**, 1064 (2009).

40. P.Rai-Choudhury, *Handbook of Microlithography, Micromachining and Microfabrication* (SPIE, 1997)

41. I. Bita *et al., Science* **321**, 939 (2008)

42. R. Ruiz *et al., Science* **321**, 936 (2008)

43. R. A. Segalman, H. Yokoyama and E. J. Kramer, *Adv. Mater*. **13**, 1152 (2001)

44. J. Y. Cheng, C. A. Ross, E. L. Thomas, H. I. Smith, G. J. Vancso, *Appl. Phys. Lett.* **81**, 3657 (2002)

45. L. Rockford *et al., Phys. Rev. Lett*. **82**, 2602 (1999)

46. S. O. Kim *et al., Nature* **424**, 411 (2003)

47. E. W. Edwards, M. F. Montague, H. H. Solak, C. J. Hawker and P. F. Nealey, *Adv. Mater.* **16**, 1315 (2004)

48. M. P. Stoykovich *et al., Science* **308**, 1442 (2005)

49. G. Strobl, *The Physics of Polymers*, (Springer, 2007)

50. E. Helfand and Z. R. Wasserman, *Macromolecules* **11**, 960 (1978)

51. G. O. R. Alberda van Ekenstein, R. Meyboom, and G. ten Brinke, *Macromolecules* **33**, 3752 (2000)

52. J. E. Mark, *Polymer Data Handbook* (Oxford University Press, 1999)

53. G. Brown, M.A. Novotny, and P.A. Rikvold, *Phys. Rev. B.* **64**, 134422 (2001)

54. G. Brown, M.A. Novotny, and P.A. Rikvold, *J. Appl. Phys.* **87**, 4792 (2000)

55. H. A. Kramers, *Physica* (Utrecht) **7**, 284 (1940)

56. D. O. Shin *et al., Macromolecules* **42**, 1189 (2009)

57. Th. Dittrich, H. Angermann, W. Füssel, H. Flietner *Physica Status Solidi (a)* **140**, 463 (2006)

58. J. M. C. Thornton *et al., Semicond. Sci. Technol.* **4**,847 (1989)

59. G. Riess, *Prog. Polym. Sci.* **28**,1107 (2003)

60. S. H. Kim *et al., Adv. Mat*. **16**, 226 (2004)

61. G. Kim, M. Libera, *Macromolecules* **31**, 2670 (1998)

62. A. Sidorenko, I. Tokarev, S. Minko, M. J. Stamm, *Am. Chem. Soc.* **125**, 12211 (2003), 125 (40)

63. W. van Zoelen, T. Asumaa, J. Ruokolainen, O. Ikkala, G. ten Brinke, *Macromolecules* **41**, 3199 (2008)

64. A. Agrawal *et al.*,*New J. of Phys* **7**, 249 (2005)

65. T. M. Rumke *et al., Opti. Exp*. **16**,5013 (2008)

66. Z. Cui, *Nanofabrication: Principles, Capabilities and Limits* (Springer, 2008)

67. J. Brandrup and E. H. Immergut, *Polymer Handbook* (Wiley, 1989)

68. M. Rubinstein, R. H. Colby, *Polymer Physics* (Oxford University Press, 2003)

69. D. I. Bower, *An Introduction to Polymer Physics* (Cambridge, 2002)

CHAPTER 5

SUMMARY AND FINAL OUTLOOK

As the final conclusion, this thesis and related work were inspired by a technique challenge from the magnetic media data storage industry. By further scaling down the bit size and increasing the storage density, the size of the individual bits becomes incompatible with the read/write mechanism because the interaction between the nanoelements of the media becomes significant enough to cause collective switching. Is there a way to overcome this difficulty with the increasing bit density in the modern magnetic bit media? To answer this question, we proposed a novel diagram that uses clusters of interacting nanomagnets instead of individual nanomagnet as the basic access units of the media. Our micromagnetic simulation work gave theoretic predictions on the magnetic switching behaviors of the clusters. Proof-of-concept fabrication proved the availability of the distinctive cluster magnetostatic states. Guided diblock copolymer self assembly were experimented to prove the feasibility of scaling down the devices with the anticipated configurations, with qualitative theoretic explanation on the copolymer microdomain formation.

There are new questions emerging from this work. The proposed multilevel cluster devices depend on the distinctive magnetostatic states of the clusters. The degeneracy is taken into account as if the symmetry of the clusters is defect free. In the real applications, what is the tolerance of defects for the device to perform as designed? These defects can include shift of single element, deformation of the whole cluster, and asymmetric magnetic properties of the nanomagnets. With the size scaled

down by the media fabricated from the copolymer self assembly, the interaction between the nanomagnets and thermal stability of the cluster's magnetostatic states are dominant factors of the clusters. How strong the magnetic material is required to be and what structure of the nanomagnets are yet to be determined for the proposed devices.

The unexpected guided self assembly by direct EBL needs explicit explanation beyond the hypothesis. Our theoretic treatment for the graphoepitaxy of self-assembled PS-*b*-P4VP template on the SiN plateau includes certain simplifying assumptions, e.g. perfect spherical shape of the micelles, ignorance of the solvent-micelle interfacial energy, and ideal elastic spring approximation of the copolymer blocks with well-defined average dimensions. How correct these assumptions are needs to be further tested.

The project can be readily moved into the next phase. It requires precise pattern transferring to convert the self-assembled copolymer template to perpendicular nanomagnet arrays. Strong magnetic materials with perpendicular magnetic anisotropy, e.g. Pd/Co multilayer heterostructure, are to be tested for the fabrication efforts. Given the extremely small nanostructures, well-focused micromagnetism study is necessary, in order to find the appropriate perpendicular anisotropy, magnetic moment strength, and underlying structures to optimize magnetic interaction between the cluster elements for the most distinctive magnetostatic states. Statistical study of large arrays of the clusters needs to be done, in order to research the switching field distribution based on the degenerated magnetostatic states of the clusters and the thermal stability of these states.

In order to test the hypothesis of the EBL induced PS-*b*-P4VP self assembly, the cross section profile study of the patterned thin film can be done. If the hypothesis is correct, the depletion of copolymers at the proximity of the exposed area will give a contrast to the unaffected area. By rinsing the sample in strong solvent to remove the migrated and self-assembled copolymer chains, the crosslinked templates at the EBL patterned area will be exposed. The comparison of the cross section profiles can reveal how the copolymer materials are distributed after the EBL and THF solvent annealing.

The formation of the three-domain clusters on SiN plateau by graphoepitaxy of self-assembled PS-*b*-P4VP is to be improved. Uniform distribution of the spin coated copolymer thin film can be achieved from the solution in a strong solvent of both PS and P4VP blocks, e.g. DMF. Statistical study of the array of self-assembled diblock copolymer multiple domain clusters on identical SiN equilateral triangular plateaus will show the distribution of the cluster's size and number of microdomains, thus give an insight to the free energy barrier associated with different cluster configurations to improve the theoretical model for the hierarchical graphoepitaxy of the self assembly. Along with all the exciting challenges, the research can be used in other applications that demand precise nanoscale patterning, e.g. MQCA [1] for magnetic logic gates and circuits.

[1] A. Orlov, A. Imre, G.Csaba, L. Ji, W.Porod, G.H.Bernstein, *J. of Nanoelectronics and Optoelectronics* **3**, 1-14 (2008)

BIBLIOGRAPHY

A. Agrawal *et al.*,*New J. of Phys* **7**, 249 (2005)

G. O. R. Alberda van Ekenstein, R. Meyboom, and G. ten Brinke, *Macromolecules* **33**, 3752 (2000)

M. Albrecht, G. Hu, A. Moser, O. Hellwig and B. D. Terris, *J. Appl. Phys.*, **97**, 103910 (2005)

K. Amundson, E. Helfand, X. Quan, S. D. Smith, *Macromolecules* **26**, 2698 (1993)

M. Bal, A. Ursache, J. Goldbach, T.P. Russell, and M.T. Tuominen, *Applied Physics Letters* **81**, 3479 (2002)

F. S. Bates, G. H. Fredrickson, *Annu. Rev. Phys. Chem.* **41**, 525 (1990)

R. Behrisch and W. Eckstein, *Sputtering by Particle bombardment: Experiments and Computer Calculations from Threshold to Mev Energies*. (Springer, Berlin. 2007)

G. Bertotti, *Hysteresis in Magnetism* (Academic Press, 1998).

I. Bita *et al.*, *Science* **321**, 939 (2008)

C. T. Black *et al.*, *Appl. Phys. Lett.* **79,** 409 (2001)

C. T. Black and O.Bezencenet, *IEEE Nanotechnology* **3,** 3 (2004)

D.A. Bonnell, *Scanning Probe Microscopy and Spectroscopy* (Wiley, 2000)

D. I. Bower, *An Introduction to Polymer Physics* (Cambridge, 2002)

J. Brandrup and E. H. Immergut, *Polymer Handbook* (Wiley, 1989)

A. N. Broers, *J. Electrochem. Soc.* **128**, 166 (1981)

G. Brown, M.A. Novotny, and P.A. Rikvold, *Phys. Rev. B.* **64**, 134422 (2001)

G. Brown, M.A. Novotny, and P.A. Rikvold, *J. Appl. Phys.* **87**, 4792 (2000)

C. Burger *et al.*, *Handbook of Polyelectrolytes and Their Applications* (American Scientific Publishers, 2002)

J. Y. Cheng *et al.*, *Adv. Mater.* **13,** 1174 (2001)

J. Y. Cheng, C. A. Ross, E. L. Thomas, H. I. Smith, G. J. Vancso, *Appl. Phys. Lett.* **81**, 3657 (2002)

J. Chen, M. Zhang, L.Yang, M. Collins, J. Parks, A. Avallone and T. P. Russell, *Journal of Polymer Science B* **20**, 2912 (2007)

J. Chen, M. A. Reed, A. M. Rawlett and J. M. Tour, *Science* **286**, 1550 (1999)

J. Cheng, C. A. Ross and A. Mayes, *Nature Materials* **3**, 823-8 (2004)

S.-Y. Chou, *Proc. IEEE* **85**, 652 (1997)

E.W. Cochran *et al., Macromolecules,* **39**, (2006)

Z. Cui, *Nanofabrication: Principles, Capabilities and Limits* (Springer, 2008)

Th. Dittrich, H. Angermann, W. Füssel, H. Flietner *Physica Status Solidi (a)* **140**, 463 (2006)

D. Dobrev, J. Vetter, N. Angert and R. Neumann, *Appl. Phys. A: Mater. Sci. Process.* **69**, 233 (1999)

D. Dobrev, J. Vetter, N. Angert, and R. Neumann, *Appl. Phys. A: Mater. Sci. Process.* **72**, 729 (2001)

M. Doi and S. F. Edwards *Theory of Polymer Dynamics* (Academic Press 1986)

W.J. Dressick and J.M. Calvert, *Jpn. J. Appl. Phys.* **32**, 5829 (1993)

E. W. Edwards, M. F. Montague, H. H. Solak, C. J. Hawker and P. F. Nealey, *Adv Mater.* **16**, 1315 (2004)

S. Fan *et al., Science* **283**, 512 (1999)

G. Fasol *et al., Science* **275**, 941 (1999)

J. M. Garcia *et al., J. Appl. Phys*. **85**, 5480 (1999)

P. Gaunt, *J. Appl. Phys.* **59**, 4129 (1986)

K. W. Guarini *et al,. IEEE Electron Devices Mtg Tech. Digest,* 541 (2003).

N. Hadjichristidis et al., *Block Copolymers: Synthetic Strategies, Physical Properties, and Applications* (Wiley, 2002)

U. Hartmann, *Annu. Rev. Mater. Sci.* **29**, 53 (1999)

J. Heier, E.J. Kramer, S. Walheim and G. Krausch, *Macromolecules* **30**, 6610 (1997)

E. Helfand and Z. R. Wasserman, *Macromolecules* **11**, 960 (1978)

J. Heremans and C. M. Thrush, *Phys. Rev. B* **59**, 12579 (1999)

E. Huang, P. Mansky, T.P. Russell, C. Harrison, P.M. Chaikin, R.A. Register, C.J. Hawker and J. Mays, *Macromolecules* **33**, 80 (2000)

T. L. Hylton *et al.*, *Appl. Phys. Lett.* **67**, 1154 (1995)

S. Ji *et al*., *Adv. Mat.* **16**, 3054 (2008)

D. Jiles, *Introduction to Magnetism and Magnetic Materials*, (Chapman & Hall, 1998)

Y. S. Jung and C. A. Ross, *Nano Lett.* **7**, 2046 (2007)

U. Kaiser, A. Schwarz and R. Wiesendanger, *Nature Letters* **446**, 522 (2007)

B. Kim, S. Park, T. J. McCarthy and T. P. Russell, *Small* **3 No. 11**, 1869 (2007)

G. Kim, M. Libera, *Macromolecules* **31**, 2670 (1998)

S. H. Kim *et al.*, *Adv. Mat*. **16**, 226 (2004)

S. O. Kim *et al.*, *Nature* **424**, 411 (2003)

H. A. Kramers, *Physica* (Utrecht) **7**, 284 (1940)

S. A. Maier *et* al., Adv. *Mater.* **13,** 1501 (2001).

P. Mansky, Y. Liu, E. Huang, T.P. Russell and C.J. Hawker, *Science* **275**, 1458 (1997)

P. Mansky, T.P. Russell, C.J. Hawker, M. Pitsikalis and J. Mays, *Macromolecules* **30**, 6810 (1997)

J. E. Mark, *Polymer Data Handbook* (Oxford University Press, 1999)

T. L. Morkved et al., *Science* **273**, 931 (1996)

K. Naito, H. Hieda, M. Sakurai, Y. Kamata and K. Asakawa, *IEEE Trans. Mag.* **38**, 1949 (2002)

L. N´eel *Ann. Geophys*. **5** 99 (1949)

M. Park, *et al.*, *Science* **276,** 1401 (1997)

M. J. Park et al., *Nano Lett.* **7**, 3547 (2007)

S. Park, J. Y. Wang, B. Kim, J. Xu and T. P. Russell, *Adv. Mater.* (2007)

S. Park, O. Yavuzcetin, B. Kim, M.T. Tuominen and T.P. Russell, *Small* **5**, 1064 (2009).

R.D. Peters, X.M. Yang, T.K. Kim, B.H. Sohn and P.F. Nealey, *Langmuir* **16**, 4625 (2000)

M. L. Plumer, J. van EK and D. Weller, *The Physics of Ultra-High-Density Magnetic Recording* (Springer, 2001)

P.Rai-Choudhury, *Handbook of Microlithography, Micromachining and Microfabrication* (SPIE, 1997)

G. Riess, *Prog. Polym. Sci.* **28**,1107 (2003)

L. Rockford *et al., Phys. Rev. Lett*. **82**, 2602 (1999)

M. Rooks, N. Belic, E. Kratschmer, and R. Viswanathan, *J. Vac. Sci. Technol. B* **23**, 2769 (2005)

C. A. Ross, *Annu. Rev. Mater. Res.* **31,** 203 (2001).

M. Rubinstein, R. H. Colby, *Polymer Physics* (Oxford University Press, 2003)

R. Ruiz *et al., Science* **321**, 936 (2008)

T. M. Rumke *et al., Opti. Exp*. **16**,5013 (2008)

Du Y. Ryu, K. Shin, E. Drockenmuller, C. J. Hawker and T. P. Russell, *Science* **308**, 236 (2005)

H. Saito *et al., J. of Magnetism and Magnetic Mat.* **310**, 939 (2007)

R. A. Segalman, H. Yokoyama and E. J. Kramer, *Adv. Mater*. **13**, 1152 (2001)

D. J. Sellmyer, M. Zheng and R. Skomski, *J. Phys. Condens. Matter* **13**, R433 (2001)

D. O. Shin *et al., Macromolecules* **42**, 1189 (2009)

A. Sidorenko, I. Tokarev, S. Minko, M. J. Stamm, *Am. Chem. Soc.* **125**, 12211 (2003), 125 (40)

R. Skomski and J. M. Coey, *Permanent Magnetism* (Bristol: Institute of Physics, 1999)

J. P. Spatz *et al*., *Adv. Mater.* **11,** 149 (1999)

E.C. Stoner and E.P. Wolfarth, *Phil. Trans. R. Soc. Lond., A,* **240**, 599–642 (1948)

M. P. Stoykovich *et al., Science* **308**, 1442 (2005)

R. Street and J. C. Wooley, *Proc. Phys. Soc. A* **62** 562 (1949)

G. J. Strikjers, J. H. J. Dalderop, M. A. A. Broeksteeg, J. J. M. Swagten and W. J. M. de Jonge, *J. Appl. Phys*. **86**, 5141 (1999)

G. Strobl, *The Physics of Polymers*, (Springer, 2007)

M. Sun, G. Zangari, M. Shamsuzzoha and R. M. Metzger, *Appl. Phys. Lett.* **78**, 2964 (2001)

T. Suzuki *et al., J. of Magnetism and Magnetic Mat.* **286**, 306 (2005)

C. Tang, E. M. Lennon, G. H. Fredrickson, E. J. Kramer and C. J. Hawker, *Science* **322**, 429 (2008)

J. M. C. Thornton *et al., Semicond. Sci. Technol.* **4**,847 (1989)

T. Thurn-Albrecht, J. Schotter, G.A. Kästle, N. Emley, T. Shibauchi, L. Krusin-Elbaum, K. Guarini, C. T. Black, M. T. Tuominen and T. P. Russell, *Science* **290**, 2126 (2000).

A. Ursache, M. Bal, J. T. Goldbach, R. L. Sandstrom, C. T. Black, T. P. Russell and M. T. Tuominen, *Mater. Res. Soc. Symp. Proc.* **721**, E3.3 (2002)

A. Ursache, J. T. Goldbach, T. P. Russell, and M. T. Tuominen, *J. Appl. Phys.* **97**, 10J322 (2005)

S. Wirth, S. V. Molnar, M. Field and D. D. Awscholom, *J. Appl. Phys.* **85**, 5249 (1999)

J. Wong, A. Scherer, M. Todorovic and S. Schultz, *J. Appl. Phys*. **85**, 5489 (1999)

H. Xiang, K. Shin, T. Kim, S. I. Moon, T. J. McCarthy and T. P. Russell, *Macromolecules* **37**, 5660 (2004)

Q. Xiao, R. V. Krotkov, and M. T. Tuominen, *J. of Appl. Phys.*, **99**, 08G305 (2006)

Q. Xiao, T. Yang, A. Ursache, and M. T. Tuominen, *J. Appl. Phys.***103**, 07c521 (2008)

T. Xu, C. J. Hawker, and T. P. Russell, *Macromolecules* **36**, 6178 (2003)

T. Xu, J. Stevens, J. Villa, J. T. Goldbach, K.W. Guarini, C. T. Black, C. J. Hawker and T. P. Russell, *Adv. Funct. Mater*. **13**, 698 (2003)

H. Yokoyama, T. E. Mates, and E. J. Kramer, *Macromolecules* **33**, 1888 (2000)

H. Zeng, M. Z. R. Skomski, D. J. Sellmyer, Y. Liu, L. Menon and S. Bandyopadhyay, *J. Appl. Phys.* **87**, 4718 (2000)

W. van Zoelen, T. Asumaa, J. Ruokolainen, O. Ikkala, G. ten Brinke, *Macromolecules* **41**, 3199 (2008)